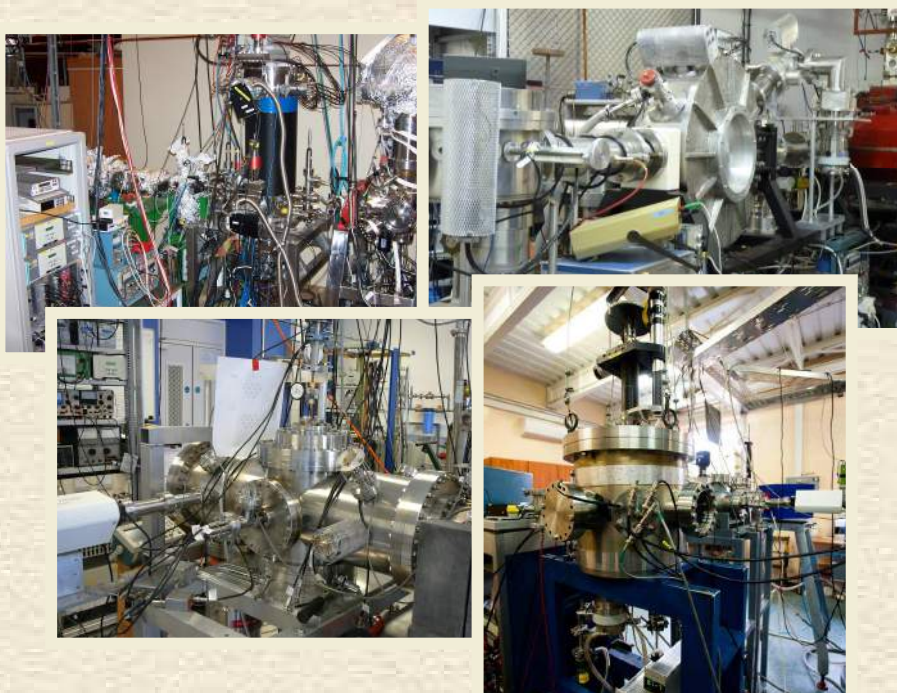


SZALAY CENTENARY

ATOMKI

ANNUAL REPORT

2009



INSTITUTE OF NUCLEAR RESEARCH
OF THE HUNGARIAN ACADEMY OF SCIENCES
DEBRECEN, HUNGARY

INSTITUTE OF NUCLEAR RESEARCH
OF THE HUNGARIAN ACADEMY OF SCIENCES
DEBRECEN, HUNGARY

ANNUAL REPORT
2009



ATOMKI

Postal address:

P.O. Box 51
H-4001 Debrecen,
Hungary

Editors:

I. Rajta
E. Leiter

HU ISSN0 0231-3596

Preface

The year 2009 was devoted to the 100th anniversary of the birth of Prof. Alexander Szalay, the founder and first director of Atomki¹. Prof. Szalay defined the still valid scientific credo of Atomki: Excellence in basic science together with a wide range of applications. In fact, the talks given on the centenary day reflected the interdisciplinary nature of the scientific activity in Atomki. This year the Researchers' Night talk in Atomki was given by Alexander Szalay Jr., about his astrophysical studies, based on SDSS observations and to complete the circle, the 30th Physicist Days, a week-long-event in Atomki was devoted to the International Year of Astronomy.

It is the firm aim of Atomki to follow interdisciplinary research subjects, no wonder in 2009 our colleague Zoltán Pécskay was invited to join a three-month-mission to Antarctica to collect rocks that can be studied later by Atomki laboratories.

We also celebrated with workshops the birthdays of Tibor Fényes (80), and Árpád Z. Kiss (70), prominent members of the Atomki community. The achievements of Árpád Z. Kiss have been also recognized by the Hungarian Government, awarding him the Knight's Cross Order of Merit of the Republic of Hungary, civil division.²

This year, Debrecen was the proud host of the Celebration of Hungarian Science, a yearly event of the Hungarian Academy of Sciences. Atomki had its share in the events organizing the workshop on alternative energy sources.

The infrastructure and activity in our laboratories are unique nationwide, drawing sizeable attention from the media: in 2009 two Atomki laboratories Laboratory of Secondary Neutral/Ion Mass Spectrometry (SNMS)³ and Electron Cyclotron Resonance Laboratory (ECR)⁴ have been presented in the TV show 'DELTA' broadcasted by the Hungarian Television.

Several changes have been made to the Atomki structure in 2009 aiming at more efficient work and streamlined activities. Among others the Atomki Accelerator Centre (AAC) was founded to emphasize further the maintenance and developments of the Atomki accelerators. Within the Debrecen Pharmapolis initiative we have further plans to upgrade the radiochemistry laboratory and the cyclotron facility to collaborate further in the field of pharmacy and medical physics with active involvement of companies nationwide.

The Atomki Annual Report features this year the Section of Atomic Collisions, where using our low energy accelerators quantum physics meets nanotechnology. The keyword is ionization, a complex phenomenon relevant from astrophysics to biology.

Further details of Atomki events, and the back issues of the Annual Reports can be found on our homepage⁵.

Debrecen, 2 August 2010



Zsolt Fülöp
Director

¹http://www.atomki.hu/100_Szalay/index_en.html

²http://www.keh.hu/state_decorations.html

³<http://www.atomki.hu/atomki/SNMS/>

⁴<http://www.atomki.hu/atomki/Accelerators/ECR/>

⁵<http://www.atomki.hu>

Szalay centenary

Prof. Alexander Szalay, the founder and first director of Atomki, was born on 4 October 1909. The Institute organized a series of events to celebrate the 100th anniversary of his birth. The centenary day was organized on 24 September 2009. Its main topic was how Szalay's ideas are continued today.

The opening talks were given by *Zsolt Fülöp*, director of Atomki, *Ádám Kiss*, President of the Nuclear Physics Committee of the HAS, *Gyula Faigel*, President of the Section of Physics of the HAS. Moreover, *Dénes Berényi*, former director of Atomki, full member of HAS, gave a memorial speech about his collaboration with Prof. Szalay.

Prof. Sándor A. Szalay Jr., presently full professor at Johns Hopkins University (Baltimore, MD, USA), gave a talk titled "Events, observations and the forming of my individuality in a scientist's family". The following lectures touched some of Prof. Szalay's extremely wide areas of interest. *István Hamvas* (Paks Nuclear Power Plant Ltd.) reviewed the history of the Hungarian uranium research. *Éva Svingor*, *Árpád Z. Kiss* and *Kadosa Balogh* talked about the laboratories of Atomki and their close connection to Prof. Szalay's research areas: environmental physics, accelerator physics and geochronology. *László Galuska* (Uni. Debrecen) described nuclear medicine research. *Árpád Molnár* (Uni. Szeged) talked about sonochemistry and *Zoltán Győry* (Uni. Debrecen) about agriculture applications.

Finally, *Ede Koltay* placed a wreath on Prof. Szalay's memorial tablet at the main entrance of the institute. After this, Prof. Szalay's embossment was unveiled in Sándor Szalay street.



Sándor A. Szalay Jr. and András Szalay by the embossment of their father.

On 5 October 2009, *Tibor Fényes* talked to the gathered family members, friends and colleagues at the tomb of Professor Szalay. On the same day, a memorial programme commemorating the 100th anniversary of the birth of Prof. Alexander Szalay was held at the Lajos Kossuth Evangelical Secondary School in Nyíregyháza, where as a pupil he made his first acquaintances with physics under the guidance of his father, renowned physics teacher of the school.

The programme of the memorial day included experimental demonstrations, special physics lessons, a lectures presenting the life and scientific achievements of Professor Szalay delivered by *Ádám Kovách* from Atomki, as well as a presentation recalling personal memories by *Rezső Lovas* the former director of Atomki. At last, a commemorative tablet honouring the achievements of Prof. A. Szalay was inaugurated at the outer wall of the main building of the gymnasium. The memorial day was a common programme of the L. Kossuth Secondary School, the Roland Eötvös Hungarian Physical Society and of the Institute of Nuclear Research of the Hungarian Academy of Sciences.

Organizational structure of ATOMKI

Director		
Dr. Zsolt Fülöp D.Sc.		
Deputy Directors		Finance Officer
Dr. Béla Sulik D.Sc.	Dr. József Molnár C.Eng.	Dr. Mária Pálincás
Scientific Secretary: Zoltán Máté, C.Sc. Scientific Secretary: Zsuzsa Trócsányi-Kiss, Ph.D. Knowledge and Technology Translator: Alíz Simon, Ph.D.		
Scientific Sections		
<ul style="list-style-type: none"> • Division of Nuclear Physics (Head: Attila Krasznahorkay, D.Sc.) <ul style="list-style-type: none"> • Section of Experimental Nuclear Physics (Head: János Timár, C.Sc.) • Section of Ion Beam Physics (Head: István Rajta, Ph.D.) <ul style="list-style-type: none"> • Nuclear Astrophysics Group • Laboratory of Ion Beam Applications • Section of Theoretical Physics (Head: András Kruppa, D.Sc.) 		
<ul style="list-style-type: none"> • Division of Atomic Physics (Head: Ákos Kövér, D.Sc.) <ul style="list-style-type: none"> • Section of Atomic Collisions (Head: László Gulyás, D.Sc.) • Section of Electron Spectroscopy and Materials Science (Head: László Kövér, Ph.D.) <ul style="list-style-type: none"> • Laboratory of Secondary Ion/Neutral Mass Spectrometry 		
<ul style="list-style-type: none"> • Division of Applied Physics (Head: Sándor Mészáros, C.Sc.) <ul style="list-style-type: none"> • Section of Environmental and Earth Sciences (Head: Mihály Molnár, Ph.D.) <ul style="list-style-type: none"> • Hertelendi Laboratory of Environmental Studies • Radon Group • K-Ar Laboratory • QMS Laboratory • DE TTK - ATOMKI Department of Environmental Physics (Head: István Csige, Ph.D.) • Section of Cyclotron Applications (Head: Ferenc Ditrói, Ph.D.) • Section of Electronics (Head: János Gál, C.Sc.) <ul style="list-style-type: none"> • Computational Group 		
<ul style="list-style-type: none"> • Accelerator Centre (Head: Sándor Biri, Ph.D.) <ul style="list-style-type: none"> • Cyclotron Laboratory • Laboratory of Electrostatic Accelerators • ECR Laboratory • Isotope Separator Laboratory 		
<ul style="list-style-type: none"> • Services <ul style="list-style-type: none"> • Library (Librarian: Mária Nagy) • Accounting (Ibolya Monostori) • Basic Services and Maintenance (Head: István Katona) • Mechanical Workshop (Head: Zoltán Pintye) • Radiation- and Environmental Protection Group 		

Data on ATOMKI

At present the Institute employs 195 persons. The affiliation of personnel to units of organization and the composition of personnel are given below.

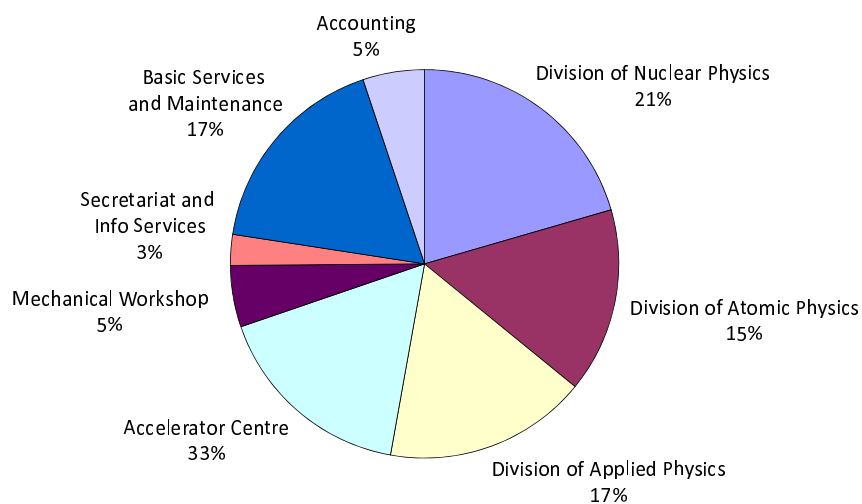


Figure 1. Affiliation of personnel to units of organization

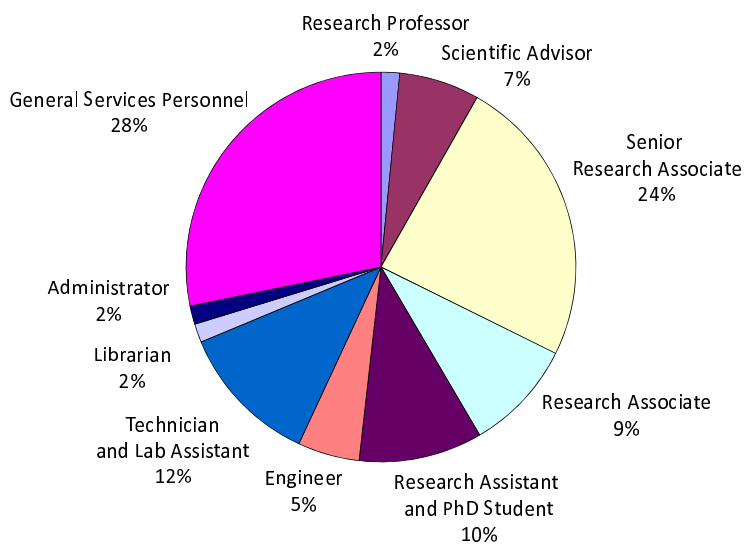


Figure 2. Composition of personnel

International connections

Multilateral international programs: 15

Cooperations based on S&T (TéT) bilateral intergovernmental agreements: 14

Cooperations based on HAS bilateral agreements: 20

Cooperations based on specific collaboration agreements between institutes:

- in nuclear physics and applications with 22 countries in 36 topics
- in atomic physics and applications with 21 countries in 39 topics
- in detection and signal processing technique with 5 countries in 6 topics
- in ion beam analysis with 6 countries in 7 topics
- in environmental research and dating with 11 countries in 13 topics

Membership in international scientific committees: 25

Running research projects, grants

European Research Council (ERC) Starting Grant: 1

Other EU projects: 12

European Organization for Nuclear Research (CERN) projects: 2

International Atomic Energy Agency (IAEA) projects: 2

Intercomparison programs and exercises: 5

(ESIR, VIRI, EURATOM, TRI-TOFFY, TRIC2008-IAEA)

Hungarian National Research Foundation (OTKA) projects: 12

National Office for Research and Technology (NKTH) projects: 3

Hungarian Science and Technology Foundation (TéT) projects: 14

CHARISMA

Cultural Heritage Advanced Research Infrastructures: Synergy for a Multidisciplinary Approach to Conservation/Restoration

Call for Proposals

The FP7 project, CHARISMA, of the European Commission is a consortium of 21 partners (universities, museums, research centres and institutions) that are centres of excellence in scientific research devoted to cultural heritage. <http://www.charismaproject.eu>

Among other activities, CHARISMA supports users from all institutions of the EU member countries and associates* for their transnational access to medium and large-scale facilities in Hungary and France (FIXLAB).

The FIXLAB facilities are:

- the **ATOMKI-HAS nuclear microprobe** (Debrecen, Hungary) for high spatial resolution measurements of microsamples with a focussed ion beam;
- **BNC** (Budapest, Hungary) with access to various neutron-based instruments to investigate elemental and structural composition;
- the **AGLAE ion beam accelerator at C2RMF** (Paris, France), providing elemental analysis with an external beam for whole art objects;
- **IPANEMA, the platform for ancient material research at synchrotron SOLEIL** (Gif-sur-Yvette, France) for X-ray, UV-visible and FTIR synchrotron methods.

For more information please visit:

<http://iba.atomki.hu/charisma/index.html> or

<http://www.charismaproject.eu/transnational-access/fixlab/fixlab-welcome-desk.aspx>

We publish a call twice a year (June & December) with an application deadline:
15 September and 15 March, respectively.

Contact at ATOMKI-HAS: Dr. Aliz SIMON: a.simon@atomki.hu

We are looking forward to receiving your proposals.

* Please enquire about other eligible countries.

Transnational Access Service at ATOMKI-HAS in the field of Cultural Heritage

The **Laboratory of Ion Beam Applications (IBA)** (<http://iba.atomki.hu/>) is equipped with a 5 MV Van de Graaff electrostatic accelerator, as well as ion beam analytical facilities and instruments. The assortment of ion beams and their energy range makes it possible to apply most of the non-invasive ion beam analytical techniques used for the study of cultural heritage.

Expected users are scientists, curators, art historians, archaeologists, conservators, restorers who usually carry out research on materials with ion beams especially at a micrometer scale. The main fields of study are: a) materials alterations (origin, products and mechanisms); b) provenance studies; c) characterization of micro-details of altered or unaltered materials e.g. to prevent further damages; d) studying of the manufacturing techniques as a contribution to art-historical studies; e) characterisation of the artwork conservation state or the effectiveness of a conservation treatment.

The following methods are available for research on cultural heritage materials: Particle Induced X-ray Emission technique (PIXE), Rutherford Backscattering Spectrometry (RBS), Particle Induced Gamma-ray Emission technique (PIGE), Nuclear Reaction Analysis (NRA), Elastic Recoil Detection Analysis (ERDA) and Scanning Transmission Ion Tomography (STIM).

Beam lines are included in CHARISMA project:

- Macro-PIXE line for bulk analysis of samples in the Mg-U atomic number range with a **milli-beam**
- Oxford Microbeams Scanning Nuclear Microprobe (SNM) facility for analysis of samples from H to U with high lateral resolution; with a **micro-beam** (1 μm beamsize).

Expected analyses at our infrastructure are: elemental composition, lateral and depth distribution of the elements, elemental mapping, surface topography as well as 2D tomography. The sample chambers are equipped with several detectors. In case of SNM an ultra thin windowed and a Be windowed Si(Li) X-ray detectors are used for the simultaneous detection of elements from Carbon to Uranium. Gamma ray detectors (HPGe and in request Clover-Ge-BGO) are available for PIGE analysis and depth profile measurements of light elements. Particle detectors are installed for RBS and NRA analysis. ERDA setup is applied for hydrogen detection. The data acquisition (DAQ) system consists of an ATOMKI-type Digital Signal Processor at the Macro-PIXE setup and an OM_DAQ and Canberra/Genie-2000 DAQ at the SNM. Auxiliary instruments are also available (http://iba.atomki.hu/facilities_en.html) e.g. XRF setup, optical microscopes, ultrasonic cleaner, evaporator for surface coating.

Services offered within FIXLAB

Access to the ATOMKI IBA service is given in hours. 8 hours/day measurement time is planned but for technical and scientific reasons continuous run (24 hours/day) can also be implemented. The minimum duration of stay is 2 days and it can not exceed 5 days.

Data evaluation is promoted by the assistance of the scientists of the IBA laboratory of ATOMKI-HAS while data interpretation is done by the users.

The CHARISMA project financially supports travel, subsistence and beamtime for the eligible users. The submitted proposals are evaluated by an international Peer Review Panel.

THE STUDY OF ARCHAEOLOGICALLY INTERESTING GLASSY AND METAL ARTEFACTS IN HAS-ATOMKI

Alíz Simon, Imre Uzonyi, Gábor Tomka¹, Zoltán Szoboszlai, Zsófia Kertész, Árpád Zoltán Kiss

Institute of Nuclear Research of the Hungarian Academy of Sciences (HAS-ATOMKI), P.O. Box 51, H-4001 Debrecen, Hungary
¹Hungarian National Museum, 14-16 Múzeum krt., H-1088 Budapest, Hungary



IBA SETUP AND ANALYSIS

- PIXE: UTW Si(Li) & Be windowed detectors. Simultaneous quantitative elemental analysis between C-U.
- RBS: Substrate composition, depth profiling
- ERDA: Hydrogen content determination
- NRA: C, O, elemental depth profiling
- PIGE: DIGE: Light element analysis (Li, B, F, C, N, O)

Broad beam and microbeam irradiations

- 1-3.5 MeV H⁺, D⁺, He⁺
- min. beam size: 1×1 μm²
- max. scan: 2500×2500 μm²
- Full and area selective spectra and elemental maps
- Listmode, tomographic images, true elemental maps



ATOMKI Scanning Nuclear Microprobe [1,2]

Data acquisition & evaluation

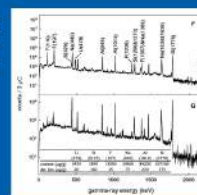
- Oxford-type and Canberra-type DAQ
- PIXE/MI-M and PKLM TPI program packages [3,4]
- RBX and WINDF codes [5,6]

OBSIDIAN SOURCES OF THE TOKAJ MOUNTAINS, HUNGARY



Aim: to find sub-groups among the classified obsidian sources of the Cenozoic volcanic Tokaj Mountains (NE Hungary-E Slovakia).

Compton suppressed spectrum measured on a standard macusanite obsidian glass (F) and on an obsidian sample (G). E_{beam} = 3.3 MeV, Q = 3.3 μC, I = 1 nA [7]



On the basis of the PIGE measurements alone, the clusterisation of samples of Tokaj Mountains from other specimens could be achieved.

As a result of the analyses a database was provided for the LITHOTECA of the Hungarian National Museum.

MEDIEVAL GLASS BOTTLE



Archaeological excavation was carried out in Győr (West-Hungary) in 2004-2005. Remnants from the Roman Period (1st-2nd c.) and from various periods of the Middle Ages (10th-15th c.) were found. From a storage pit (Nr. 259), pieces of a glass bottle were saved. The 18 cm tall bottle was restored, its well preserved material has a greenish tint.

- The "goiter necked" glass bottles were spread in Southern and Central Europe.
- The find from Győr can be dated with great probability to the 2nd half or to the end of the 13th century.

Questions to be answered: • Origin of the glass • Production technology
 Analytical characterization by PIXE and PIGE

Concentrations and their standard deviations are in wt.%. For comparison, chemical composition of Venetian glasses (V1-11: 14th c. [8]; V2-16th c. [9]; V3-15-16th c. [10]) were used.

	Bottle	V-1	V-2	V-3
Na ₂ O	15.761	14.0	13.0	15.423.4
MgO	2.340.2	2.30	3.30	1.140.3
Al ₂ O ₃	4.520.5	4.00	0.90	1.721.2
SiO ₂	65.012	64.7	68.0	70.323.0
K ₂ O	2.250.1	2.50	2.50	3.423.0
CaO	6.540.1	7.50	9.50	4.640.8
TiO ₂	0.2350.01	0.24	0.06	—
MnO	1.110.1	1.90	0.60	0.1240.07
Fe ₂ O ₃	2.010.6	1.40	0.50	0.7710.39

Conclusions

- The bottle was made from soda-lime glass.
- Comparing Na, Mg and Ca values with literature data → "similarity" with Venice glass.
- However, high Ti, Fe (and Al) concentrations → relatively low quality vitrifying agent. (siliceous material) was used excluding late medieval (15-16th c.) fine Venetian glass.
- The greenish tint attributable to the high Fe content → incomplete decolorization (by MnO) → characteristic for lower quality glass products.

The analytical results do not falsify the hypotheses that the artefact can be a 13th century (supposedly Venice) glass.

SILVER COINS

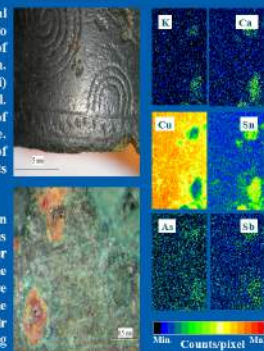
Ancient silver coins (drachms) issued by the Greek city Dyrrhachium during 68-43 years BC were analysed non-destructively by mikro-PIXE method. The selected 27 drachms, including four imitations, belong to the numismatic collection of the Hungarian National Museum.

Nine elements (Fe, Cu, Zn, Br, Ag, Sn, Au, Pb and Bi) were determined quantitatively. PIXE showed uniformly low (~2%) Ag concentrations, implying debasement. The PIXE results also made it clear that ancient imitations can be identified by their high Sn content [11].



ANALYSIS OF LATE BRONZE AGE METALS

The main event of the complex cultural changes during the transition from Middle to Late Bronze Age was the appearance of Tumulus culture in the Danube-Tisza region. In this period people rose mounds (tumuli) above their graves made from stone and soil. Depots were typical of the final period of Middle Bronze Age called Koszider-phase. During the tumulus period the practice of hiding depots came to its end, bronze objects were put into graves.



The IBA analyses can provide a relation between the Koszider and Tumulus metallurgy. The main question is whether there is any noticeable change between the metallurgical craftsmanship of the consecutive eras. It is important to determine the composition of the used raw materials, their sources, as well as the applied manufacturing technologies [12].

REFERENCES

- [1] Rajta, I. Borbély-Kist, Gy. Múric, L. Barnha, E. Kolty, Á. Z. Kiss; Nucl. Instr. and Meth. B 109 (1996) 148.
- [2] Uzonyi, Gy., Székely, I., Borbély-Kist, Á. Z. Kiss; NIM B 210 (2003) 147.
- [3] Gy. Szabó and I. Borbély-Kist; NIM B 175 (1993) 123.
- [4] Uzonyi and Gy. Szabó; NIM B 221 (2005) 156.
- [5] E. Köhl; Nucl. Instr. Meth. B 85 (1994) 588.
- [6] N.P. Barradas, P.K. Marriott, C. Jeynes, R.P. Webb; Nucl. Instr. and Meth. B 136-138 (1998) 1157.
- [7] Z. Elek, I. Uzonyi, B. Grátsz, P. Róssa, Á. Z. Kiss, Gy. Szabó; Nucl. Instr. and Meth. B 161 (2000) 836.
- [8] M. Verità; *Technique et Science. Les Arts du Verrre. Actes du Colloque de Namur* oct 1989, Presse Universitaire de Namur, pp. 57-59.
- [9] M. Verità and T. Tomatis; *Rivista della Storia. Venetia n. 4* (1990) 149.
- [10] B. Grátsz et al.; *Archaeologia. Central European Series I, BAR International Series 1043 (II)* (2002) 565.
- [11] I. Uzonyi, E. Bugoi, A. Sallán, Á. Z. Kiss, B. Constantinescu, M. Turbige; Nucl. Instr. and Meth. B 161 (2000) 748.
- [12] G. Senta, I. Uzonyi, Cs. Cséghi, L. Dárdai; *Archaeometriai Műhely 0* (2007) 19-30.

For scientific collaboration and TNA service please contact Dr. Alíz Simon, a.simon@atomki.hu

Higher education activity

Number of researchers teaching at universities: 39

Number of researchers teaching in doctoral (PhD) schools: 11

Gradual and postgradual teaching: 62 courses, 1293 hours

Number of undergraduate students participating in research work
(organized by the Student's Science Association, TDK): 4

Number of students making diploma work: 12

Number of PhD students: 9

Supervision activity by Atomki researchers: 1822 hours

Finance

The total budget of the Institute for the year 2009 was 1489 million Hungarian Forints income, and 1479 million Hungarian Forints expenses. The composition of the budget and the share of personnel expenditure within the budget are shown below.

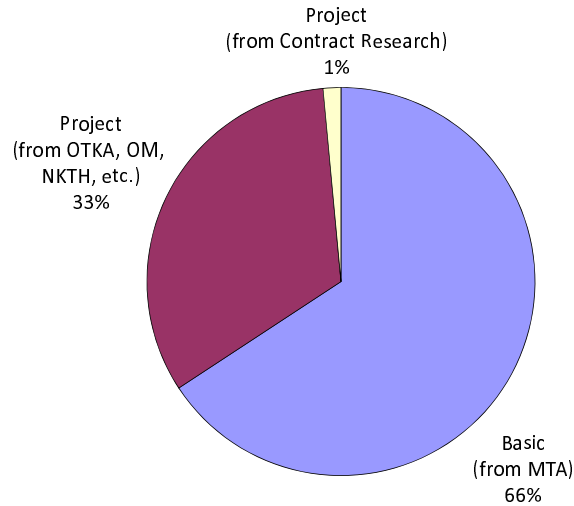


Figure 3. Composition of the budget of the Institute
MTA: Hungarian Academy of Sciences
OTKA: Hungarian Scientific Research Fund
OM: Ministry of Education
NKTH: National Office for Research and Technology

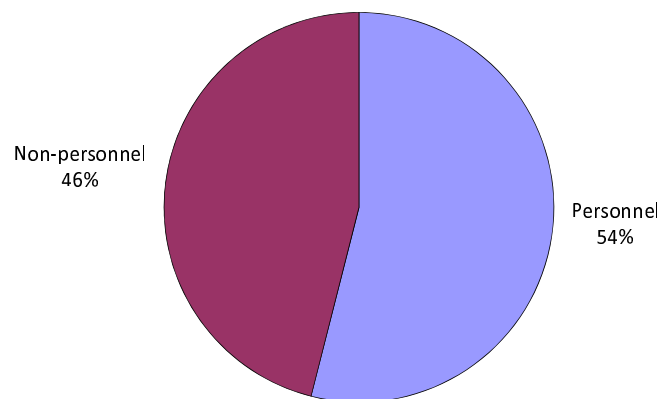


Figure 4. Breakdown of expenditure into personnel and non-personnel expenditures

Table of contents

Preface	i
Szalay centenary	ii
Organizational structure of ATOMKI	iii
Data on ATOMKI	iv
International connections	v
Running research projects, grants	v
CHARISMA - Call for proposals	vi
Higher education activity	ix
Finance	x
Table of contents	xi

Featured:

Section of Atomic Collisions	1
--	---

1. General Physics

1.1 Exactly solvable potentials with finite positive position-dependent mass	22
1.2 Asymptotic iteration method to bound-state problems with unbroken and broken supersymmetry	23

2. Sub Atomic Physics

2.1 Stellar and Primordial Nucleosynthesis of ${}^7\text{Be}$: measurement of ${}^3\text{He}(\alpha, \gamma){}^7\text{Be}$	24
2.2 Persistent decoupling of valence neutrons toward the dripline: study of ${}^{20}\text{C}$ by γ spectroscopy	25
2.3 Study of the neutron-rich ${}^{21}\text{N}$ nucleus through proton inelastic scattering	26
2.4 Hyperdeformed band in the ${}^{36}\text{Ar}$ nucleus?	27
2.5 In-beam γ -ray spectroscopy of the neutron rich ${}^{39}\text{Si}$	29
2.6 High resolution study of the Gamow-Teller strength distribution in Sc isotopes	30
2.7 High precision ${}^{89}\text{Y}(\alpha, \alpha){}^{89}\text{Y}$ scattering at low energies	31
2.8 Structure of high-spin bands in ${}^{104}\text{Pd}$	32
2.9 Gamma-ray multipolarity assignments in ${}^{132}\text{La}$	33
2.10 Medium- and high-spin band structure of ${}^{134}\text{Pr}$	34
2.11 Precise half-life measurement of the 10 h isomer in ${}^{154}\text{Tb}$	35
2.12 Search for $E(5)$ type nuclei in terms of the sextic oscillator	36
2.13 Phases of clusterized nuclei	37

3. Atomic and Molecular Physics

3.1 Double differential ionization of H_2O by positron impact	38
3.2 A reaction microscope for studies positron - atom collisions	39
3.3 Electron Guiding through Insulating Nanocapillaries	40
3.4 Angular and energy differential electron emission cross sections in collisions between antiprotons and helium atoms	41
3.5 Atomic Ionization by Ultrashort Half-Cycle Pulses	42

3.6	Single and double ionization of He by slow antiproton impact	43
3.7	State-to-state interference in electron induced resonant Auger decay	44
3.8	Multiple electron scattering sequences in $C^{q+} + Ar$ collisions at energies and charge states relevant for carbon ion therapy	45
3.9	Ionization of the H_2^+ by intense ultrashort laser pulses	46
3.10	Ionization of the H_2O molecule by intense ultrashort laser pulses	47
3.11	ECR Plasma Photos	48
3.12	Resonant Mn KLL Auger spectra excited from a nanolayer sample	49
4.	Materials Science and Analysis	
4.1	Simulation of attosecond streaking of electrons emitted from a tungsten surface	50
4.2	Monte Carlo simulation of electron spectra scattered elastically from Au-C double-layer sample at relativistic energy	51
4.3	Quantification of surface effects: Monte Carlo simulation of REELS spectra to obtain surface excitation parameter	52
4.4	Identification of hydrogen and deuterium at the surface of water ice by reflection electron energy loss spectroscopy	53
4.5	Electroless nickel plating with different pre-treatments on silicon carbide particles	54
4.6	An experimental study on the effect of aqueous hypophosphite pre-treatment used on an Al-alloy substrate before electroless Ni plating	55
4.7	On the composition depth profile of electrodeposited Fe-Co-Ni alloys	56
4.8	Energy dependence of electron transmission through a single glass macrocapillary	57
4.9	Heatable sample holder for capillary experiments	58
4.10	Search for collective excitations in nanoparticles of biological origin	59
5.	Earth and Cosmic Sciences, Environmental Research	
5.1	Radiocarbon dating of the last volcanic eruption of the Ciomadul volcano, Southeast Carpathians	60
5.2	Atmospheric fossil fuel CO_2 record in Debrecen city during the winter of 2008	61
5.3	Using an ultrapure 4He spike in tritium measurements of water samples by the 3He ingrowth method	62
5.4	Separation of ^{79}Se from L/ILW radioactive waste material produced by the Hungarian NPP	64
5.5	Improved determination of Tc-99 in L/ILW liquid wastes with special emphasis on quantitative Ag-108m separation	65
5.6	Environmental survey of the low and intermediate level radioactive waste disposal facility Bataapati before the operation of the site	66
5.7	Experimental investigation and numerical modelling of tritium wash-out by precipitation in the area of the nuclear power plant of Paks, Hungary	67
5.8	Characterization of urban aerosol sources in Debrecen, Hungary	68
5.9	Study of Cl containing urban aerosol particles by ion beam analytical methods	69
6.	Biological, Chemical and Medical Research	
6.1	^{11}C -radioisotope study of methanol co-reaction with ethanol over Ni-MCM-41 silica-alumina and Ni-alumina	70
6.2	Production of ^{117m}Sn with high specific activity	71

6.3	Separation of ^{103}Pd from metal Rhodium by dry distillation	72
6.4	Study of the sap-flow and related quantities of oak trees in field experiments	73
6.5	Technology for microbial synthesis of nanoparticles	74
7.	Developments of Methods and Instruments	
7.1	The ATOMKI Accelerator Center	75
7.2	Fabrication of optical devices in poly(dimethylsiloxane)by proton microbeam	79
7.3	WCGM - a gamma-spectrum analysis program rewritten in Windows	80
7.4	Report on the development of an XRF set-up with X-ray tube excitation	82
7.5	Micro-XANES and micro-PIXE measurements of iron-rich impact materials from the Barringer Crater	83
7.6	Detection efficiency of a low-energy TOF neutron spectrometer	84
7.7	Deposition station for selenium isotopes	85
7.8	Theoretical study of three-dimensionally position-sensitive scintillation detector based on continuous crystal	86
7.9	Giant resonances in BaF_2 scintillators	87
7.10	The energy linearity and resolution of Si based X-ray detectors based on the properties of plasmons	88
8.	Appendix	
8.1	Events	89
8.2	Hebdomadal Seminars	90
8.3	Awards	92
8.4	List of Publications	93
	Author index	94

Section of Atomic Collisions

D. Berényi, S. Biri, L. Gulyás, Z. Juhász, Á. Kövér, A. Orbán, J. Pálinkás, T. Papp, R. Rácz, S. Ricz, T. Ricsóka, L. Sarkadi, B. Sulik, I. Török, K. Tőkési¹, D. Varga¹

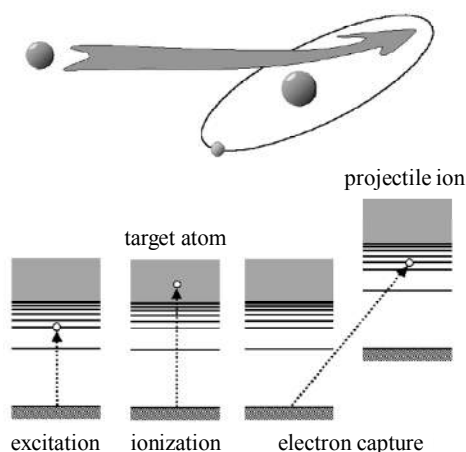
1. Introduction

The Section of Atomic Collisions is a research unit with extended activity in the field of atomic and molecular physics. Starting from the study of atomic processes at the beamlines of nuclear physics accelerators in the seventies, our research community became one of the centers of fundamental research in Atomki. We also have a strong connection to materials sciences especially along the line of electron and ion spectroscopy methods. Our present activity covers a wide range of topics from atomic collision mechanisms of fundamental interest, to the complex interactions of electrons, ions, photons and antiparticles with atoms, molecules, surfaces, and specific nanostructures. In the last few years, an increasing fraction of our present topics has become relevant for applications, e.g., molecular collision studies for the radiation therapy methods of tumors, or ion-nanostructure interactions for the future construction of small ion-focusing elements.

Our section belongs to the Division of Atomic Physics. The other unit of the Division is the Section of Electron Spectroscopy and Materials Sciences. There are traditionally good connections and a strong collaboration between the groups of the two sections in many fields. From the very beginning of our research work in atomic collisions, external collaborations were of vital importance for us. We regularly organize international workshops in the field of fast ion-atom collisions and related small conferences in Debrecen from 1981. Recently, we organized the Conference on Radiation Damage in Biomolecular Systems (RADAM 2008, Debrecen), and co-organized the Conference on Elementary Processes in Atomic Systems (CEPAS 2008, Cluj). We have access to several large scale facilities in Europe within the framework of formal and informal collaborations.

The most characteristic research activity of our Section is the study of fast atomic collisions. The term „fast” definitely means that the impact energies are far above the thermal energy range of our surroundings. With other words, in atomic collision physics, we typically deliver a large amount of energy to the electronic systems of a few atoms. Sometimes our projectiles are really very fast, with GeV/nucleon energies. We mostly use accelerators for production of these energetic particles; therefore this research field is often called as “accelerator-based atomic physics”. We have used all Atomki accelerators and ion sources (MGC Cyclotron, VdG-1, VdG-5, and ECRIS) in our experiments and many accelerator facilities worldwide. The basic processes in these energetic, fast collisions are as follows:

- excitation
- ionization
- electron capture
(charge-exchange)
- relaxation.



We are mainly interested in the dynamical aspect of the collision. The most direct information on the dynamics can be obtained by observing the primarily ejected electrons having continuous energy distribution. The dynamics – particularly for the ionization of inner atomic shells – can also be studied by detection of the decay products (photons, Auger or autoionization electrons) emitted from the excited states. Recoil ions or ionic fragments of the molecules carry important information about the collisions, too. In our research of the collision dynamics we use all these app-

proaches, applying the methods of x-ray and charged particle (electron or ion) spectrometry.

The primary aim of the investigations is the better understanding of the dynamics of the fast atomic collisions by studying, first of all, collisions involving a few particles. Furthermore, by performing electron and x-ray spectroscopic measurements of the atomic (molecular) states excited in the collisions, we wish to explore more deeply the electronic structure of the atoms and molecules. Besides the investigations of the simple collision systems car-

¹Section of Electron Spectroscopy and Materials Sciences

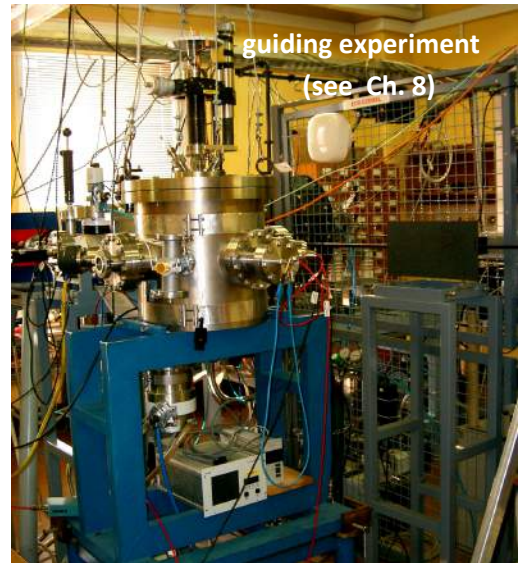
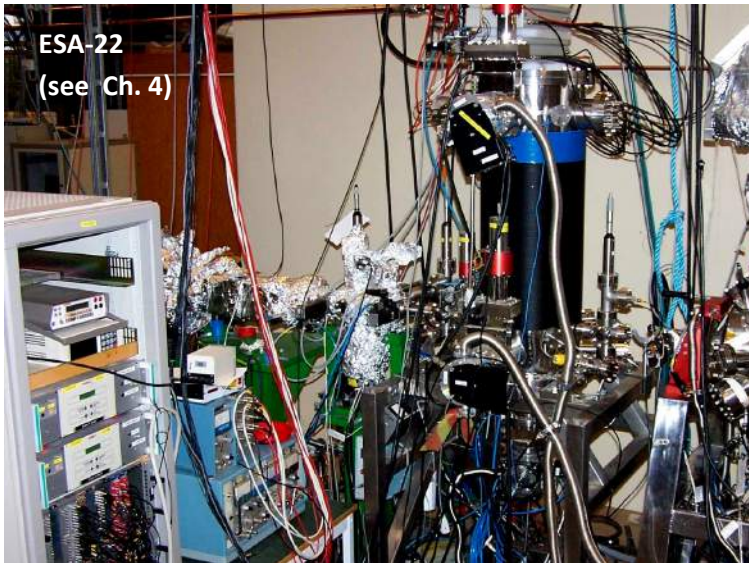
ried out on free atoms and molecules, we study also the interactions of more complex systems, like the collisions of photons, electrons, light and heavy ions with solids. As a further example, we may mention our research work exploring the properties of some mesoscopic systems (fullerene molecules, micro-capillaries).

Our approach is primarily experimental, but the theoretical work carried out in connection with our own and other's experiments is also remarkable. A significant part of the activity of the Section of Atomic Collisions is the development of new research instruments and methods. Due to the experimental character of most of the research work, this activity primarily implies the development of experimental tools, first of all, construction of electron spectrometers in collaboration with the Section of Electron Spectroscopy and Materials Sciences. It is worth mentioning the development of the theoretical methods for the description of various collision processes.

1.1. Historical review

Our research work in the field of the atomic collisions started about 35 years ago. At that time many groups in the world working in the field of nuclear physics realized that their experimental techniques (particle accelerators, detectors, etc.) can effectively be used to explore the so far unknown properties of the structure and dynamics of atoms and molecules. The research activity of our group has also roots in nuclear physics, specifically in the field of β spectroscopy. Quite naturally, our first "atomic physics" experiments represented a transition between the old and new research subjects of the group: Electrons and positrons originating from radioactive sources were used to ionize the inner shells of atoms [1].

Despite of the tradition and experience in the field of electron spectroscopy, the first "true" collision experiments were carried out with use of the x-ray spectroscopy method. In these experiments energetic beams of electrons, protons, alpha particles and heavier ions provided by the accelerators of ATOMKI (the Cockcroft–Walton generator, the 5-MV Van de Graaff generator, and later the cyclotron) were used to ionize the K, L and M shell of atoms. The absolute ionization cross sections were determined by measuring the yield of the x-ray photons emitted following the ionization. Later the angular distribution of the x rays was also measured by which the alignment parameter characterizing the charge-cloud asymmetry of the ionized atom was established. The satellite structures of the K, L and M x-ray lines, intensity irregularities of the $K\beta_5$ line, and the cristal spectrometer based PIXE method are also worth mentioning here.



In parallel with the x-ray spectroscopic experiments, soon an electron spectrometer suitable for the study of collisions has been constructed. In the following decades several further electron spectrometers – often with unique parameters – have been built. For atomic collision physics the most successful types are ESA-13, ESA-21 and ESA-22. Some of them are working in other laboratories, some of them we operate at the beamlines of large scale facility accelerators and synchrotrons, often in collaboration framework. With use of these spectrometers and other instruments and devices developed by our group (ion beam cleaner, charge-state analyzer, fast particle detector, recoil-ion detector, time-of-flight electron spectrometer, etc.) we performed systematic experiments for a large variety of collision processes and phenomena. Just to mention the most important ones: collisional Auger-electron emission, continuum electron emission including the "cusp" phenomenon, post-collision interaction, multiple ioni-

zation, photoionization, positron-impact ionization, Fermi-shuttle type “ping pong games” of the colliding heavy partners with the liberated electron, one- and two-center electron-electron interactions, coherent electron emission from diatomic molecules. For the results achieved in the field of the electron spectroscopic investigations of the collision processes our group earned a world-wide reputation.

For earlier topics, we refer to the longer list of the selected atomic physics publications at the home page of the Section of Atomic Collisions: http://www.atomki.hu/atomki/AtomPhys/index_en.html. Starting from there, information about the experimental facilities or the external collaborations is also available. In the following, we select a few topics of our research activities and some important results in the field of atomic collisions. These recent examples include collisions between heavy or light charged particles and photons with atoms or molecules, as well as ion guiding throughout nana-capillaries.

2. Forward electron emission from energetic atomic collisions

One of the most fundamental research subjects of the Section of Atomic Collisions is the study of *forward electron emission*. The energy spectra of the electrons ejected at small angles from atomic collisions exhibit a characteristic, sharp peak [2]. The peak, known as “cusp”, is centered at the electron energy that corresponds to a velocity which is equal to that of the projectile. The equality of the velocities means that in the projectile-centered reference frame these electrons move slowly, that is, they occupy the low-lying continuum states around the projectile. The population of such states may take place basically via two processes. If the projectile has bound electrons (“clothed” ions or atoms), it may lose them with small kinetic energy as a result of ionization by the target atoms (*electron loss to the continuum*, ELC). The other process is a special kind of ionization of the target by the projectile, called *electron capture to the continuum* (ECC) [126]. ECC can be viewed by extrapolating the real capture processes populating high Rydler states to “capture” to low-lying continuum states around the projectile. Experimentally, ECC and ELC can be identified detecting the electrons in coincidence with the outgoing charged-state analyzed projectiles. Since the cusp corresponds to emission of low-energy 2 electrons in the projectile reference system, its formation is governed by Wigner’s threshold law [3], i.e., the cusp is a *threshold phenomenon*. Another general feature of the cusp is that it is formed by *final-state interaction* between the ejected electron and the outgoing projectile; therefore its intensity and shape are mainly determined by the asymptotic properties of the collision system in the outgoing phase. In the followings we present some examples of the investigations carried out in the Section of Atomic Collisions for the phenomenon of the electron cusp.

2.1. The electron cusp with neutral outgoing projectile in the final state

According to Wigner’s threshold law, the appearance of the cusp in the electron spectrum at impact of charged projectiles can be traced back to the long-range nature of the Coulomb force. For neutral atomic projectiles the Coulomb potential around the nucleus is fully screened, that is, the interaction has a short range. Consequently, the ECC cusp should not exist for impact of neutral atoms. Surprisingly, our group observed a narrow and pronounced ECC cusp in a coincidence measurement using 300 keV He^0 projectiles [4] (see Figure 1).

Following our unexpected observation, several theoretical and experimental investigations have been carried out on the subject. The cusp with neutral outgoing projectile in the final state can be studied basically in two processes: (i) target ionization by neutral atoms (ECC), and (ii) single electron detachment from negative ions (ELC). To solve the puzzle of the cusp induced by neutral atomic projectiles we conducted systematic experiments for both processes. In the ECC experiments we used H^0 [5] and He^0 projectiles [6, 7], in the ELC experiments we measured the cusp following the collisional electron detachment from H^- [8] and He^- [9].

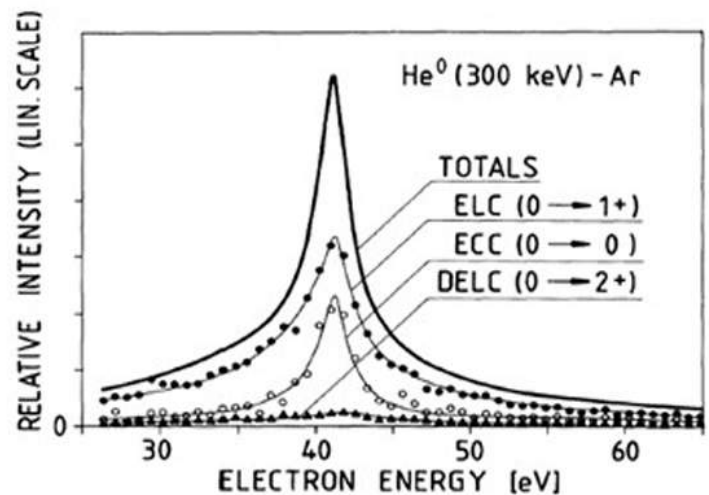


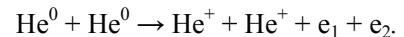
Figure 1. Electron energy spectra obtained from He^0 on Ar collisions at 0° in coincidence with the outgoing He^0 , He^+ and He^{2+} projectiles.

The data obtained for He^0 and He^- projectiles supported the theoretical model proposed by Barrachina [10] which assumes that a weakly bound or low-lying virtual state of the $e^- + \text{He}$ system is responsible for the narrow and pronounced ECC cusp. For hydrogen projectiles we observed that the ECC cusp induced by neutral hydrogen atoms is significantly larger than that induced by protons. Unlike for He^0 , the origin of the ECC cusp for H^0 projectiles is not clear, most probably it can be interpreted as a result of *dipolar* interaction between the ejected electron and the outgoing neutral hydrogen atom [11].

2.2. Observation of the two-electron cusp

In all our previous cusp experiments we detected a single electron. Recently the following question came up: How is the cusp modified in the presence of another electron? In other words: Does the two-electron cusp exist?

The formation of the two-electron cusp supposedly leads to a final state consisting of two slow electrons in the Coulomb field of a positive ion core. Such a state was first considered by Wannier [12]. He applied Wigner's idea [3] in atomic physics for processes leading to two free electrons in the final state at threshold. Such processes are, for example, the electron-impact single ionization or the photon-induced double ionization of atoms. He treated the process in the classical mechanics, and found that the electrons escape from the atom symmetrically in opposite directions, i.e., there is a strong 180° correlation between the electrons. On the basis of the Wannier's picture we may also ask: Can one observe the Wannier-type correlated two-electron continuum states also in atomic collisions? To show the existence of the two-electron cusp, we measured the energies of the electrons ejected in forward direction from the process [13]:



The impact energy was 100 keV. This was a triple coincidence experiment: We detected coincidences between the two electrons and the outgoing charged-changed projectile ions. We obtained that the coincidence yield showed a peak as a function of the electron energies at the expected cusp position (see Figure 2). Furthermore, a strong correlation was found between the energies of the two electrons, which are traced back to an angular correlation of 180° in the projectile-centered reference system. This finding strongly supports of the formation of Wannier-type correlated two-electron continuum states around the projectile.

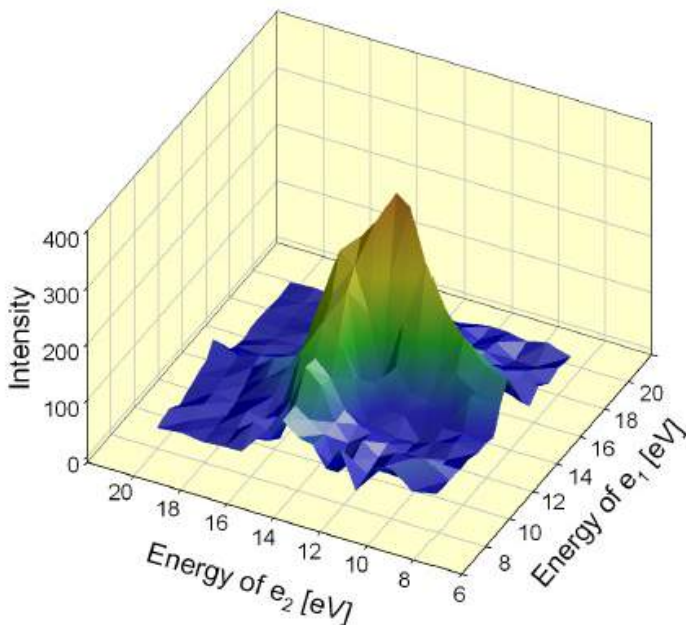


Figure 2. The two-electron cusp observed in 100 keV He^0 on He collisions.

3. Positron–atom collisions

Positrons are the antiparticles of electrons; therefore the understanding of positron-induced reactions with atoms and molecules remains a significant challenge, driven by the quest to advance fundamental knowledge of the underlying physical mechanisms, as well as to be able to control and to apply them. In this respect, ionization is particularly pertinent, with examples ranging from damage limitation to healthy tissue during a scan employing positron emitters (as in Positron-Emission Tomography) – or indeed targeting of tumors by the same means, to the investigation of the interstellar medium and the solar atmosphere.

The correlated dynamics of few interacting particles is a fundamental physics problem that may be exemplified through the process of ionization. Despite the tremendous progress in its theoretical description during the past decades, concomitant experimental investigations remain essential in assessing the accuracy of the various approaches and in guiding further developments. In this respect, particularly sensitive are studies in which there are two or more light particles (e.g. an electron and a positron) in the final state and which yield cross sections which are differential in the energy and/or angular distribution of the ejected electron(s) and/or scattered projectile. The most stringent among these is the triply differential cross section (TDCS) in which all the kinematic parameters are

determined. A significant body of data has been gained using the (e^- ; $2e^-$) method (e.g., [24]) and the Cold Target Recoil Ion Momentum Spectroscopy (COLTRIM technique (e.g., [25])), which has been applied to electron, photon, proton, and ion impact. Differential studies with positrons, mainly confined to doubly differential investigations remain scarce but are desirable both intrinsically and for comparison with equivelocity electrons or protons to probe the role of the projectile charge or mass on the collision dynamics.

During the last two decades several double- and triple-differential measurement of positron-impact ionization have been carried out in cooperation with the positron group at University College London (UCL) (e.g., [26, 27, 28, 29, 30, 31, 32]). One of the main aims of these studies has been to investigate electron capture to the continuum (ECC), a special case of ionization in which the ionized electron is strongly influenced by the positively charged projectile. This process, whose description requires higher-order approximations [33] can be considered as an extrapolation across the ionization limit to highly-excited bound states. In the case of ion impact, a sharp peak appears in the doubly-differential electron spectrum around 0° at a velocity which is close to that of the scattered projectile. For positron impact, due to the positive charge of the positron, similar-final state interactions are expected. However, due to the equal masses of the electron and the positron, different collision dynamics may occur resulting in scattering for positrons to much larger angles than for heavier projectiles.

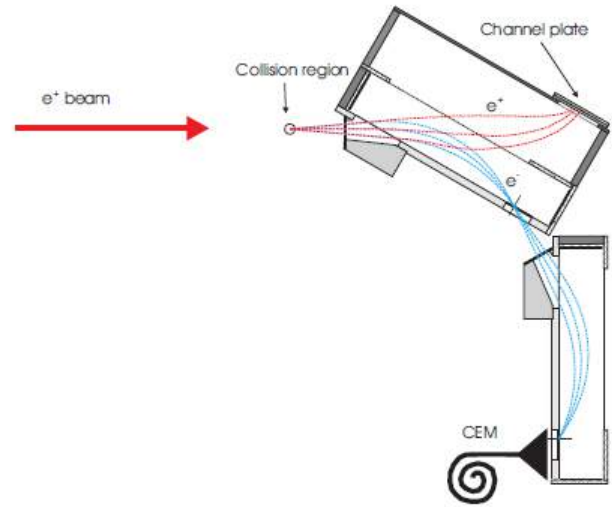


Figure 3. Experimental arrangement to measure the ionized electrons and scattered positrons in coincidence.

Figure 3 shows the experimental system developed for triple-differential measurements [34]. The parallel-plate analyzer (PPA) with time focusing determines the energy of the ionized electron while the scattered positrons ejected into the same direction are counted by a channel plate. Initially investigations of the doubly-differential electron energy spectra found no peak which could be associated with ECC [26-28]. Aided by theoretical investigations [35], it was surmised that the wide angle scattering of the light projectile from the heavy target (Ar) applied in the experiment would spread the ECC peak over a broad range of angles, in contrast to the sharp cusp observed by ion impact at around 0° with respect to the beam direction. For this reason, a more sensitive (triple-differential) measurement was performed by measuring coincidences between the scattered positron and the ionized electron, and a lower-Z target (H_2) was used. At 100 eV projectile energy a small broad peak was found in the electronic spectrum, the first clear experimental demonstration of the occurrence of ECC by positron impact [29]. Theoretical

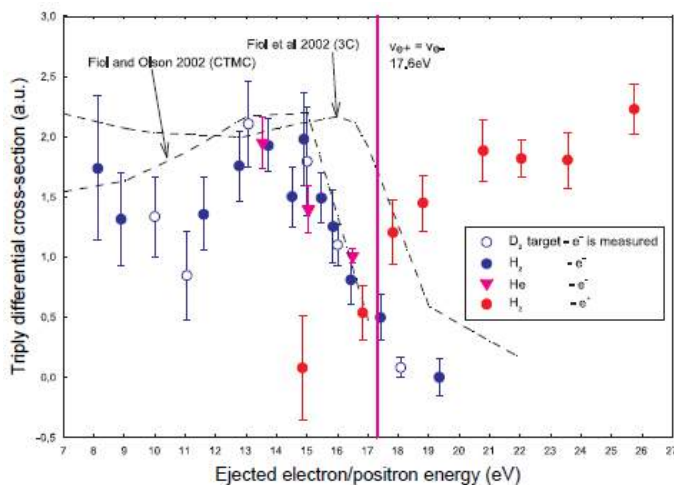


Figure 4. Experimental data of the triply-differential ionization cross sections at 50 eV e^+ -projectile impact.

calculations were soon able to reproduce these findings [36, 37]. However, at 50 eV impact energy the electron spectrum was observed to be shifted to a lower energy by 1.6 eV relative to the theoretical value [30]. Further investigations showed that a similar shift but towards higher energies occurs in the corresponding energy spectrum of the scattered positrons (Figure 4) [31]. Although not fully understood, a possible explanation of these surprising findings is that the polarization of the positron–electron pair in the positive Coulomb field of the residual target ion causes the ejected electron to be slowed down and the scattered positron to be accelerated [127].

Further investigation of the energy and angular distribution of the ionized electron and the scattered positron originated from the collisions will be carried out with a recently developed system

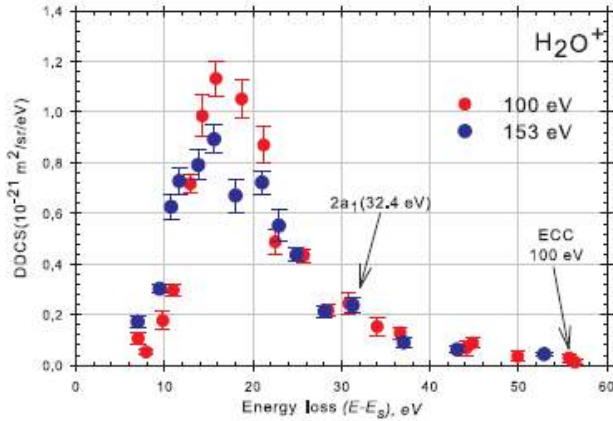


Figure 5. Energy loss spectrum of e^+ scattered projectile in coincidence with the H_2O^+ fragments. From 100, 153 eV e^+ - H_2O collisions.

momentum distribution of the target atoms due to the small momentum transfer (0.3–4 a.u.) during collision).

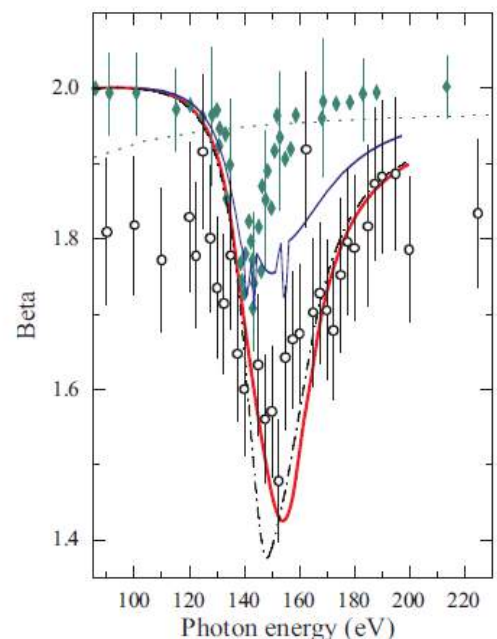
It is worth to mention our study of positron impact ionization of H_2O . The investigation of the intrinsic properties of H_2O and of its interactions with various projectiles remains a vigorous multidisciplinary pursuit, spurred by the universal importance of this molecule. In the case of irradiation by positrons, for example, the role that water radiolysis plays in cell destruction is becoming increasingly pertinent due to the widespread usage of positron emission tomography in medical diagnostics. Here, knowledge of integral and differential cross-sections underpins the understanding of the microscopic distribution of energy deposits needed for accurate dosimetry. Experimentally, whilst a considerable data library is now available for positron scattering from atoms and molecules, data on $e^+ - H_2O$ collisions remain scarce. They consist of total cross sections and of preliminary results for the positronium formation and differential ionization cross sections.

A differential ionization study on H_2O is of special interest due to its strong dipole moment, which has been shown to cause significant forward scattering of electron projectiles [39]. The main aims of our work have been to investigate whether forward scattering enhances the probability of ECC around 0° and to measure the intensity ratios of different fragments at various projectile energies. Figure 5 shows the results for H_2O^+ fragments at 100 and 153 eV positron impact energy. No ECC peak has been found in the double-differential electron spectrum, similarly to the earlier results obtained with Ar [26], indicating that the strong dipole moment of the water does not significantly enhance the ECC process for positron projectiles. However, a small shoulder around 32 eV energy loss has been recorded at both projectile energies. This structure may be consistent with the results of high-resolution electron momentum spectroscopy ([40] and references therein), identifying 32.4 eV as the onset of a weak shake-up band connected with the $2a_1$ orbital.

4. Photon-atom interactions

The experimental study of photon-atom interaction started almost ten years ago in our division. The aim of these measurements were to investigate the higher-order effects in photoexcitation/ionization (e.g. role of the electron correlation, channel interaction, multipole mixing etc). The angle-resolved photoelectron spectroscopy (ARPES) and photoelectron-Auger-electron coincidence technique as well as linearly polarized synchrotron radiation were applied in these studies. The measurements were performed at the Max-II storage ring in Lund, Sweden and at the DORIS III in Hamburg, Germany. The angular distributions of the photoelectrons were collected in the oscillation plane of the electric vector of the photon.

Figure 6. Comparison of the present experimental angular distribution β parameters (open circles) with the earlier experimental results of Hemmers *et al.* [46] (diamonds) and with the theoretical values: RIPM [47] (dot line), 13-channel RRPA (dash-line) [43], 20-channel RRPA [43] (thick solid line), TDDFT [45] (thin solid line).



[38] by measuring the energy and angular distribution of the recoil ions.

This method, called (COLTRIMS), has been successfully applied for investigating ion, electron and photon collisions (see [25] and reference therein). A benefit of COLTRIMS is the 4π collection of the recoil ions comparing with the traditional methods where only a small part of the collision events can be detected. When the residual ions are recorded in coincidence with the outgoing fragments, a kinematically complete picture can be determined about the correlated motion of the fragments of atomic and molecular breakup processes. Up till now the COLTRIMS have not been used in positron collision physics due to the serious requirement for the quality of the projectile and the target beam (small projectile and target beam diameter (around 1 mm), high target density (10^{11} – 10^{13} atom/cm³), and narrow initial

The experimental setup was based for a special electrostatic electron spectrometer (ESA-22, see Ref. [41] for details) which is capable to measure the angular distribution of the emitted electrons simultaneously in the angular range from 0° to 360° relative to the quantization axis. Another option is that two independent electron energies can be analyzed in the same time, both in the $0 \pm 180^\circ$ angular range. The latter feature of the spectrometer provides condition to carry out electron-electron coincidence experiments with large solid angle, as well as electron-electron angular correlation experiments.

In one of our experiments we measured the angular distribution of the $5s$ photoelectrons of xenon with linearly polarized light in the 90–225 eV photon energy range in order to determine the dipole (β) and non-dipole (γ and δ) anisotropy parameters [42]. In this energy range the relativistic and non-relativistic random phase approximations (RRPA and RPAE) [43, 44] and the time-dependent density functional theory (TDDFT) [45] predict strong distortion in the photon energy dependence of the anisotropy parameters due to the interactions between the $5s$ and the $4d$; $4p$ ionization channels, while the independent particle model [47] shows smooth curves without any structures. Figures 6 and 7 show the comparison between our experimental data and the theoretical predictions for the dipole β and non-dipole γ anisotropy parameters, respectively. One can see that the measured data are closer to the RRPA, RPAE and the TDDFT description, and they confirm the breakdown of the independent particle model. This was the first measurement where a strong channel interaction was observed in the photon energy dependence of the non-dipole anisotropy parameters.

In the measurement discussed above the effect of the interaction between the different ionization channels was demonstrated. In another measurement, the effect of channel mixing between the direct and indirect ionization processes was investigated [48]. The angular distribution of the $3p$ photoelectrons of argon was measured with linearly polarized synchrotron radiation in the 90–330 eV

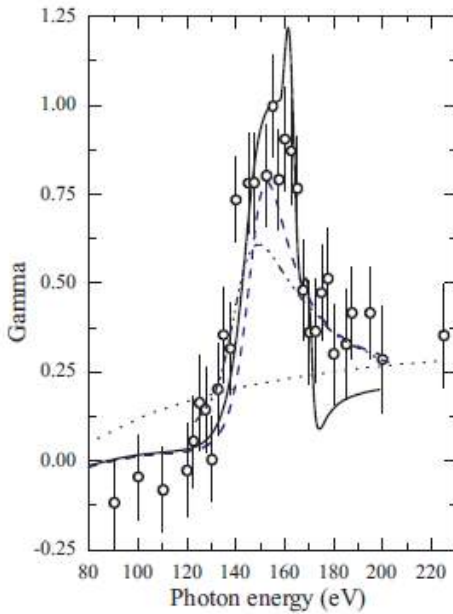


Figure 7. Comparison of the experimental non-dipole γ parameters (open circles) with the corresponding theoretical values in function of the photon energy. Theory: RIPM [47] (dot line), 13-channel RPAE [44] (dash dot line), 13-channel RRPA (dash line) [43], 20-channel RRPA [43] (solid line).

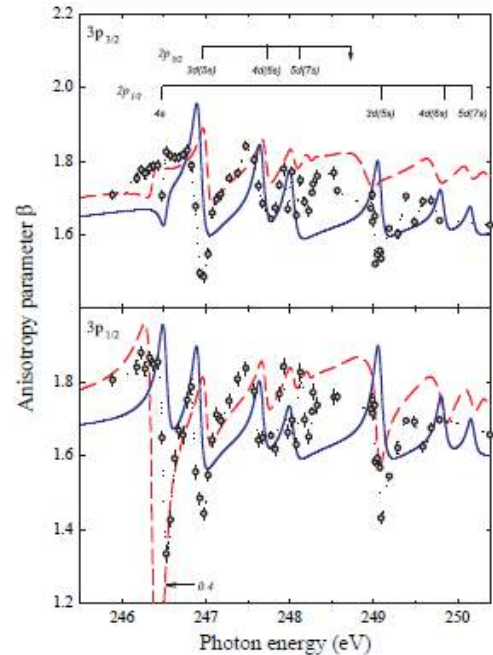


Figure 8. Comparison of the present experimental angular distribution β parameters (dots connected with dotted line) with the results of the R matrix [49] (dashed line) and the MCDF (solid line) calculations. The $2p_{1/2,3/2} \rightarrow ns/md$ resonance positions are shown in the figure as vertical bars whereas arrows indicate the corresponding threshold energies [51].

photon energy range in order to determine the dipole and non-dipole angular anisotropy parameters. The experimentally observed $\beta_{3p_{1/2},3p_{3/2}}$ parameters were compared with the corresponding multichannel quantum defect theory (MQDT) of Gorczyca and Robicheaux [49] and the relativistic independent particle calculation (RIPC)

[47]. In addition, the effect of the participator Auger decay to the angular distribution of Ar $3p$ photoelectrons was also determined with multi-configuration Dirac–Fock calculation by using the RATIP program package [50].

The detailed investigation of the $2p \rightarrow ns/md$ resonant photon energy region was carried out with high energy resolution and with narrow photon bandwidth. The experimental results for the dipole $\beta_{3p_{1/2},3p_{3/2}}$ anisotropy parameters are presented in Figure 8. As it is seen the experimental β parameters show strong variation at the vicinity of $2p \rightarrow ns/md$ resonances. Furthermore the participator Auger decay channels have different effects on the $\beta_{3p_{1/2}}$ and $\beta_{3p_{3/2}}$ parameters, similarly to the predictions of Gorczyca and Robicheaux [49]. For instance, the $\beta_{3p_{1/2}}$ parameter is strongly modified at the vicinity of $2p_{1/2} \rightarrow 4s$ resonance, whereas the effect on $\beta_{3p_{3/2}}$ parameter is much weaker. At higher resonances, the effects on the β parameters are quite similar to the calculated ones except at the $2p_{1/2} \rightarrow 3d/5s$ resonance which affects more the $\beta_{3p_{3/2}}$ parameter. This is the first experimental investigation which demonstrates the effect of interference between the participator resonant Auger decay (indirect ionization channel) and the direct photoionization channel on the angular distribution of emitted photoelectrons.

The application of coincidence technique is a useful tool for the separation of the overlapping excitation, ionization and decay processes. For example, the L_{23} –MM Auger spectrum of argon consists of many overlapping lines, originating from different excitation and rearrangement processes even in the case of ultra high energy resolution. By detecting photoelectron–Auger-electron coincidences between the Ar $2p_{1/2,3/2}$ photo- and L_{23} – $M_{23}M_{23}$ Auger electrons one can eliminate the overlap between the final states, and one can separate the ionization and excitation channels [41]. We carried out such an experiment at 440 eV photon energy with high energy resolution in both the photon energy and the electron spectrometer side to distinguish between the $2p_{1/2}$ and $2p_{3/2}$ photo lines. Figure 9 shows the measured L_{23} – $M_{23}M_{23}$ single and the random-coincidence corrected $2p_{1/2,3/2}$ photoelectron–Auger-electron coincidence spectra of argon. The Auger- and photoelectron data were integrated over the angular range $-75^\circ \div +75^\circ$ and $-82.5^\circ \div +82.5^\circ$, respectively. The solid line is the well-known single Auger spectrum (without coincidence condition), the circles with error bars represent the coincidence data. The single spectra are normalized to the intensity of the $^2P_{3/2}$ – 1D_2 and $^2P_{1/2}$ – $^3P_{012}$ coincidence Auger peaks. Figure 9 (a) and (b) show clearly that we could eliminate the overlap between the L_2 – $M_{23}M_{23}$ and L_3 – $M_{23}M_{23}$ Auger transitions in the coincident spectra. Figure 9 (a) shows that the $^3P_{012}$ to 1D_2 intensity ratio measured in the coincidence experiment is different from that obtained without the coincidence condition. It demonstrates well that the coincidence condition can remove such disturbing processes which are hidden in the single measurements.

During the measurement of the angular distribution of the photoelectrons our impression was that the intensity distributions are not symmetric relative to the propagation direction of the photon beam. The all angle-resolved photoelectron spectra were reanalyzed, and a left–right asymmetry has been observed in the double differential cross sections of the photoelectrons. (See the geometrical definition of the left and right side, the expression of the asymmetry parameter as well as details of the experiments in Refs. [52, 53]). A series of measurements were carried out to study the left–right asymmetry parameters for H2 molecule and for the following s shells of noble gas atoms: He $1s$, Ne $2s$, Ar $3s$, Kr $4s$ and Xe $5s$. The measurements were repeated rotating the vacuum chamber and the spectrometer by 180° in order to check the systematic errors at the Max-II storage ring in Lund (Sweden). The experiment was repeated also at the DORIS III synchrotron in Hamburg for the He $1s$, Ne $2s$, Ar $3s$ and Xe $5s$ photoelectrons with a different electron spectrometer and photon source. Figure 10 compares the DORIS III [53] (solid triangles) and the Max-II [52] (solid circles) experimental left–right asymmetry parameters as well as the

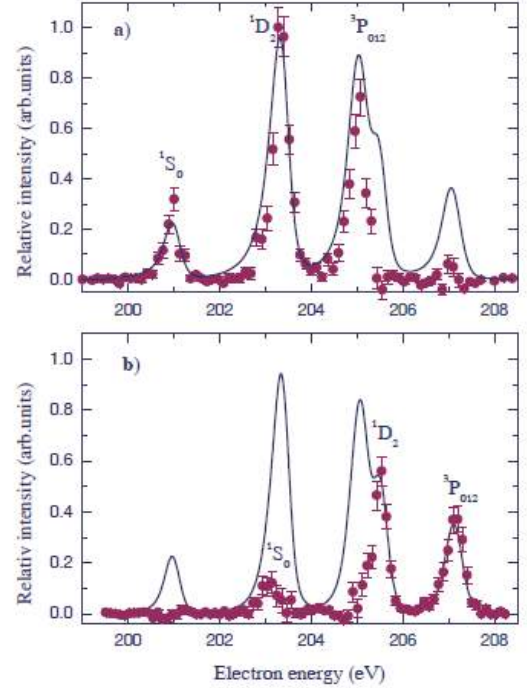


Figure 9. Comparison between the measured single and true coincidence L_{23} – $M_{23}M_{23}$ Auger spectra of argon a solid line and full circles with error bars represent the single and the coincidence spectra, respectively. (a) In coincidence with $2p_{3/2}$ photoelectrons, (b) in coincidence with $2p_{1/2}$ photoelectrons. The data were normalized to the $^2P_{3/2}$ – 1D_2 , and $^2P_{1/2}$ – $^3P_{012}$ transitions.

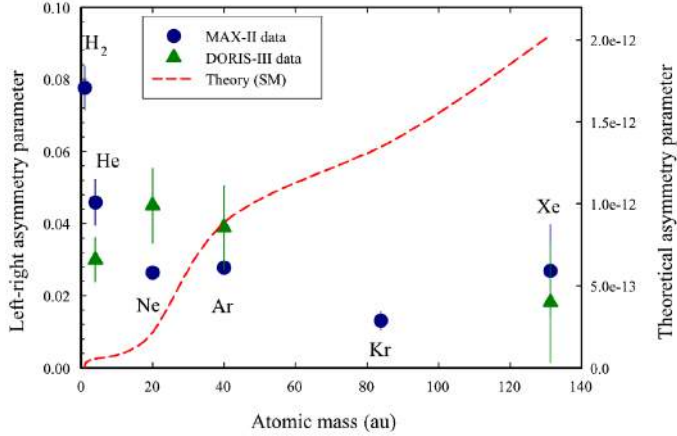


Figure 10. Comparison of the DORIS III experimental left-right asymmetry parameters [53] (solid triangles) with the Max-II experimental results [52] (solid circles) and the theoretical values [52] as a function of the atomic mass for the H_2 molecule and for the noble gas atoms from He to Xe. The dashed line and the right hand scale represent the theoretical estimation of the left-right asymmetry parameters [52].

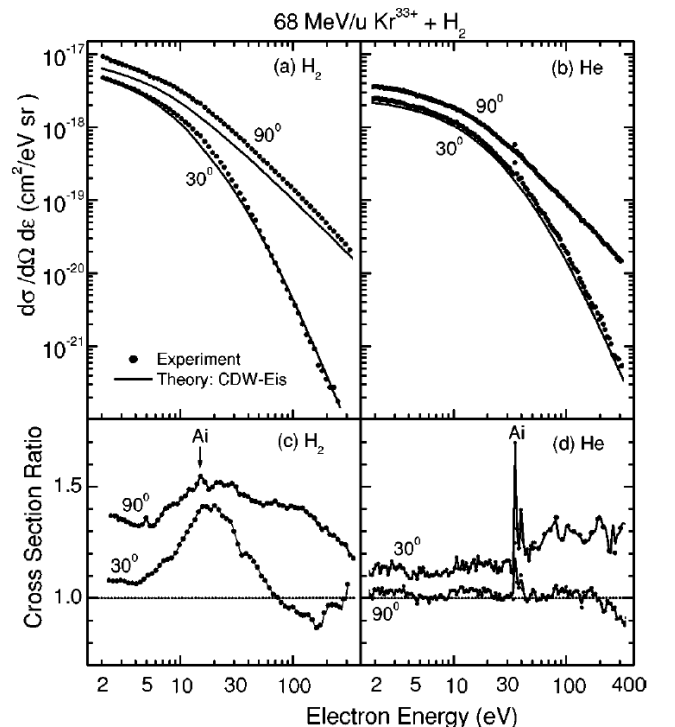
calculated data [52] (dashed line and right hand scale) as a function of the atomic mass. In the figure the average of the three experimental data sets reported in Ref.[52] is plotted as the result of the Max-II measurement. The theoretical asymmetry parameters were calculated within the framework of the Standard Model (for details see [52]). In this model the left-right asymmetry is due to parity violation by the weak interaction through the exchange of a Z_0 boson among the atomic nucleons and electrons.

The figure shows agreement between the two experimental data sets. Both the DORIS III and the Max-II experimental asymmetry parameters differ significantly from zero. Small differences can be seen between the results of the Lund and Hamburg measurements. This may originate from the slightly different photoelectron energies (i.e., also different photon energies) in the two sets of experiments. The difference in energies was 3.7 eV. The atomic mass dependence of the calculated data [52] is totally different from the results of the measurements. Moreover, the experimental asymmetry parameters are orders of magnitude larger (a factor of 10^{10} – 10^{11}) than the calculated values. The DORIS III measurements confirm the statement in Ref. [52] that the observed left–right asymmetry cannot originate from the weak interaction among the nucleons and atomic electrons. In both experiments great care has been taken to exclude or quantify all possible sources of systematic errors that could introduce an experimental asymmetry. We are not aware of any additional experimental effects that could produce a left–right asymmetry in the measurements. We have to conclude that the observed left–right asymmetry is the result of a real physical process. Currently, there is no explanation for the non-zero asymmetry parameter. If the non-zero asymmetry is a real physical effect, it means the breakdown of space inversion symmetry in the photon–atom interaction.

5. Interference effects in electron emission from H_2 by fast ion impact

Studies of particle-induced ionization have devoted particular attention to the molecular target H_2 , which is the simplest molecule composed of two atoms. While the overall ionization was well understood at the end of the 1990’s, little was known about phenomena associated with the indistinguishability of the atomic H centers. In this case, the contributions to ionization from each center add coherently, and interference effects may be expected in the ionization spectra. Such electron emission from H_2 is closely related to Young’s two-slit experiment, which played an essential role in the early development of quantum mechanics. Early studies of collisionally induced interferences from H_2 centered on the processes of electron capture and photoionization, but no experimental evidence for coherent electron emission had been found.

Figure 11. Cross sections and ratios for electron emission by 68 MeV/u Kr^{33+} impacting on H_2 and He as a function of the electron energy. In *a* and *b*, experimental and theoretical cross sections are compared for H_2 and He, respectively, obtained at the observation angles 30° and 90° . In *c* and *d*, cross-section ratios of experimental and theoretical results are given for H_2 and He, respectively. The peaks labeled “Ai” are attributed to autoionization. [58].



In the late '90-s, a multilateral international collaboration, with Atomki participation, was developed to reveal these interference effects in atomic collisions with H₂. The starting point was the analysis of the analogies between the impact of very fast charged particles and photons [54-56]. We have found evidence for coherent electron emission from the hydrogen molecule in collisions with very fast, highly charged ions [57-63].

The analysis indicated that the use of a high projectile velocity is important because it enhances interference effects. The electron energy spectra obtained at different observation angles exhibited oscillatory structures in good agreement with model calculations.

In Figs. 11a and 11b, typical results for electron emission from H₂ and He, respectively, are shown for observation angles $\theta = 30^\circ$ and $\theta = 90^\circ$. Also plotted are theoretical (CDW-EIS, see later in the theoretical part of this review) cross sections obtained for *atomic* targets. The cross sections vary by several orders of magnitude with the electron energy. Since the variation due to the interference term is less than a factor of 2, we removed this strongly variation by dividing the measured cross sections by the corresponding theoretical atomic cross sections. The results for 30° and 90° associated with H₂ and He are given in Figs. 11c and 11d, respectively.

Apart from the distinct peak near 33 eV, the benchmark He data show a smooth and nearly monotonic dependence on the ejected electron energy. On the contrary, the 30° cross-section ratio for H₂ shows a non-monotonic behavior suggestive of an oscillatory structure well outside the experimental uncertainties.

To understand more quantitatively the interference structures, the experimental data are compared with theoretical results. The cross section for electron emission from H₂ relevant for these experiments is given by [57]

$$\frac{d\sigma_{H_2}}{d\Omega d\epsilon} = \int \frac{d\sigma_{2H}}{dq d\Omega d\epsilon} \left[1 + \frac{\sin(pd)}{pd} \right] d^2q_\perp$$

where the solid angle $d\Omega$ and the energy transfer $d\epsilon$ refer to the outgoing electron. The cross section $d\sigma_{2H}/dq d\Omega d\epsilon$ describes incoherent electron emission from the two independent H atoms. The term in parentheses represents the interference caused by coherent emission from the two centers, where d is the internuclear distance of the H₂ molecule and $p = |\mathbf{k} - \mathbf{q}|$ is the difference between the electron momentum \mathbf{k} and the momentum transfer \mathbf{q} .

Numerical calculations were performed using the above formula in conjunction with analytical Born cross sections for atomic hydrogen. These calculations were normalized to the corresponding integrated Born cross sections and are shown by the solid curves in Fig. 12. To gain more information about the oscillation frequency, we used an analytical fit function in the form $A [1 + \sin(kcd)/(kcd)] + B$, where A and B (with $A + B = 1$) are interfering and noninterfering cross section fractions, respectively, and c is an adjustable frequency parameter. The functions fitted to the experimental data are also shown in Fig. 12. The experimental data are well reproduced by the analytic function with a frequency parameter c nearly equal to $\cos \theta$.

These experiments [57-61] have explored the oscillatory structures in H₂ electron emission spectra attributed to the Young-type interferences. Evidence has been provided for the fact that the oscillation frequency of the interference pattern varies significantly with the electron ejection angle. Later theoretical approaches provided insight into the nature of the observed interference structures. The oscillation frequency has been found to be governed mainly by the electron momentum component parallel to the beam direction.

This topic attracts increasing interest today, including experimental studies of the phenomenon in photoionization at synchrotrons. Due to its fundamental character, and its challenging uncleaned features, coherent electron emission from molecules is a central topic at atomic collision conferences.

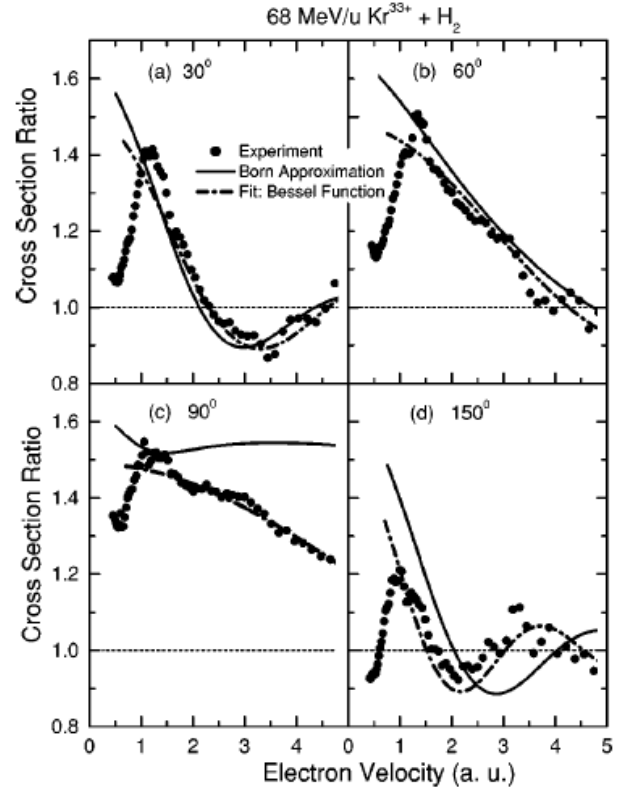


Figure 12. Ratios of experimental to theoretical cross sections plotted as a function of the ejected electron velocity for the electron observation angles indicated. The solid lines represent Born calculations and the dash dotted lines are obtained from fits to an analytic function (see text). [58]

6. Fast electron ejection in slow and intermediate velocity ion-atom collisions: Fermi-shuttle type ping-pong games in single ionization

Ionisation is not only a complicated process. It is a rich field of strange phenomena. Therefore, double differential spectra of electrons ejected in ion-atom and ion-solid collisions are in the focus of general interest for a long time.

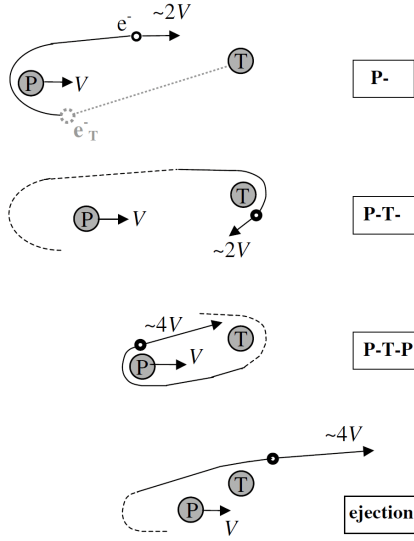


Figure 13. A classical view of a P-T-P scattering sequence [71]. The starting step is a binary collision between the heavy projectile ion and the active target electron, i.e. a P process.

approach, which turned out to be successful in describing this complicated process, is the classical trajectory Monte-Carlo (CTMC) method (see [70] and references therein). Within a classical picture, a possible triple electron scattering sequence in a collision is shown in Fig. 1 [71]. Here the displayed triple scattering sequence is denoted by P-T-P. The starting step (P) is a collision between the heavy projectile ion (moving with a velocity V) and the target electron. As a result, the electron is scattered forward with about two times the projectile velocity, $2V$. In the second step (T), the liberated electron is backscattered on the target field. Then, in Fig. 13, this T-step is followed by a third scattering on the projectile ion again (P). Finally the electron leaves the collision region with a velocity of $4V$. For kinematical reasons, the acceleration is originated exclusively from the P steps. The velocity of the electron is increased by $\sim 2V$, in every 180° electron scattering by the incoming projectile, while only the direction of its motion is changed by the scattering on the target field. Binary encounter (BE) ionization of the target is signed with P, whereas the corresponding projectile ionization (electron loss) is denoted by T. Longer sequences can be referred to as, for instance, P-T-P or T-P-T-P. Target ionization sequences start with a P process, and emit electrons up to the velocity $2nV$ in forward and backward directions (n is the number of projectile encounters). For electron loss sequences (starting with T), the final velocity is $(2n+1)V$.

Significantly enhanced emission of fast electrons far above the theoretically expected maximum (the so-called binary encounter energy) was observed in the '90-s by experimental groups in both ion-atom and ion-solid [64-67] collisions. In some cases, fast electrons have been identified as originated from double scattering of the liberated electron on the projectile and target cores [64, 65]. For the ionization of the projectile, e.g., the active electron is originally bound to the projectile ion, and it undergoes into a hard collision with the target nucleus. The scattered electron has a certain probability to suffer a second scattering on the incoming projectile core, and gain kinetic energy in this second scattering from the moving heavy projectile.

The often used name of this process is Fermi-shuttle acceleration, which refers to Fermi's idea [68] for explaining the origin of high-energy cosmic rays as acceleration of charged particles by giant magnetic fields moving in the interstellar space. The first theoretical evidence of the Fermi-shuttle acceleration in atomic collisions was found in 1991 [69] within a non-perturbative quantum mechanical model. Another non-perturbative

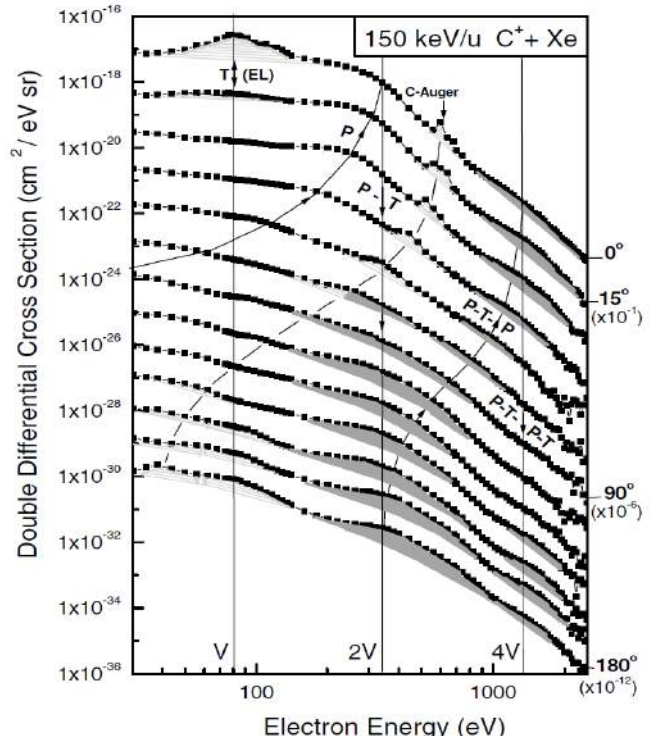


Figure 14. Experimental double differential cross section for electron emission at different observation angles in $150 \text{ keV/u } C^+ + Xe$ collisions. Lines with arrows indicate the expected location of the T, P, P-T, P-T-P, and P-T-P-T ridges. Proposed multiple scattering contributions are marked by dark gray shading. [70]

The first *triple* and *quadruple* scattering sequences has been identified in Debrecen by Sulik and coworkers [72] by using a special, high precision electron spectrometer ESA-21. Such longer sequences were later measured with higher intensities [73,74,76], also in Atomki. Later, at low projectile velocities, even longer sequences [75] have been identified. Examples of the measured double differential cross-sections exhibiting the kinematical patterns characteristic for the Fermi acceleration are shown in Figs. 14 [72] and 15 [76] for different collision systems.

In Fig. 14, the method of identification of the fast electrons produced by the Fermi shuttle mechanism was to search for extra yields on the “background” of the first order, single ionization contribution. The extra yields are indicated with the shaded areas. They nicely follow the kinematical pattern for the multiple scattering sequences at all observation angles. The absolute cross sections for the triple and quadruple scattering processes, however, were very small for this collision system (150 keV/u $C^{+} + Xe$).

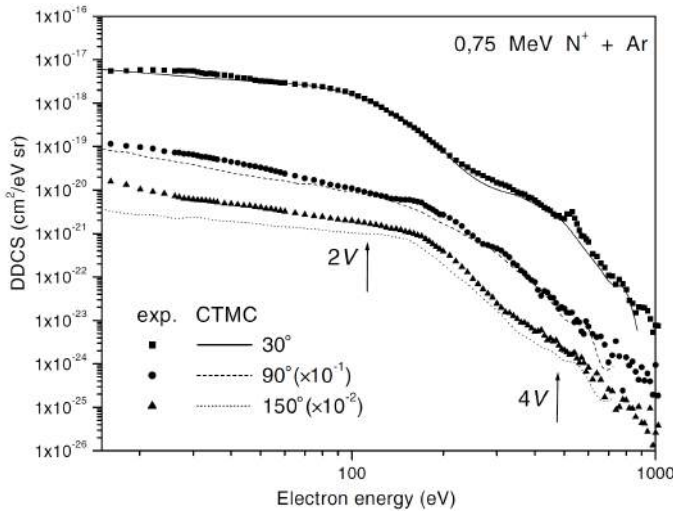


Figure 15. Double differential cross-section for electron emission at 30°, 90° and 150° observation angle in 750 keV $N^{+} + Ar$ collisions as a function of the ejected electron energy [74]. Symbols: experimental data, lines: CTMC results. Even multiples of the projectile velocity V are indicated by arrows.

In Fig. 15. a similar graph is shown for slower collisions of 53.6 keV/u N^{+} ions with Ar targets ($v_{proj} = 1.46$ au.). The expected target ionization structures (P, P-T, P-T-P and P-T-P-T) clearly appear in the spectra. For easier identification, the multiples of the projectile velocity (2V, 4V) are also indicated. The solid lines in both figures are the results of CTMC calculations. There is a remarkable agreement between the experimental data and the CTMC results [74] at 30° observation angle. Only around V and $3V$ can one find slightly lower calculated cross sections.

For Figs. 14 and 15, the experiments were carried out at the beamline of the 5 MV Van de Graaff accelerator in Atomki.. The ion beam has been directed to a gas jet target in the scattering region of a special electron spectrometer, which detects the electrons simultaneously by 13 channels between 0° and 180° relative to the beam direction, taking a complete angular distribution in one sweep. Absolute cross section data were determined by known reference cross sections.

An important feature of the CTMC calculations is that the development of the individual collision “events” can be analyzed and associated with single or multiple scattering events [75]. This way, the theoretical weights of the single and multiple scattering contributions can be derived. The observed good agreement with experiment indicates that these relative yields are realistic. By performing an extended analysis we have found that more than 60 % of the CTMC electrons, “emitted” above 250 eV in both 0.75 MeV $N^{+} + Ar$, and 1.5 MeV $N^{2+} + Ar$ collisions, could be identified as Fermi-shuttle accelerated electrons, liberated in P-T-P or P-T-P-T processes. Accelerating multiple scattering strongly contribute to the high-energy electron emission in atomic collisions at 1.5 au. projectile velocity. The contribution of the fast ($E > 250$ eV), Fermi-shuttle accelerated electrons has been found to be 4.5% of the total electron emission cross section. Since they are the most efficient in creating double strand breaks in DNA, this ping-pong effect can increase radiation damages during the deceleration of the ions in biological tissues significantly.

7. Fragmentation of biologically relevant molecules in collisions with ions

Fragmentation of water molecules by highly charged ions is of relevance in radiation damage of biological tissues, and was recently studied by different groups (many of them with Atomki collaboration) [77-80,82]. Fragment emission was found to be unisotropic in almost all fragmentation channels. In some of the channels an unexpected forward enhancement was observed, and molecular orientation sensitivity of electron transfer processes was considered as a possible origin. The aim of the studies was to understand the fundamental processes which contribute to the direct and indirect channels of radiation damage in biological tissues. The study of the fragmentation of the water molecule is especially important, since these fragments initiate a wide range of secondary processes in the cells, which finally may lead to double strand break of the DNA molecules.

In our later experiments [81], we have systematically studied the energy and angular distribution of the fragment ions from the collisions of slow, highly charged ions with water molecules. For reference, we also study the fragmentation of the H_2S molecule, which has a similar spatial structure to H_2O . We performed our experiments at the ARIBE facility in GANIL, Caen, France within the framework of an FP6 Integrated Infrastructure Initiative, the ITS-LEIF collaboration. Double differential cross sections with respect to energy and solid angle have been measured for molecule fragments. Fragmentation of H_2O and H_2S molecules were investigated by 60 keV N^{6+} and 70 keV O^{7+} impact, providing a systematics for the projectile charge. It was found that despite their similarity, H_2O and H_2S exhibit significantly different fragmentation patterns as shown in Fig. 16 and 17.

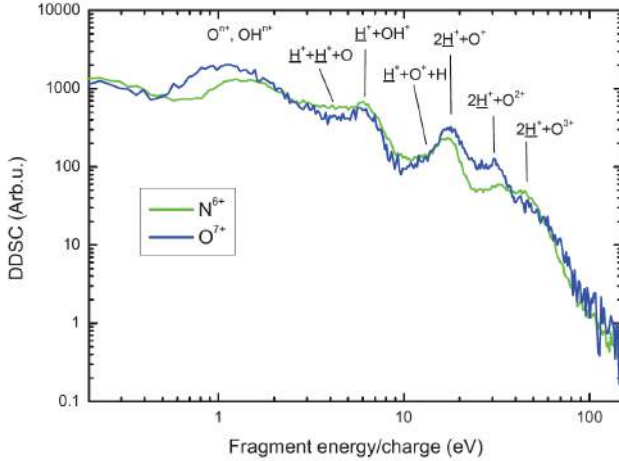


Figure 16. Energy spectra of light (proton) and heavy fragments in collision systems of 60 keV $\text{N}^{6+} + \text{H}_2\text{O}$ and 70 keV $\text{O}^{7+} + \text{H}_2\text{O}$ at 90° observation angle. [81]

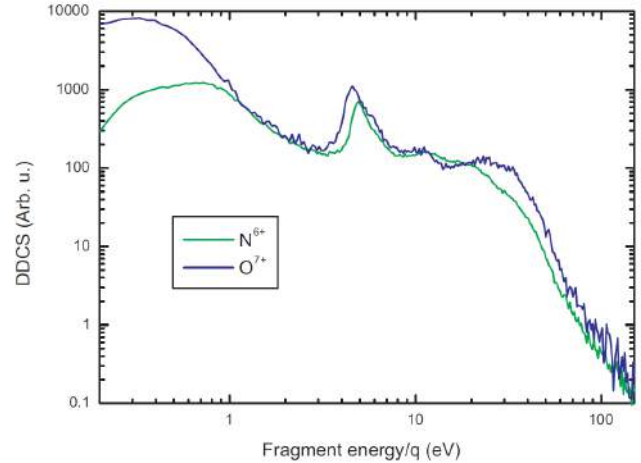


Figure 17. Energy spectra of light (proton) and heavy fragments in collision systems of 60 keV $\text{N}^{6+} + \text{H}_2\text{S}$ and 70 keV $\text{O}^{7+} + \text{H}_2\text{S}$ at 90° observation angle. [81]

We did not find anisotropies with forward enhancement for any of the fragmentation channels in the case of H_2S target. This fact would indicate that the molecular orientation effects, which are strong for the water molecule can not explained exclusively by the geometry of the molecule; water again seems to show up some special features.

Other types of anisotropies can be explained by the presence of post collision and nucleus-nucleus effects. Here the important finding is the sensitivity of the relative yields of the fragmentation channels on the projectile charge. This is clearly visible in both figures, so the strong sensitivity on the projectile charge holds for both H_2O and H_2S targets. Note that the the charge difference between the two projectiles is only 15%. It seems that some of the fragmentation channels corresponding to certain multiple ionization of the target are enhanced in the case of O^{7+} projectile, while the others are reduced. These results invited extended theoretical calculations with a partial explanation of the projectile charge effect [83].

8. Guiding of highly charged ions through insulating nanocapillaries

Guiding properties of insulating nanocapillaries have recently attracted a considerable attention. In 2002 it was discovered that ions can be effectively transmitted through capillaries in insulating polyethylene terephthalate foils with diameter to length ratio of 1/100 [84]. The front and back side of the foils were covered by metallic layers in order to avoid macroscopic charge up. Since then, different groups investigated this remarkable phenomenon [85, 86, 87]. Participants from the Atomki were involved in this research from the discovery. In 2005 experimental studies have been started at the Atomki at the Section of Atomic Collisions.

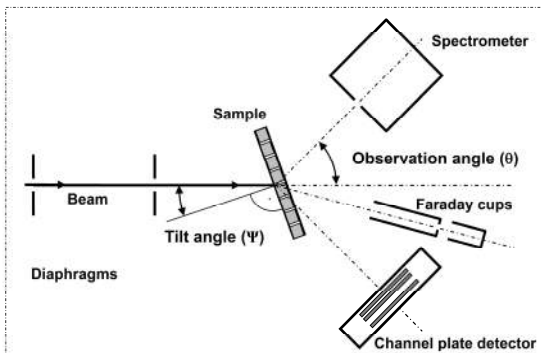


Figure 18. Experimental arrangement.

The phenomenon involves the charging up of inner capillary walls, which prevents a significant fraction of the ions getting close to the walls, i.e. they mostly preserve their initial charge state during the transmission. Due to the self organizing nature of the charge up process the transmitted ions are directed along the capillaries with a narrow angular distribution. There is

a significant transmission even if the capillaries are tilted by a relatively large tilt angle, i.e., when there is no transparency for straight line trajectories. Due to these properties, insulating nanocapillaries might find numerous applications, but in order to achieve this, a better understanding of the phenomenon is necessary.

The experiments in Atomki were performed at the beams of the electron cyclotron resonance (ECR) ion source. With low extraction voltage mode it is suitable to provide intensive beams of slow ions of charge state q in the $q \times 400$ eV – $q \times 20$ keV energy range, partly due to the short beamline construction. The highly charged ions transmitted through the capillary samples were detected by different techniques (see Figure 18).

This allowed us to study the phenomenon in wide range of incident ion intensity and for capillary samples of different porosity. As an example for the samples, high porosity Al_2O_3 capillary arrays can be seen in Figure 19. They were prepared at the Catholic University of Louvain.

In the case of high intensity beams and high porosity samples currents due to the incident ions are measured in a differential Faraday cup system. This method can be applied when the currents to be measured reach at least a few pA. By rotating the Faraday cups, angular distributions of the transmitted ions in one-dimension can be measured. The method is also suitable to measure such high currents as that of the primary beam (a few 100 pA), therefore absolute transmission through the samples can be measured.

In most of the cases the transmitted ion intensities are too low for a current measurement. Therefore we built an ion spectrometer, with which single ions can be detected. It consists of a 45° parallel plate analyzer and a channel electron multiplier. With its small opening aperture the angular distributions can be measured in one dimension by scanning the observation angle like in the case of Faraday cups. In Figure 20 angular distributions of ions transmitted through the Al_2O_3 nanocapillary samples at different tilt angles are presented. As the result of the guiding the tilt angle coincides with the center of the angular distributions. The analyzer allows us to measure accurately the energy and charge distribution of the ions also. The results presented in Figure 21 show that most of the ions kept their initial charge state during the transmission.

Recently, we installed a multi channel plate (MCP) detector in order to study the two-dimensional angular distributions of the transmitted ions. Digital signal processor based data acquisition electronics and software was developed for this detector by the Department of Electronics of Atomki. This allowed us to record two-dimensional images in time sequences, with which time dependence of the charge up process can be studied. The pulse height distribution of the MCP signals, which helps us to identify the different incident particles, is also stored for each pixel element. Compared to list mode operation, this way of data storage significantly reduced the size of the stored files without losing valuable information for this research. The developed electronics improved the limit for the speed of signal processing up to $\approx 5 \times 10^5$

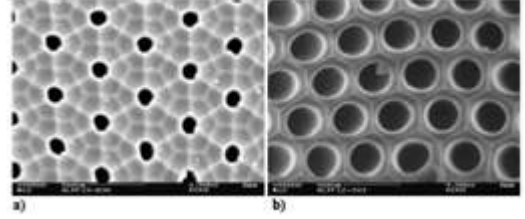


Figure 19. SEM images of the Al_2O_3 nanocapillary array samples. The diameters of the capillaries are a) $d \approx 140$ nm, b) $d \approx 260$ nm.

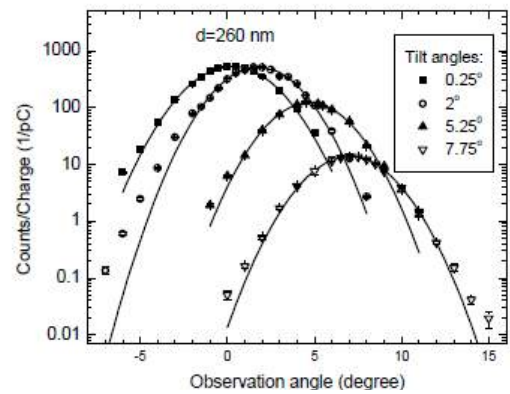


Figure 20. Angular distributions of 3 keV Ne^{6+} ions transmitted through nanocapillaries of Al_2O_3 with diameters of $d \approx 260$ nm measured by the spectrometer. The capillaries were tilted as indicated in the figure. solid lines represent Gaussian fits to the data.

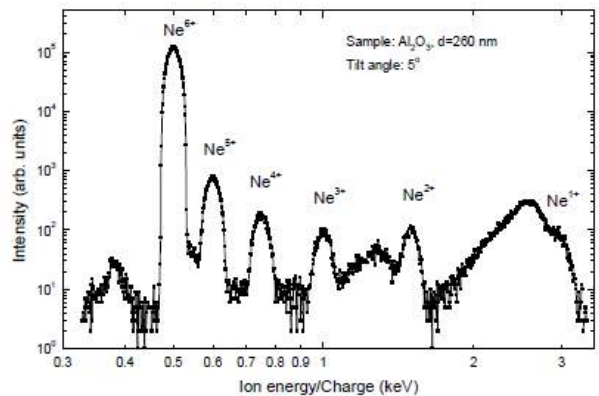


Figure 21. Charge state distribution of the ions transmitted through the 260 nm sample tilted at 5° measured by the electrostatic spectrometer. The incident beam was of 3 keV Ne^{6+} ions. Experimental arrangement.

events/s. Different charge state of the ions can be separated by applying an electric field in front of the detector. Unlike in the case of the ion spectrometer the MCP is suitable for detecting neutral particles also. In Figure 22 a picture acquired by our MCP data acquisition program is shown, where the angular distribution of Ar^{7+} ions and neutrals transmitted through a PET capillary sample can be seen.

In the course of our research, we investigated capillary samples of different materials. We were the first to show that electro chemically grown Al_2O_3 capillaries has ion guiding ability [88] similarly to capillaries in PET foils for which the discovery was made. Moreover, we observed that a relatively large fraction of the ions can be neutralized in the capillaries. In Fig. 15, only ions in their original charge state, and neutrals are visible. The fraction of ions with lower charge states is negligible [89].

In the frame of an international collaboration (ITS LEIF) we also participate in experiments at other facilities. At the KVI Groningen (Netherlands) dynamic properties of the ion transmission through PET nanocapillaries were studied by an ion spectrometer [90]. As a result of multiple charged patches developing in the capillaries an oscillatory behavior of the mean emission angle of ions was observed.

Recently we investigated also PET capillaries in Atomki by our MCP detector. Detailed studies on the time dependence of the intensity and the two dimensional angular distribution of neutrals and ions were performed. We obtained valuable information on the way of neutral formation and the time dependence of guiding process.

Within an ongoing collaboration with the Laboratory of Ion Beam Applications of Atomki, highly ordered capillary arrays with opening diameters of a few μm are produced in poly(methylmetacrylate) films by proton beam writing for the capillary guiding experiments. Characterization of other nanocapillary samples is also performed by scanning transmission ion microscopy. The combination of different techniques makes our facility a unique one to study ion guiding in nano or larger size capillaries. We will continue this work investigating different materials and going forward to the direction of applications.

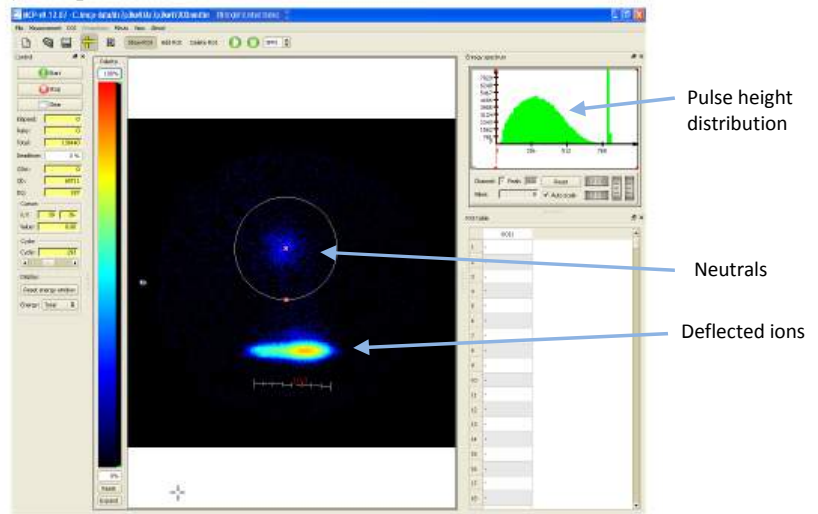


Figure 22. An MCP image by the acquisition program.

9. Theoretical description of the atomic collision processes

An important activity of the Section of Atomic Collisions is the theoretical description of the collision processes. The theoretical work is motivated partly by our own experimental observations, and partly by the results of other experimental groups. It extends also to the development of theoretical methods and tools. Remarkable results have been achieved in the following research subjects:

- 9.1 Continuum distorted wave models for energetic atomic collisions
- 9.2 Study of inner-shell ionization processes
- 9.3 Annihilation of protonium by charged particle impact
- 9.4 Classical description of the atomic collisions
- 9.5 Dynamics of collisional two-electron processes

9.1. Continuum distorted wave models for energetic atomic collisions

Variety of quantum mechanical models have been developed and applied for describing the dynamics of energetic atomic collision processes since the late sixties [91]. Amongst them are the continuum distorted wave (CDW) methods which are first order perturbative approaches where the long range properties of the Coulomb interactions are treated properly [92]. The model was proposed by Cheshire [94] and applied for electron capture and ionization by Gayet [95] and Belkic [96], respectively. Later, variants of the model were developed depending on the modified forms of the distortions used in the initial and final channels, respectively. Amongst them are the continuum distorted wave with eikonal initial-state model (CDW-EIS), where the CDW distortion of the initial channel was

replaced by its eikonal form and the symmetric eikonal (SE) model where the eikonal forms were used both in the initial and final channels (see Ref. [92]). The former proved to be very effective for treating the process of ionization, while the later received considerable interest in the treatment of excitation. Initially, the applications of the methods were restricted to the use of hydrogen-like potentials, and during the last 15 years we have generalized them by applying a more realistic model potentials for accounting the interaction between the active electron and the target core [97-100]. Since then, the numerous confrontations of the theories with the experiments and the reported quantitative agreements leads to a conclusions that, nowadays, the CDW methods becomes the most powerful approximation for describing the single electron processes in energetic atomic collisions. Description of multi-electronic processes can be given within the framework of independent electron picture (IEM). The accurate know-

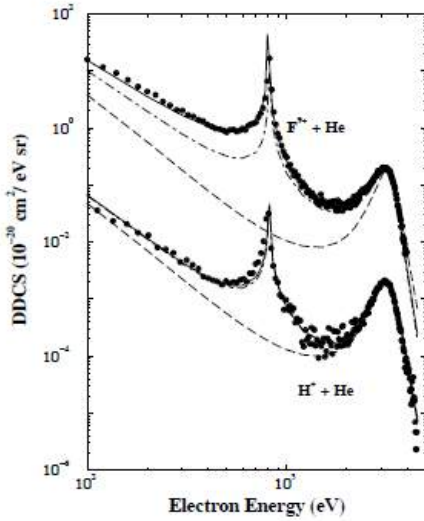


Figure 23. Doubly-differential cross section (DDCS) as a function of electron energy at fixed ejection angle of 0° , for 1 MeV/amu F^{9+} impact on He. Theory: dashed line, first Born; dot-dashed line, CDW-EIS; solid line, CDW Experiments; (\bullet) from [105].

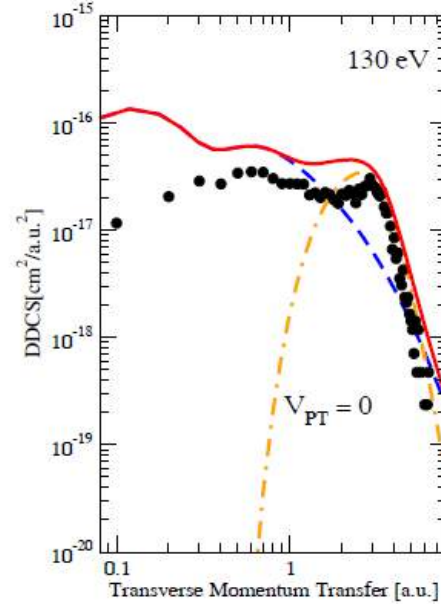


Figure 24. Doubly-differential cross section as a function of transverse momentum transfer for fixed electron energy $E_k = 130$ eV, for single ionization of He by 3.6-MeV/u Au^{53+} impact. Experiment: (\bullet), from [106]. Theory: present CDW- EIS calculations elastic channel (Dashed line); inelastic channel (dot-dashed line); elastic + inelastic channels (solid line), convoluted over detector resolution (double-dot-dashed line).

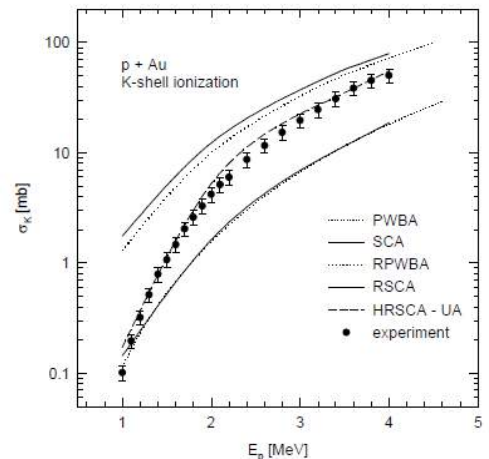
ledge of the one-electron transition probabilities, which is the essential requirement in the IEM, have also been in the focus of our studies [101-112]. Figures 23 and 24 illustrate two examples of the applications of the theorems [99, 103], see also [104] for other applications.

9.2. Study of inner-shell ionization processes

This work started at the beginning of the 1980's years. It was motivated by our x-ray experiments carried out at the 5-MV Van de Graaff accelerator of Atomki by using protons, alpha particles and heavier ions (C^+ , N^+ , O^+). We used the first-Born approximation (plane-wave Born approximation, PWBA) for the calculations of K- and L-shell ionization cross sections. We found that PWBA is incapable of the reproduction of the measured data for the L-shell ionization by heavy-ion impact [14].

The search for the reason of the discrepancy led to the dis-

Figure 25. K-shell ionization cross sections for gold bombarded by protons as a function of the incident energy.



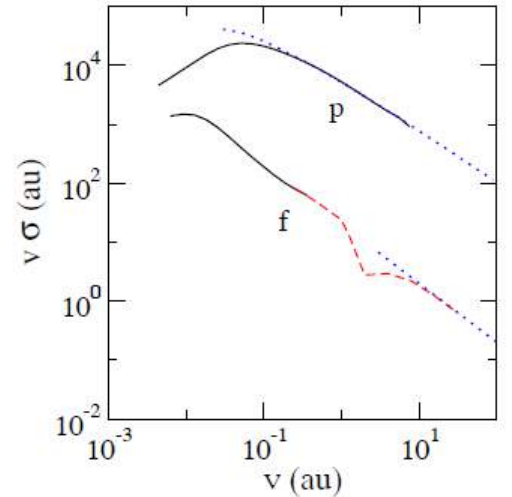
covery of an interesting effect, known as “subshell coupling effect” [15-17]. This is a result of a higher-order process that occurs when the perturbation expansion parameter Z_1/v (here Z_1 is the charge of the projectile and v is the collision velocity) is not a negligibly small quantity (in atomic units).

A recent important result in the field of the inner-shell ionization is the development of two computer codes that calculate the bound–free matrix elements of the Coulomb interaction with use of non-relativistic [18] and relativistic [19] hydrogenic wave functions, respectively. An example of the application of the relativistic code is shown in Figure 25. Our calculation (the curve denoted by HRSCA-UA) is in good agreement with the experimental data [20].

9.3. Annihilation of protonium by charged particle impact

Protonium (Pn) annihilates almost instantaneously when its initial high- l states (l denotes the angular momentum) are transferred to the low-lying s , p or d states. In our recent studies [107, 108], the annihilation of Pn induced by electron or bare ion impact is described by quantal and semi-classical close-coupling methods, where the scattering wave functions are expanded in terms of Pn orbitals. These calculations show that at low projectile velocities intrashell transitions dominate the process, while, at high impact velocities the transitions between different shells must also be taken into account. Two different collision mechanisms, dipole and sudden, are found to dominate the process in the range of medium and high impact velocities, respectively.

Figure 26. Annihilation cross sections times impact velocity (v) for the $p + \text{Pn}(n_0 l_0)$ collisions ($n_0 = 100$, $l_0 = 1$ and 3). Cross-sections are obtained by using the *dipole* (solid line), *sudden* (dashed line) scaling rules. Dotted lines are cross sections obtained by the σ_{B1} approximation (see [108]).



Scaling of the annihilation cross sections with n is discussed in relation to the scaling properties of coupling matrix elements. Figure 26 shows an example of the annihilation cross sections for the $p + \text{Pn}(n_0 l_0)$ collision when $n_0 = 100$ and $l_0 = 1$ and 3. These cross sections are evaluated on the basis of different scaling formulas.

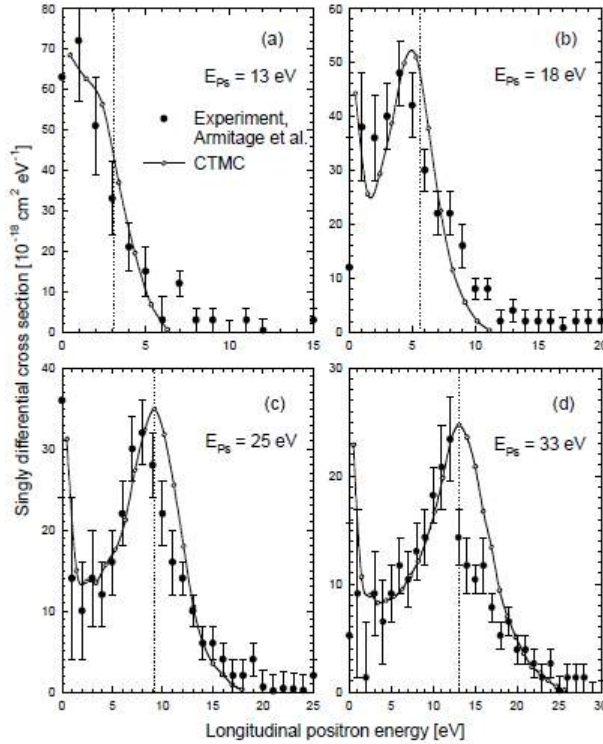
9.4. Classical description of the atomic collisions

Classical models for atomic collisions has a long tradition in our work. A simple classical „geometrical” model was developed in the ’80-s, and has been used successfully [109-111] for the treatment of multiple ionization in energetic ion-atom collisions. In the past few years we frequently used a more developed classical method for the description of the atomic collisions. The applied theory is the classical trajectory Monte Carlo (CTMC) model [21, 70]. Although it is a classical approach, it proved to be a very efficient method for the treatment of the collision problems. CTMC is based on the numerical solution of Newton’s classical equations of motion for a large number of trajectories under randomly chosen initial conditions. The model describes the motion of all particles classically. The initial bound electronic states of the target (and/or projectile) are represented by elliptic Kepler orbits. In addition to its use in the treatment of the Fermi-shuttle process [70-76], in the following we demonstrate the efficiency of the method by its application to the treatment of the collisional fragmentation of positronium.

9.4.1. Fragmentation of positronium in collision with He atoms

This work [22] is connected to an experiment in which Armitage et al. [23] carried out a first measurement of absolute break-up cross sections for the fragmentation of positronium (Ps) in collision with He atoms in the energy range between 13 and 33 eV. In addition to the measurement of total cross sections, they determined also the longitudinal energy distributions of the emitted positrons. A remarkable feature of the obtained positron spectra is a peak appearing just below 50% of the residual Ps energy ($E_{\text{res}} = E_{\text{Ps}} - 6.8$ eV). The peak was interpreted as an analogy of the electron loss to the continuum (ELC) peak appearing in the energy spectrum of the electrons ejected in the forward direction in ion–atom (atom–atom) collisions.

We applied the classical trajectory Monte Carlo (CTMC) method to the description of the collisional fragmentation of PS. The collision system was simplified to a three-body system consisting of the electron and the



positron of Ps, as well as the He atom that was considered as a structureless particle. Our model correctly reproduced the peak observed in the longitudinal positron spectra (see Figure 27), supporting a peak formation mechanism similar to the ELC process in atomic collisions.

Figure 27. Longitudinal energy distributions of the positrons emitted in Ps + He collisions for $E_{Ps}=13$, 18, 15 and 33 eV. The experimental data (full circles, Armitage et al. [23]) are normalized to the maxima of the theoretical curves calculated by the present CTMC model. The vertical dotted line shows the expected peak position, $E_{res}/2$.

9.5. Dynamics of two electron processes

The dynamics of electron-electron interaction in atomic collisions is one of the fundamental areas in atomic collision physics. The study of two electron processes provides the easiest way to understand these complicated phenomena. We have a long history to study collision systems both theoretically and experimentally, by the method of the spectroscopy of electrons originating from the target and the projectile. One of the most important examples is the two-electron cusp (See Chapter 2.2 above). Here we provide only a list of the other topics, where we have contributed to this field: Two-center electron-electron interactions [112,122], time ordering in two-electron transitions [113-116], dynamic correlation in dielectronic transitions [117,118], transfer ionization in cusp electron production [119,120] and the analysis of the so called transfer-loss process at low impact energies [121, 123-125]. This line of (mostly) theoretical studies was very important for finding the ways to study more complex systems, and to become integrated into the the collision community at the frontiers of that research direction.

10. Summary

We hope that the present selection provides the reader with a flavor of the atomic collision physics research performed in our Section. It is seen that we have a strong interest in fundamental processes. It is also seen that the research work in the field is developing from the basic study of simple systems to different directions. One of them goes towards a deeper understanding of simple systems and fundamental processes. The other direction is the analysis of complex, sometimes strange phenomena, up to the study of mesoscopic effects governed by atomic collision processes. Moreover, new experimental facilities and possibilities (e.g., the availability of antiparticles) are always a challenge to start into a new direction. Finally, as our community gets better equipped for handling complex problems, we are turning to study systems, which are related to applied sciences and direct applications. We believe that these are all natural ways to find the future of the field of atomic collision physics.

11. Acknowledgements

We express our gratitude to the former members of the Section and its predecessors, or who are on a longer leave. They helped to establish this line of research in Atomki, and contributed to the research work in the field during many years: Erika Bene, István Cserny, Gábor Hock, Imre Kádár, Károly Kiss, László Kövér, Bálint Schlenk[†], Gyula Szabó, Endre Takács, József Tóth, Aladár Valek, János Vámosi, Endre Vatai[†], János Végh and László Végh;

To our Ph.D. students: Attila Báder, Éva Fekete, István Iván, Lajos Kenéz, Csaba Koncz, László Lugosi, Péter Nábrádi, László Nagy, Béla Paripás, Csilla Szabó, Ernő Szmola, Tibor Suta, László Tóth, Tibor Vajnai, György Víkor, Liljana Víkor and Péter A. Závodszy;

To our technician Lajos L. Horváth, and technicians during the years: Márta Halász, Erzsébet Bene, László Barta, Ferenc Gáll[†] and József Köblös;

To the engineers, to the staff of the accelerators and the workshops, and to all helpful colleagues;

Last but not least we express our thanks for all our external collaborators, and acknowledge the continuous help of the international community of atomic collision physicists.

References

- [1] S. A. H. Seif El-Nasr, D. Berényi and Gy. Bibók, *Z. Phys.* **267** (1974) 169 and *ibid* **271** (1974) 207.
- [2] G. B. Crooks and M. E. Rudd, *Phys. Rev. Lett.* **25** (1970) 1599.
- [3] E. P. Wigner, *Phys. Rev.* **73** (1948) 1002.
- [4] L. Sarkadi, J. Pálinkás, Á. Kövér, D. Berényi and T. Vajnai, *Phys. Rev. Lett.* **62** (1989) 527.
- [5] L. Sarkadi, M. Kuzel, L. Víkor, P. A. Závodszy, R. Maier, D. Berényi and K. O. Groeneveld, *Nucl. Instrum. Methods. B* **124** (1997) 335.
- [6] M. Kuzel, L. Sarkadi, J. Pálinkás, P. A. Závodszy, R. Maier, D. Berényi and K. O. Groeneveld, *Phys. Rev. A* **48** (1993) R1745.
- [7] A. Báder, L. Sarkadi, L. Víkor, M. Kuzel, P. A. Závodszy, T. Jalowy, K. O. Groeneveld, P. A. Macri and R. O. Barrachina, *Phys. Rev. A* **55** (1997) R14.
- [8] L. Víkor, L. Sarkadi, F. Penent, A. Báder and J. Pálinkás, *Phys. Rev. A* **54** (1996) 2161.
- [9] L. Víkor and L. Sarkadi, *Phys. Rev. A* **55** (1997) R2519.
- [10] R. O. Barrachina, *J. Phys. B: At. Mol. Opt. Phys.* **23** (1990) 2321.
- [11] L. Sarkadi, K. Tókési and R. O. Barrachina, *J. Phys. B: At. Mol. Opt. Phys.* **33** (2000) 847.
- [12] G. H. Wannier, *Phys. Rev.* **90** (1953) 817.
- [13] L. Sarkadi and A. Orbán, *Phys. Rev. Lett.* **100** (2008) 133201.
- [14] L. Sarkadi and T. Mukoyama, *J. Phys. B: At. Mol. Phys.* **13** (1980) 2255.
- [15] L. Sarkadi and T. Mukoyama, *J. Phys. B: At. Mol. Phys.* **14** (1981) L255.
- [16] L. Sarkadi and T. Mukoyama, *Nucl. Instrum. and Meth. B* **4** (1984) 296.
- [17] L. Sarkadi, *J. Phys. B: At. Mol. Phys.* **19** (1986) L755.
- [18] L. Sarkadi, *Comp. Phys. Commun.* **133** (2000) 119.
- [19] L. Lugosi and L. Sarkadi, *Comp. Phys. Commun.* **141** (2001) 73.
- [20] M. Kamiya, K. Ishii, K. Sera and H. Tawara, *Phys. Rev. A* **16** (1977) 2295.
- [21] R. Abrines and I. C. Percival, *Proc. Phys. Soc. London* **88** (1966) 861.
- [22] L. Sarkadi, *Phys. Rev. A* **68** (2003) 032706.
- [23] S. Armitage D. E. Leslie, A. J. Garner, and G. Laricchia, *Phys. Rev. Lett.* **89** (2002) 173402-1.
- [24] P. Schlemmer, T. Rosel, K. Jung, and H. Ehrhardt, *Phys. Rev. Lett.* **63** (1989) 252.
- [25] R. Dörner, V. Mergel, O. Jagutzki, L. Spielberger, J. Ullrich, R. Moshhammer, and H. Schmidt-Böcking, *Physics Reports* **330** (2000) 95.
- [26] Á. Kövér, G. Laricchia and M. Charlton, *J. Phys. B: At. Mol. Opt. Phys.* **26** (1993) L575.
- [27] Á. Kövér, G. Laricchia, and M. Charlton, *J. Phys. B* **27** (1994) 2409.
- [28] Á. Kövér, R. M. Finch, M. Charlton, and G. Laricchia, *J. Phys. B* **30** (1997) L507.
- [29] Á. Kövér and G. Laricchia, *Phys. Rev. Lett.* **80** (1998) 5309.
- [30] Á. Kövér, K. Paludan, and G. Laricchia, *J. Phys. B: At. Mol. Opt. Phys.* **34** (2001) L219.
- [31] C. Arcidiacono, Á. Kövér, G. Laricchia, *Phys. Rev. Lett.* **95** (2005) 223202.
- [32] C. Arcidiacono, J. Beale, Z. D. Pešić, Á. Kövér, and G. Laricchia, *J. Phys. B: At. Mol. Opt. Phys.* **42** (2009) 065205.
- [33] M. Brauner, J. S. Briggs, *J. Phys. B: At. Mol. Opt. Phys.* **24** (1991) 2227.
- [34] Á. Kövér and G. Laricchia, *Meas. Sci. Technol.* **12** (2001) 1875.
- [35] R. A. Sparrow, and R. E. Olson, *J. Phys. B: At. Mol. Opt. Phys.* **27** (1994) 2647.
- [36] Berakdar J., *Phys. Rev. Lett.* **81** (1998) 1393.
- [37] J. Fiol, V. D. Rodriguez, and R. O. Barrachina, *J. Phys. B* **34** (2001) 933.
- [38] Á. Kövér, D. J. Murtagh, A. I. Williams, and G. Laricchia, *J. Phys: Conference Series* **199** (2010) 012020(5).
- [39] K. L. Baluja, R. Zhang, J. Franz, and J. Tennyson, *J. Phys. B: At. Mol. Opt. Phys.* **40** (2007) 3515.
- [40] C. G. Ning, B. Hajgato, Y. R. Huang, S. F. Zhang, K. Liu, Z. H. Luo, S. Knippenberg, J. K. Deng, and M. S. Delueze, *Chem. Phys* **343** (2008) 19.
- [41] S. Riez, Á. Kövér, M. Jurvansuu, D. Varga, J. Molnár, and S. Aksela, *Phys. Rev. A* **65** (2002) 042707.
- [42] S. Riez, R. Sankari, Á. Kövér, M. Jurvansuu, D. Varga, J. Nikkinen, T. Ricsóka, H. Aksela, S. Aksela, *Phys. Rev. A* **67** (2003) 012712.

- [43] W. R. Johnson, and K. T. Cheng, *Phys. Rev. A* **63** (2001) 022504.
- [44] M. Ya. Amusia, A. S. Baltenkov, L. V. Chernysheva, Z. Felfli, and A. Z. Msezane, *Phys. Rev. A* **63** (2001) 052506.
- [45] D. Toffoli, M. Stener, and P. Decleva, *J. Phys. B* **35** (2002) 1275.
- [46] O. Hemmers, S. T. Manson, M. M. Sant'Anna, P. Focke, H. Wang, I. A. Sellin, and D. W. Lindle, *Phys. Rev. A* **64** (2001) 022507.
- [47] A. Derevianko, W. R. Johnson, and K. T. Cheng, *At. Data and Nucl. Data Tables* **73** (1999) 153.
- [48] S. Ricz, J. Nikkinen, R. Sankari, T. Ricsóka, Á. Kövér, D. Varga, S. Fritzsche, H. Aksela, and S. Aksela, *Phys. Rev. A* **72** (2005) 014701.
- [49] T. W. Gorczyca and F. Robicheaux, *Phys. Rev. A* **60** (1999) 1216.
- [50] S Fritzsche, *J. E.I Spect Rel Phenom.* **114** (2001) 1155.
- [51] G. C. King, M. Tronc, F. H. Read, and R. C. Bradford, *J. Phys. B* **10** (1977) 2479.
- [52] S. Ricz, T. Ricsóka, Á. Kövér, D. Varga, M. Huttula, S. Urpelainen, H. Aksela and S. Aksela, *New J. Phys.* **9** (2007) 274.
- [53] T. Ricsóka, S. Ricz, Á. Kövér, S. Schippers, K. Holste, A. Borovik Jr., D. Varga and A. Müller, *Journal of Physics: Conference Series* **194** (2009) 2051.
- [54] Stolterfoht N., Chesnel J. -Y., Grether M., Skogvall B., Frémont F., Lecler D., Hennecart D., Husson X., Grandin J. P., Sulik B., Gulyás L., Tanis J. A., *Phys. Rev. Lett.* **80** (1998) 214649.
- [55] Stolterfoht N., Chesnel J. -Y., Grether M., Tanis J. A., Skogvall B., Frémont F., Lecler D., Hennecart D., Husson X., Grandin J. P., Koncz Cs., Gulyás L., Sulik B., *Phys. Rev. A* **59** (1999) 2:1262.
- [56] Tanis J. A., Chesnel J. -Y., Frémont F., Hennecart D., Husson X., Cassimi A., Grandin J. P., Skogvall B., Sulik B., Bremer J-H., Stolterfoht N., *Phys. Rev. Lett.* **83** (1999) 6:1131.
- [57] Stolterfoht N, Sulik B, Hoffmann V, Skogvall B, Chesnel J-Y, Rangama J, Frémont F, Hennecart D, Cassimi A, Husson X, Landers AL, Tanis JA, Galassi ME, Rivarola RD, *Phys. Rev. Lett.* **87** (2001) 023201.
- [58] Stolterfoht N., Sulik B., Gulyás L., Skogvall B., Chesnel J. -Y., Frémont F., Hennecart D., Cassimi A., Adoui L., Hossain S., Tanis J. A. , *Phys. Rev. A* **67** (2003) 03702.
- [59] Stolterfoht N., Sulik B., *Advances in Quantum Chemistry* **46** (2004) 307.
- [60] Sulik B., Tanis J. A., Chesnel J. -Y., Stolterfoht N., *Physica Scripta T* **110** (2004) 345.
- [61] Stolterfoht N., Sulik B., Skogvall B., Chesnel J. -Y., Frémont F., Hennecart D., Cassimi A., Adoui L., Hossain S., Tanis J. A., *Phys. Rev. A* **69** (2004) 012701.
- [62] Tanis J. A., Hossain S., Sulik B., Stolterfoht N., *Phys. Rev. Lett.* **95** (2005) 079301.
- [63] Tanis J. A., Chesnel J. -Y, Sulik B., Skogvall B., Sobocinski P., Cassimi A, Grandin J. P., Adoui L, Hennecart D, Stolterfoht N., *Phys. Rev. A* **74** (2006) 022707.
- [64] Suárez S, Barrachina R O and Meckbach W, *Phys. Rev. Lett.* **77** (1996) 474.
- [65] Bechthold U, Hagmann S, Ullrich J, Bathelt B, Bohris A, Moshammer R, Ramm U, Bhalla C, Kraft G, Schmidt-Böcking H, *Phys. Rev. Lett.* **79** (1997) 2034.
- [66] Lanzano G, De Filippo E, Mahboub D, Rothard H, Aiello A, Anzalone A, Cavallaro S, Elanique A, Geraci E, Geraci M, Giustolisi F, Pagano A, Politi G, *Phys. Rev. Lett.* **83** (1999) 4518.
- [67] Sulik B, Kövér Á, Ricz S, Koncz C, Tökési K, Víkor Gy, Chesnel J Y, Stolterfoht N, Berényi D, *Phys. Scr. T* **80** (1999) 338.
- [68] Fermi E *Phys. Rev.* **75** (1949) 1169.
- [69] Wang J, Burgdörfer J and Bárányi A, *Phys. Rev. A* **43** (1991) 4036.
- [70] Sulik B., Tökési K., *Advances in Quantum Chemistry* **52** (2007) 253.
- [71] Sulik B, Stolterfoht N, Hellhammer R, Pesic Z, Koncz Cs, Tökési K and Berényi D, *Nucl. Inst. and Meth. B* **212** (2003) 32.
- [72] Sulik B, Koncz Cs, Tökési K, Orbán A and Berényi D, *Phys. Rev. Lett.* **88** (2002) 073201.
- [73] Sulik B, Tökési K, Koncz Cs, Kövér Á, Ricz S, Orbán A, Stolterfoht N, Chesnel J-Y and Berényi D, *Phys. Scr. T* **92** (2001) 463.
- [74] Ricsóka T, Víkor Gy, Nagy Sz, Tökési K, Berényi Z, Paripás B, Stolterfoht N, Sulik B, *Nucl. Instr. Meth. B.* **235** (2005) 397.
- [75] Tökési K, Sulik B, Stolterfoht N, *Nucl. Instr. Meth. B.* **233** (2005) 187.
- [76] Sulik B., Tökési K., Stolterfoht N., Ricsóka T., Víkor Gy., Nagy Sz., Berényi Z., Hellhammer R., Pesic Z., Berényi D. , *Radiation Physics and Chemistry* **76** (2007) 483.
- [77] Pesic Z. D., Chesnel J. -Y., Hellhammer R., Sulik B., Stolterfoht N., *J. Phys. B* **37** (2004) 1405.
- [78] Serebyuk B, McCullough RW, Tawara H, Gilbody HB, Bodewits D, Hoekstra R, Tielens AGGM, Sobocinski P, Pesic Z, Hellhammer R, Sulik B, Stolterfoht N, Abuhaija O, Kamber E. Y, *Phys. Rev. A* **71** (2005) 022705.
- [79] Sobocinski P., Pesic Z.D., Hellhammer R., Stolterfoht N., Sulik B., Legendre S., Chesnel J. -Y., *J. Phys. B* **38** (2005) 2495.
- [80] Sobocinski P., Pesic Z.D., Hellhammer R., Stolterfoht N., Chesnel J. -Y., Legendre S, Sulik B., *Nucl. Instr. Meth. B* **233** (2005)207.
- [81] Juhász Z., Sulik B., Frémont F., Hajaji A., Chesnel J. – Y, *Nucl. Instr. Meth. B* **267** (2009) 326.
- [82] Pesic Z. D., Hellhammer R., Sulik B. , Stolterfoht N, *J. Phys.B* **42** (2009) 5202.
- [83] Guevara N. L. et al., *Phys. Rev. A* **80** (2009) 062715.

- [84] N. Stolterfoht, J.-H. Bremer, V. Hoffmann, R. Hellhammer, D. Fink, A. Petrov, B. Sulik, *Phys. Rev. Lett.* **88** (2002) 13320.
- [85] M.B. Sahana, P. Skog, Gy. Viktor, R. T. Rajendra Kumar, R. Schuch, *Phys. Rev. A* **73** (2006) 040901R.
- [86] Y. Kanai, M. Hoshino, T. Kambara, T. Ikeda, R. Hellhammer, N. Stolterfoht, Y. Yamazaki, *Nucl. Instrum Methods B* **258** (2007) 155.
- [87] R.J. Berezky, G. Kowarik, F. Aumayr, K. Tokési, *Nucl. Instr. and Meth. B* **267** (2009) 317.
- [88] S. Mátéfi-Tempfli, M. Mátéfi-Tempfli, L. Priaux, Z. Juhász, S. Biri, É. Fekete, I. Iván, F. Gáll, B. Sulik, Gy. Viktor, J. Pálíns, N. Stolterfocht, *Nanotechnology* **17** (2006) 3915.
- [89] Z. Juhász, B. Sulik, S. Biri, I. Iván, K. Tökési, É. Fekete, S. Mátéfi-Tempfli, M. Mátéfi-Tempfli, Gy. Viktor, E. Takács, J. Pálíns, *Nucl. Instr. and Meth. B* **267** (2009) 321.
- [90] N. Stolterfoht, R. Hellhammer, D. Fink, B. Sulik, Z. Juhász, E. Bodewits, H. M. Dang, R. Hoekstra, *Phys. Rev. A* **79** (2009) 022901.
- [91] D. P. Dewangan and J. Eichler, *Phys. Rep.* **247** (1994) 59.
- [92] D. S. F. Crothers and L. Dubé, *Adv. At. Mol. Opt. Phys.* **30** (1993) 287.
- [93] N. Stolterfoht, R. D. DuBois, and R. D. Rivarola, *Electron Emission in Heavy Ion-Atom Collisions* (Springer-Verlag, Berlin, 1997).
- [94] I. M. Cheshire, *Proc. Phys. Soc.* **84** (1964) 89.
- [95] R. Gayet, *J. Phys. B* **5** (1972) 483.
- [96] Dž. Belkic, *J. Phys. B* **11** (1978) 3529.
- [97] L. Gulyás, P. D. Fainstein, and A. Salin, *J. Phys. B.: At. Mol. Phys.* **27** (1995) 245.
- [98] L. Gulyás, and P. D. Fainstein, *Phys. Rev. A* **56** (1997) 1321.
- [99] L. Gulyás, and P. D. Fainstein, *J. Phys. B.: At. Mol. Phys.* **31** (1998) 3297.
- [100] L. Gulyás, P. D. Fainstein, and T. Shirai, *Phys. Rev. A* **65** (2002) 052720.
- [101] P. D. Fainstein, L. Gulyás, and A. Salin, *J. Phys. B: At. Mol. Phys.* **29** (1996) 1225.
- [102] P. D. Fainstein, L. Gulyás, and A. Dubois, *J. Phys. B: At. Mol. Phys.* **31** (1998) L171.
- [103] P. D. Fainstein, and L. Gulyás, *J. Phys. B: At. Mol. Phys.* **38** (2005) 317.
- [104] T. Kirchner, L. Gulyás, H. J. Lüdde, A. Henne, E. Engel, and R. M. Dreizler, *Phys. Rev. Lett.* **79** (1997) 1658.; L. Gulyás, P. D. Fainstein, and T. Shirai, *J. Phys. B.: At. Mol. Phys.* **34** (2001) 1473. ; L. Gulyás, and T. Kirchner, *Phys. Rev. A* **70** (2004) 022704. ; L. Gulyás, A. Igarashi, and T. Kirchner, *Phys. Rev. A* **74** (2006) 032713. ; L. Gulyás, A. Igarashi, and P. D. Fainstein, *J. Phys. B.: At. Mol. Phys.* **41** (2008) 025202.
- [105] D. H. Lee, P. Richard, T. J. M. Zouros, J. M. Sanders, J. M. Shinpaugh, and H. Hidmi, *Phys. Rev. A* **24** (1990) 97.
- [106] R. Moshhammer, A. Perumal, M. Schulz, V. D. Rodríguez, H. Kollmus, R. Mann, S. Hagmann, and J. Ullrich, *Phys. Rev. Lett.* **87** (2001) 223201.
- [107] A. Igarashi, and L. Gulyás, *J. Phys. B.: At. Mol. Phys.* **42** (2009) 035201.
- [108] L. Gulyás, A. Igarashi, and A. Ohsaki, *J. Phys. B.: At. Mol. Phys.* **43** (2010) 055203.
- [109] Sulik B., Hock G., Berényi D., *J. Phys. B* **17** (1984) 3239
- [110] Sulik B., Kádár I., Ricz S., Varga D., Végh J., Hock G., Berényi D., *Nucl. Instr. Meth. B* **28** (1987) 509
- [111] Sulik B., Török I., Ágoston A., Kádár I., *Nucl. Instr. Meth. B* **56** (1991) 45.
- [112] Ricz S., Sulik B., Stolterfoht N., Kádár I., *Phys. Rev. A* **47** (1993) 1930.
- [113] Stolterfoht N, Mattis A, Schneider D, Schiwietz G, Skogvall B, Sulik B, Ricz S, *Phys. Rev. A* **51** (1995) 350.
- [114] Sulik B., Ricz S., Kádár I., Xiao G, Schiwietz G, Sommer K, Grande P, Köhrbrück R., Grether M, Stolterfoht N., *Phys. Rev. A* **52** (1995) 387.
- [115] Végh L., Sulik B., Stolterfoht N., *Phys. Rev. A* **51** (1995) 3017.
- [116] Nagy L., McGuire J. H., Végh L., Sulik B., Stolterfoht N., *J. Phys. B* **30** (1997) 1939.
- [117] Chesnel J.-Y, Sulik B, Merabet H, Bedouet C, Frémont F, Husson X, Grether M, Spieler A, Stolterfoht N., *Phys. Rev. A* **57** (1998) 053546.
- [118] Chesnel J. -Y., Merabet H, Sulik B., Frémont F., Bedouet C, Husson X, Grether M., Stolterfoht N., *Phys. Rev. A* **58** (1998) 042935.
- [119] L. Sarkadi, L. Lugosi, K. Tökési, L. Gulyás and Á. Kövér, *Journal of Physics B* **34** (2001) 4901.
- [120] L. Viktor, P. Závodszy, L. Sarkadi, J. A. Tanis, M. Kuzel, A. Báder, J. Pálíns, E. Y. Kamber, D. Berényi and K. O. Groeneveld, *Journal of Physics B* **28** (1995) 3915.
- [121] Sulik B., Zouros T. J. M., Orbán A., Gulyás L., *J. El. Spectr. Rel. Phenom.* **114** (2001) 191.
- [122] A. Orbán, B. Sulik, *Comp. Phys. Comm.* **151** (2003) 199.
- [123] Orbán A., Zouros T. J. M., Sulik B., *Nucl. Instr. Meth. B* **205** (2003) 464.
- [124] Zouros T. J. M., Sulik B., Gulyás L., Orbán A., *J. Phys. B* **39** (2006) 45.
- [125] Zouros T. J. M., Sulik B., Gulyás L., Tökési K., *Phys. Rev. A* **77** (2008) 05701.
- [126] Kövér Á., Sarkadi L., Pálíns J., Berényi D., Szabó Gy., Vajnai T., Heil O., Groeneveld K. O., Gibbons J., Sellin I. A.: *J. Phys. B* **22** (1989) 1595.
- [127] Tökési K., Kövér Á., *J. Phys. B* **33** (2000)3067

1.1 Exactly solvable potentials with finite positive position-dependent mass

G. Lévai, O. Özer^{a)}

Quantum mechanical potential problems with position-dependent mass occur in various branches of physics. There have been considerable efforts recently to obtain the exact analytical solution of the Schrödinger equation with various effective masses, but the results are less numerous and less systematic than in the case of constant-mass potential problems. The quantum mechanically acceptable one-dimensional position-dependent mass problems can be transformed to the form

$$\left(-\frac{d}{dx} \frac{1}{M(x)} \frac{d}{dx} + V_{\text{eff}}(x)\right) \psi(x) = E\psi(x). \quad (1)$$

The procedure of solving this equation is usually done by adapting the methods applied in the constant mass case, i.e. Eq. (1) is transformed to the differential equation of some F special function of mathematical physics by substituting $\psi(x) = f(x)F(g(x))$. The $g(x)$ function maps the domain of definition of ψ to that of F in a monotonous way. The mass function $M(x)$ also has to be included in this procedure, and in the previous works it has been defined in terms of the derivative of $g(x)$. Since $g(x)$ and $g'(x)$ are usually not bound and can be zero, the resulting mass function also has these features typically. The physical interpretation of the zeros and the singularities of $M(x)$ usually need some kind of justification, but it may not be compatible with the actual physical nature of the problem.

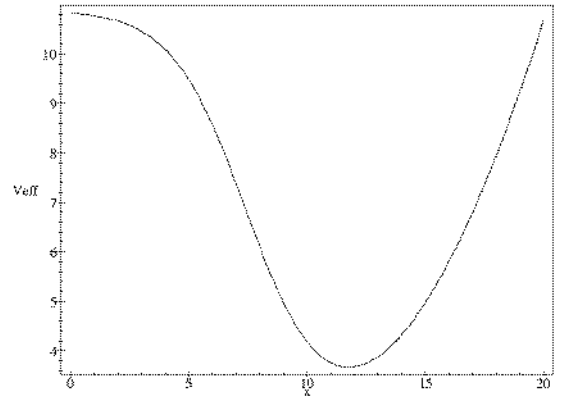
Recently we generalized the procedure of solving the position-dependent mass Schrödinger equation in a way that guarantees that $M(x)$ remains finite and positive everywhere [1]. We developed the formalism for the generalized Laguerre polynomials $F(g) = L_n^{(\alpha)}(g)$ and considered the mass function $M(g(x)) = M_0(\gamma + g(x))(\delta + g(x))^{-1}$. The $g(x)$ function was defined by $g'(x) = g(x)[B(\delta + g(x))]^{-1/2}$, which contains as special cases the $g(x)$ functions generating the harmonic oscillator ($\delta = 0$) and the Morse potential ($\delta \rightarrow \infty$, $B\delta = \text{const.}$). Integrating

$g'(x)$ results in an implicit $x(g)$ function

$$x + K = (B\delta)^{1/2} \ln \left(\frac{(\delta + g)^{1/2} - \delta^{1/2}}{(\delta + g)^{1/2} + \delta^{1/2}} \right) + 2B^{1/2}(\delta + g)^{1/2}. \quad (2)$$

The resulting $V_{\text{eff}}(g(x))$ potential also depends on x in an implicit way, nevertheless, the physically relevant quantities can be obtained exactly. The potential depends on four parameters (B , γ , δ and d) and combines the properties of the harmonic oscillator ($x \rightarrow \infty$, small n) and the Morse potential ($x \rightarrow -\infty$, $n \sim n_{\text{max}}$). The bound-state energy eigenvalues are

$$E_n = \frac{1}{B} \left(n + \frac{1}{2} - \frac{\gamma}{4} + \sqrt{\frac{1}{16} - d - \gamma n - \frac{\gamma}{2}} \right). \quad (3)$$



The constant mass case is obtained for $\gamma = \delta$. The potential then contains both the harmonic oscillator and the Morse potentials as special cases, similarly to the generalized Coulomb problem [2], which contains the harmonic oscillator and the Coulomb potential.

The method can be generalized in several ways, which may allow tailoring the effective potential to realistic physical situations.

^{a)} University of Gaziantep, Gaziantep, Turkey

[1] G. Lévai, O. Özer, submitted to J. Math. Phys.

[2] G. Lévai, B. Kónya, Z. Papp, J. Math. Phys. 39 (1998) 5811.

1.2 Asymptotic iteration method to bound-state problems with unbroken and broken supersymmetry

O. Özer^{a)}, G. Lévai

Obtaining the exact solutions of Schrödinger equation is an interesting problem in fundamental quantum mechanics for lecturers, advanced undergraduate and graduate students in physics and applied mathematics. Since there are not many potentials which admit exact solutions, then one needs to use approximate solutions such as WKB. In the framework of supersymmetric quantum mechanics, one can construct a hierarchy of Hamiltonians by using *raising* and *lowering* operators to obtain the energy spectra of the quantum system [1]. However, for some type of potentials one may need further treatment in the solution, such as supersymmetric WKB for unbroken symmetry or broken supersymmetric WKB for broken symmetry. Unfortunately, they failed to give exact results in good agreement for the broken/unbroken supersymmetry. The bound-state spectra for some potentials with unbroken and broken supersymmetry are investigated by the quantization condition of a recent method, called Asymptotic Iteration Method (AIM). AIM [2] is proposed and applied to solve the second-order differential equations in the form

$$f''(x) = \lambda_0(x)f'(x) + s_0(x)f(x) \quad (4)$$

where $\lambda_0(x)$ and $s_0(x)$ are arbitrary functions in $C_\infty(a,b)$ and $\lambda_0(x) \neq 0$. Using AIM, one obtains the general solution as [2]:

$$f(x) = \exp\left(-\int^x \alpha(x_1)dx_1\right) [C_2 + C_1 \int^x \exp\left(\int^{x_1} (\lambda_0(x_2) + 2\alpha(x_2))dx_2\right) dx_1]. \quad (5)$$

where, for sufficiently large $n > 0$, one gets

$$\frac{s_k(x)}{\lambda_k(x)} = \frac{s_{k-1}(x)}{\lambda_{k-1}(x)} = \alpha(x) \quad (6)$$

for

$$\begin{aligned} \lambda_k(x) &= \lambda'_{k-1}(x) + s_{k-1}(x) + \lambda_0(x)\lambda_{k-1}(x) \\ s_k(x) &= s'_{k-1}(x) + s_0(x)\lambda_{k-1}(x), \end{aligned} \quad (7)$$

which are called the recurrence relation of Eq.(4). The energy eigenvalues are then obtained from the roots of the termination condition (6), which can be written in more convenient form as

$$\begin{aligned} \delta_k(x) &= \lambda_k(x)s_{k-1}(x) - \lambda_{k-1}(x)s_k(x) = 0, \\ k &= 1, 2, 3, \dots \end{aligned} \quad (8)$$

Using AIM, we analyze the one-dimensional anharmonic oscillator partner potentials that are non shape-invariant potentials with unbroken supersymmetry [3], the unsolvable polynomial partner potentials with unbroken supersymmetry [4] and the non-shape-invariant spherically symmetric partner potentials with broken supersymmetry [5]. Energy eigenvalues are obtained by AIM are found to be in excellent agreement with numerical values and it is also noted that the AIM condition preserves the supersymmetric energy degeneracy [6].

^{a)} University of Gaziantep, Gaziantep, Turkey

[1] G. Lévai, J. Phys. A 22 (1989) 689.

[2] O. Özer, P. Roy, Cent. Eur. J. Phys. 7 (2009) 747.

[3] R. Adhikari, R. Dutt, A. Khare, U. P. Sukhatme, Phys. Rev. A 38 (1988) 1679.

[4] Y. P. Varshni, J. Phys. A 25 (1992) 5761.

[5] R. Dutt, A. Gangopadhyaya, A. Khare, A. Pagnamenta, U. Sukhatme, Phys. Rev. A 48 (1993) 1845.

[6] O. Özer, G. Lévai, in preparation.

2.1 Stellar and Primordial Nucleosynthesis of ${}^7\text{Be}$: measurement of ${}^3\text{He}(\alpha, \gamma){}^7\text{Be}$

A. Di Leva^{a,b}, L. Gianlanella^a, R. Kunz^b, D. Rogalla^b, D. Schürmann^b, F. Strieder^b, M. De Cesare^a, N. De Cesare^a, A. D'Onofrio^a, Zs. Fülöp, Gy. Gyürky, G. Imbriani^a, G. Mangano^a, A. Ordine^a, V. Roca^a, C. Rolfs^b, M. Romano^c, E. Somorjai and F. Terrasi^a

The precise knowledge of the different neutrino fluxes can be used to understand physical and chemical properties of the Sun, provided that nuclear reaction cross sections are known with adequate accuracy. In the case of the cross section $\sigma(E)$ of ${}^3\text{He}(\alpha, \gamma){}^7\text{Be}$, which determines the flux of the recently detected ${}^7\text{Be}$ neutrinos, a precision of at least 3% should be achieved.

The ${}^3\text{He}(\alpha, \gamma){}^7\text{Be}$ reaction also has important implications on the Big Bang nucleosynthesis (BBN). The predicted abundance of ${}^7\text{Li}$ [${}^7\text{Be}(e^-, \nu){}^7\text{Li}$] from the cosmological models is larger than observational one. Therefore, an accurate evaluation of $\sigma(E)$ is the necessary basis for possible solutions of the ${}^7\text{Li}$ problem.

During the last four decades, a lot of experiments were performed exploiting either the detection of the prompt γ -rays or the off-beam determination of the ${}^7\text{Be}$ atoms.

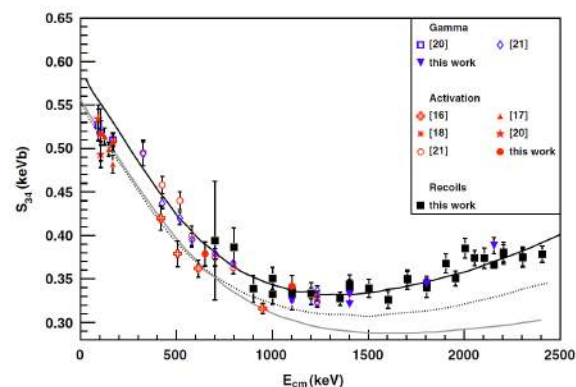


Figure 1. Comparison of the present results and recent works (ref.'s see in [1]) with different model calculations fitted at $E_0 \leq 2000$ keV.

These experiments covered the BBN energy range ($E_{cm} \approx 180-400$ keV), while the Gamow energy in the Sun ($E_0 = 22$ keV) was not reached and models have to be used to extrapolate the data. The results show an overall fair agreement in the energy dependence of $\sigma(E)$, while they disagree in their absolute values.

In this work (details in [1]) $\sigma(E)$ was determined by the direct detection of the ${}^7\text{Be}$ re-

coils from He gas target using the recoil separator ERNA (Ruhr University Bochum). In the energy range of the experiment, the recoil yield for each significant charge state q of ${}^7\text{Be}$ was measured in separate runs. Concurrently, the capture γ -rays were detected in coincidence with the recoils at selected energies. In addition, measurements were performed to obtain cross section values independent of the recoil separator, namely, by installing (downstream) a circular copper catcher close to the gas target to collect the produced ${}^7\text{Be}$ nuclei. The $\sigma(E)$ from the activity of the ${}^7\text{Be}$ nuclei was determined on the same way as in [2] at LNGS, Italy.

In conclusion, our data in combination with the measurements of [3] give an estimate of $S_{34}(0) = 0.590 \pm 0.016$ keV \cdot b using a direct capture model, but with other data an $S_{34}(0) = 0.553 \pm 0.012$ keV \cdot b value cannot be ruled out (see Fig.1). Until new information is available, a conservative estimate of $S_{34}(0) = 0.57 \pm 0.04$ keV \cdot b is suggested. This estimate represents an improvement, but it is still far from the precision required by solar models. However, at energies above 1 MeV a large discrepancy compared to previous results (not shown in Fig. 1.) is observed both in the absolute value and in the energy dependence of the cross section. With our conservative $S_{34}(0) = 0.57 \pm 0.04$ keV \cdot b value, the theoretical primordial ${}^7\text{Li}$ abundance is larger than the observational value by a factor 3 or more, thus worsening the primordial ${}^7\text{Li}$ problem.

a) INFN, Sezione di Napoli, Naples, Italy

b) Ruhr-Universität Bochum, Bochum, Germany

c) Università Federico II, Naples, Italy

[1] A. Di Leva et al., Phys. Rev. Letters **102**, 232502 (2009).

[2] G. Gyürky et al., Phys. Rev. **C75**, 035805 (2007).

[3] T.A.D. Brown et al., Phys. Rev. **C76**, 055801 (2007).

2.2 Persistent decoupling of valence neutrons toward the dripline: study of ^{20}C by γ spectroscopy

Z. Elekes, Zs. Dombrádi, T. Aiba^{a)}, N. Aoi^{b)}, H. Baba^{b)}, D. Bemmerer^{c)}, B.A. Brown^{d)}, T. Furumoto^{e)}, Zs. Fülöp, N. Iwasa^{f)}, Á. Kiss^{g)}, T. Kobayashi^{f)}, Y. Kondo^{h)}, T. Motobayashi^{b)}, T. Nakabayashi^{h)}, T. Nannichi^{h)}, Y. Sakuragi^{e)}, H. Sakurai^{b)}, D. Sohler, M. Takashinaⁱ⁾, S. Takeuchi^{b)}, K. Tanaka^{b)}, Y. Togano^{b)}, K. Yamada^{b)}, M. Yamaguchi^{b)}, K. Yoneda^{b)}

A few years ago, the decoupling of strongly-bound neutrons in heavy carbon and boron isotopes was reported [1,2,3,4], which was observed as a reduction of the quadrupole polarization charge of the neutrons. This suppression of the polarization charge was associated with the extended distribution of the valence neutrons [5,6,7] detected in reaction cross section measurements [8]. This might also be accompanied with the change of the structure of the giant quadrupole resonance in neutron rich nuclei [5,6,9]. Recently, the lifetime of the 2_1^+ state in ^{16}C has been re-measured, and the decoupling phenomenon has been questioned [10]. However, another novel work suggests the existence of this decoupling effect [11]. We report here on a study of the neutron and proton transition strengths and polarization charges investigated by inelastic scattering processes in the heavy carbon isotope ^{20}C , lying next to ^{19}C which shows halo characteristics in its ground state. Our aim is to provide further evidence that the decoupling phenomenon exists in the carbon isotopic chain. The experiment detailed in Ref. [13] was carried out at RIKEN Nishina Center. From the experimental γ ray spectra, we determined the cross sections at $\sigma^{Pb}(0_{gs}^+ \rightarrow 2_1^+) = 35 \pm 8$ mb and $\sigma^{pp}(0_{gs}^+ \rightarrow 2_1^+) = 24 \pm 4$ mb for the Pb and the liquid hydrogen target runs, respectively. The results were analyzed in the framework of the coupled channels code ECIS97 which uses standard collective form factors to calculate the inelastic cross sections. In this way, the neutron and proton deformation lengths were extracted at $\delta_n = 1.57 \pm 0.14$ (stat) fm, $\delta_p = 0.60 \pm 0.32$ (stat) fm. The corresponding multipole proton and neutron transition matrix elements (M_p^2, M_n^2) could then be calculated as $M_p^2 = 7.8_{-6.1}^{+10.6}$ (stat) fm⁴ and $M_n^2 = 292 \pm 52$ (stat) fm⁴, respectively. The validity of the phenomenological approach

was further examined by microscopic coupled-channels (MCC) calculations using folding model interactions with AMD transition density [12] and found good agreement with the phenomenological analysis. In order to analyze the effective charges, the transition probabilities were calculated within the shell model. A factor of about 0.4 reduction of the normal polarization charges was needed to reproduce the experimental trend in carbon isotopes. The fact that the polarization charges have decreased to less than half of the standard values indicates that the coupling of the valence neutrons to the core has become weaker, or in other terms, the valence neutrons decoupled to some extent from the nuclear core. A possible reason for these decreased polarization charges might be the extended valence neutron distribution.

a)Niigata University, Japan

b)RIKEN, Japan

c)Forschungszentrum Dresden-Rossendorf, Germany

d)Michigan State University, USA

e)Osaka City University, Japan

f)Tohoku University, Japan

g)Eötvös Loránd University, Hungary

h)Tokyo Institute of Technology, Japan

i)RCNP, Osaka University, Japan

[1] H. Ogawa *et al.*, PRC 67 (2003) 064308.

[2] Zs. Dombrádi *et al.*, PLB 621 (2005) 81.

[3] N. Imai *et al.*, PRL 92 (2004) 062501.

[4] Z. Elekes *et al.*, PLB 586 (2004) 34.

[5] H. Sagawa *et al.*, PRC 63 (2001) 064310.

[6] H. Sagawa *et al.*, EPJA 13 (2002) 87.

[7] Y. Suzuki *et al.*, PRC 70 (2004) 051302.

[8] A. Ozawa *et al.*, NPA 691 (2001) 599.

[9] H. Sagawa *et al.*, PRC 65 (2002) 064314.

[10] M. Wiedeking *et al.*, PRL 100 (2008) 152501.

[11] H.J. Ong *et al.*, PRC 78 (2008) 014308.

[12] Y. Kanada-En'yo *et al.*, PRC 71 (2005) 014310.

[13] Z. Elekes *et al.*, PRC 79 (2009) 011302(R).

2.3 Study of the neutron-rich ^{21}N nucleus through proton inelastic scattering

Zs. Vajta, Z. Elekes, T. Aiba^{a)}, N. Aoi^{b)}, H. Baba^{b)}, D. Bemmerer^{c)}, Zs. Dombrádi, T. Furumoto^{d)}, Zs. Fülöp, N. Iwasa^{e)}, Á. Kiss^{f)}, T. Kobayashi^{e)}, Y. Kondo^{g)}, T. Motobayashi^{b)}, T. Nakabayashi^{g)}, T. Nannichi^{g)}, Y. Sakuragi^{d)}, H. Sakurai^{b)}, D. Sohler, M. Takashina^{h)}, S. Takeuchi^{b)}, K. Tanaka^{b)}, Y. Togano^{b)}, K. Yamada^{b)}, M. Yamaguchi^{b)}, K. Yoneda^{b)}

Recently, the existence of a new subshell closure at $N=14$ was discovered in the ^{22}O isotope, which disappears already in ^{20}C having two protons less. In order to explore the characteristics of this transition we studied the structure of the middle-lying nitrogen isotope $^{21}\text{N}_{14}$ via (p,p') inelastic scattering process in inverse kinematics.

The experiment was carried out at RIKEN Nishina Center, where a ^{40}Ar primary beam of 63 MeV energy and 700 pA intensity was delivered to a ^{181}Ta production target. The RIKEN isotope separator (RIPS), which analyzed the momentum and mass of the ejectiles, was optimized for the transmission of ^{20}C . The resultant cocktail beam included ^{17}B , ^{19}C , ^{21}N , and ^{22}N isotopes with a total intensity of 100 pps. The identification of these incident beam constituents was performed on an event-by-event basis using energy loss (ΔE), time-of-flight (TOF), and magnetic rigidity ($B\rho$) information. The radioactive beams produced were transmitted to the secondary liquid hydrogen target with a thicknesses of 190 mg/cm². The scattered particles were detected and identified by the ΔE -TOF-E method. Altogether 6.8×10^5 ^{21}N were observed during the experiment.

A stack of 160 NaI(Tl) crystals called DALI2 surrounded the secondary target to detect the deexcitation γ rays emitted by the inelastically scattered nuclei. The resulting Doppler-corrected γ -ray spectra for ^{21}N can be seen in Figures 1 and 2 for γ -multiplicity $M\gamma=1$ and 2, respectively. In the obtained spectra a double peak was observed close to 1200 keV, which could be resolved for two γ rays at 1140 and 1210 keV. These peaks correspond to the transitions between the two first excited and the ground states of ^{21}N . Their energies are in good agreement with the

previously determined values of 1159(29) and 1228(29) keV.

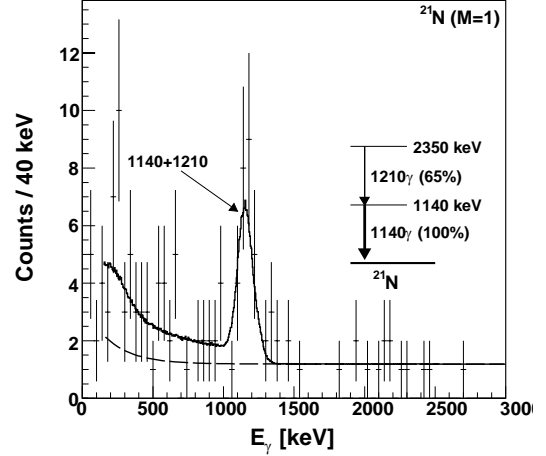


Figure 1. Doppler-corrected gamma-ray spectrum of ^{21}N for $M\gamma=1$ multiplicity.

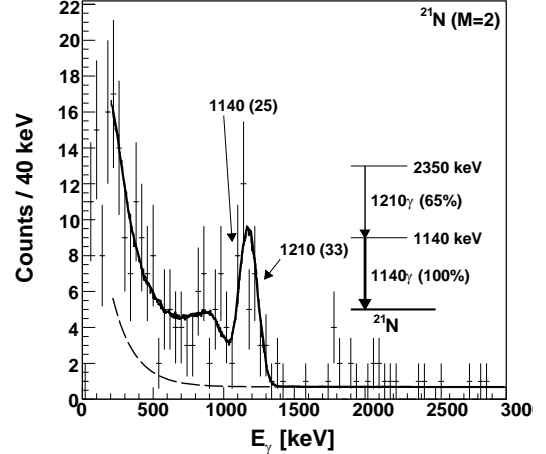


Figure 2. Doppler-corrected gamma-ray spectrum of ^{21}N for $M\gamma=2$ multiplicity.

- a) Niigata University, Japan
- b) RIKEN, Japan
- c) Forschungszentrum Dresden-Rossendorf, Germany
- d) Osaka City University, Japan
- e) Tohoku University, Japan
- f) Eötvös Loránd University, Hungary
- g) Tokyo Institute of Technology, Japan
- h) RCNP, Osaka University, Japan

2.4 Hyperdeformed band in the ^{36}Ar nucleus?

J. Cseh, J. Darai^{a)}, W. Scian^{b)}, Y. Otani^{c)}, A. Lepine-Szily^{c)}, E.A. Benjamin^{d)}, L.C. Chamon^{c)}, R.L. Filho^{c)}

The exotic shapes of atomic nuclei has attracted much attention recently both from the experimental and from the theoretical sides. E.g. the superdeformed (SD) shape in $N = Z$ nuclei were observed experimentally during the last decade. In particular the SD band of the ^{36}Ar nucleus was detected in 2000 [1]. Following the experimental observation a considerable theoretical effort has been concentrated on this band. In [2] e.g. the possible binary clusterizations of this state was studied systematically. Similar studies have been done also for the ground, and the hyperdeformed band. The latter one had been predicted from alpha-cluster model calculations [3]. The possible binary cluster-configurations are important not only for the better understanding of the structure of the shape isomers, but also from the viewpoint of predicting the favoured reaction channels to populate these states. This is the straightforward consequence of the close relation between the clusterization and reaction channels. (In fact, a cluster-configuration is defined by the reaction channel in which it can be observed.) One of the interesting conclusions of the work [2] was, that the hyperdeformed (HD) state of the ^{36}Ar nucleus could be populated in the $^{24}\text{Mg}+^{12}\text{C}$ and $^{20}\text{Ne}+^{16}\text{O}$ reactions.

A recent analysis of the $^{24}\text{Mg}+^{12}\text{C}$ elastic scattering [4] revealed the fact that the cross section can be described only by supposing resonances on top of the potential scattering. This very careful analysis incorporated phase-shift study, as well as Regge-pole and energy-dependent resonance calculations. The existence of five resonances have been proved, which have angular momenta 2, 4, 6, 7, 8. These states together with the resonances from the $^{20}\text{Ne}+^{16}\text{O}$ reactions seem to establish a rotational band, as shown in the upper part of Fig. 1. Its moment of inertia is in a very good agreement with that of the HD shape predicted from alpha-cluster model [3]. The similarity of the (predicted and observed) moments of in-

ertia, and the fact that the resonances were seen in exactly those reactions, which define the preferred cluster-configurations of the HD shape suggest that the recently observed band in Fig. 1. is a good candidate for the hyperdeformed shape isomer of the ^{36}Ar nucleus. For comparison also the ground and superdeformed bands are indicated in Fig. 1.

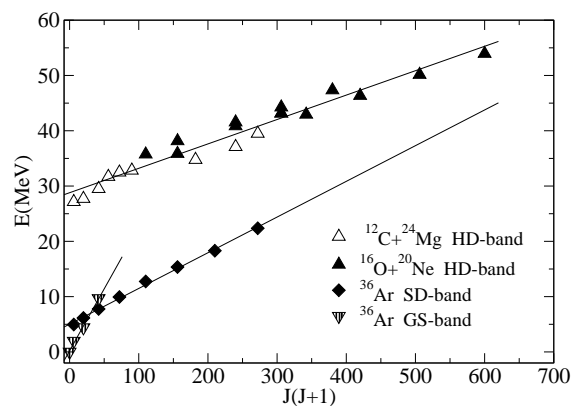


Figure 1. Excited states in ^{36}Ar , observed as resonances in the $^{12}\text{C}+^{24}\text{Mg}$ and $^{16}\text{O}+^{20}\text{Ne}$ reactions. The SD band observed in ^{36}Ar and the ground-state band are also included.

Since a candidate for the HD state showed up, the exciting question arises if such a shape can be seen in shell-model calculation as well. In [5] we have carried out Nilsson-model+quasi-dynamical SU(3) calculation in order to find the answer. In this kind of study the shape isomers are obtained from the SU(3) symmetries, not from the minima of the potential energy surface. They are determined as the horizontal plateaus of the stair-like functions, shown in Fig. 2. (In lighter nuclei, where detailed comparison could be made, the two method gave results in very good agreement with each other.) As it is seen in Fig. 2. in addition to the ground and superdeformed states the shell model predicts two candidates (a slightly triaxial, and a cylindrical one) for the hyperdeformed shape. The cylindrical state has exactly the same symmetry as

that from the alpha-cluster model, and consequently the same moment of inertia, as well.

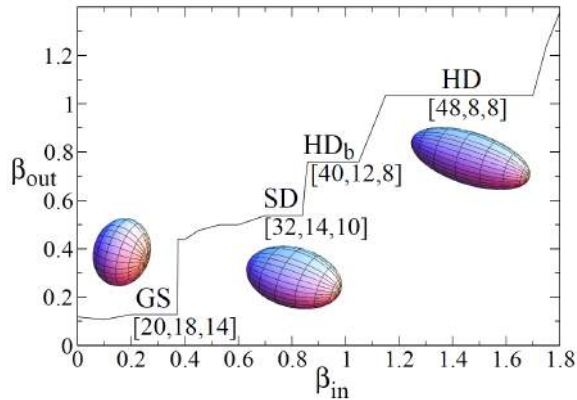


Figure 2. Quadrupole deformation of the ^{36}Ar nucleus from the Nilsson-model with the effective $U(3)$ quantum numbers at the plateaus. The approximate shape of the ground, superdeformed and hyperdeformed states are indicated by the inserts.

To sum up: from cluster studies [2,3] we have predicted [2] the $^{24}\text{Mg}+^{12}\text{C}$ and $^{20}\text{Ne}+^{16}\text{O}$ channels to populate the HD state in

the ^{36}Ar nucleus. Recently a highly-deformed rotational band has been observed [4] experimentally in these reactions. The moment of inertia is in complete agreement with the prediction. Furthermore, the same state has been found in Nilsson-model calculation [5]. Therefore, we conclude that it is a good candidate for the hyperdeformed band in the ^{36}Ar nucleus, as shown in Fig. 1. Thus it might very well be that the ^{36}Ar nucleus is the first $N = Z$ nucleus in which the ground, superdeformed and hyperdeformed bands have been observed.

- [1] C.E. Svensson et al, Phys. Rev. Lett. **85** (2000) 2693.
- [2] J. Cseh et al, Phys. Rev. **C70** (2004) 034311.
- [3] W.D.M. Rae, A.C. Merchant, Phys. Lett. **B279** (1992) 207.
- [4] W. Sciani et al, Phys. Rev. **C80** (2009) 034319.
- [5] J. Cseh et al, Phys. Rev. **C80** (2009) 034320.

- a) University of Debrecen, Debrecen, Hungary
- b) Universidade Presbiteriana Mackenzie, Brazil
- c) Universidade de Sao Paulo, Sao Paulo, Brazil
- d) Universidade de Santiago de Compostela, Spain

2.5 In-beam γ -ray spectroscopy of the neutron rich ^{39}Si

D. Sohler, S. Grévy^{a)}, Zs. Dombrádi, O. Sorlin^{a)}, N.L. Achouri^{b)}, J.C. Angélique^{b)}, F. Azaiez^{c)}, D. Baiborodin^{d)}, B. Bastin^{b)}, R. Borcea^{e)}, C. Bourgeois^{c)}, A. Buta^{e)}, A. Burger^{f,g)}, R. Chapman^{h)}, J.C. Dalouzy^{a)}, Z. Dlouhy^{d)}, A. Drouard^{f)}, Z. Elekes, S. Franchoo^{c)}, S. Iacob^{e)}, B. Laurent^{b)}, M. Lazar^{e)}, X. Liang^{h)}, E. Lienard^{b)}, S.M. Lukyanovⁱ⁾, J. Mrazek^{d)}, L. Nalpas^{f)}, F. Negoita^{e)}, F. Nowacki^{j)}, N.A. Orr^{b)}, Y. Penionskhevitchⁱ⁾, Zs. Podolyak^{k)}, F. Pougheon^{c)}, P. Roussel-Chomaz^{a)}, M. Stanoiu^{c,l)}, I. Stefan^{a)}, M.G. St-Laurent^{a)}

In order to clarify the role of proton excitations across the $Z = 14$ subshell closure in neutron-rich Si isotopes, we investigated the structure of the $^{39}\text{Si}_{25}$ isotope, having three neutron-hole configurations with respect to an $N = 28$ core. The excited states of ^{39}Si were studied by in-beam γ -ray spectroscopy through fragmentation of radioactive beams.

The experiment was performed at the GANIL facility in France. The radioactive beams were produced by the fragmentation of the stable ^{48}Ca beam of 60 MeV/u energy and 4 μA intensity on a ^{12}C target in the SISSI device. The cocktail beam produced was impinged onto a ^9Be target. The nuclei produced in the secondary fragmentation reaction were selected and unambiguously identified by the SPEG spectrometer. In the performed experiment the ^{39}Si nuclei were obtained via $1p$, $1p1n$, $2p1n$ and $2p2n$ knockout reactions from the $^{40,41}\text{P}$ and $^{42,43}\text{S}$ secondary beams.

To measure the γ rays emitted from the excited states, the secondary target was surrounded by the 4π 'Chateau de Crystal' array consisting of 74 BaF_2 scintillators. The γ -ray spectra were generated by gating event-by-event on the incoming secondary beam particles and the ejectiles after the secondary target. For the γ rays emitted by the fast moving fragments accurate Doppler correction was performed. From the obtained γ spectra of ^{39}Si displayed in Figure 1, two strong γ transitions at 163 and 397 keV as well as weaker ones at 303, 657, 906, 1143 and 1551 keV have been identified. $\gamma\gamma$ coincidences were obtained in ^{39}Si after having added all data from the various reaction channels giving rise to ^{39}Si . Analysing these data the 163 keV transition was found to be in coincidence with the 657, 1143 and 1551 keV ones, but not with

the 397 keV transition. The two lines of the 303+397 keV doublet are in mutual coincidence, and one or both of them are found in coincidence with the 906 keV transition.

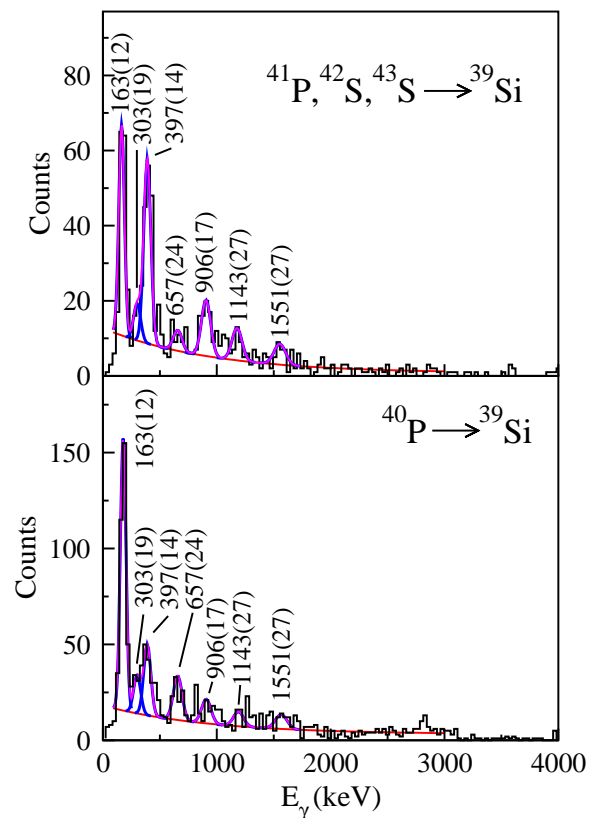


Figure 1. Gamma-ray energy spectrum detected in coincidence with ^{39}Si nuclei.

- a) GANIL, Caen, France
- b) LPC, Caen, France
- c) IN2P3-CNRS, Orsay, France
- d) NPI, Rez, Czech Republic
- e) IFIN-HH, Bucharest-Magulere, Romania
- f) DAPNIA/SPhN, CEA Saclay, France
- g) Universität Bonn, Germany
- h) University of Paisley, Scotland, UK
- i) FLNR, JINR, Dubna, Russia
- j) IreS, Strasbourg, France
- k) University of Surrey, Guildford, UK
- l) GSI, Darmstadt, Germany

2.6 High resolution study of the Gamow-Teller strength distribution in Sc isotopes

L. Stuhl, *T. Adachi*^{a)}, *A. Algora*^{b)}, *M. Csatlós*, *J. Deaven*^{c)}, *E. Estevez*^{b)}, *H. Fujita*^{a)}, *Y. Fujita*^{a)}, *C. Guess*^{c)}, *J. Gulyás*, *K. Hatanaka*^{a)}, *K. Hirota*^{a)}, *O. Hooi Jim*^{c)}, *D. Ishikawa*^{a)}, *A. Krasznahorkay*, *H. Matsubara*^{a)}, *R. Meharchand*^{c)}, *F. Molina*^{b)}, *H. Okamura*^{a)}, *G. Perdikakis*^{c)}, *B. Rubio*^{b)}, *C. Scholl*^{c)}, *T. Suzuki*^{a)}, *G. Sűsoy*^{c)}, *A. Tamii*^{a)}, *J. Thies*^{a)}, *R. Zegers*^{c)}, *J. Zenihoro*^{a)}

The Gamow-Teller (GT) strength distributions are sensitive to changes in shell structure and thus provide a way of studying such changes along an isotopic chain.

Experimental GT strength distributions are not included when performing fits on parameters of shell-model interactions. These interactions are based on level excitation energies. Since the extraction of GT strengths from charge exchange (CE) data is nearly model-independent, a detailed and unbiased testing of shell-model interactions is possible.

In order to check the shell structure of Sc isotopes, and to discuss the spin-isospin interaction in pf-shell region, high resolution experiment was performed with the (³He,t) reaction on Ca isotopes. The experiment was carried out at the Research Center for Nuclear Physics (RCNP), Osaka University. The energy of the ³He beam of 400 MeV was achromatically transported to the ⁴⁰Ca, ⁴²Ca, ⁴⁴Ca and ⁴⁸Ca targets with thicknesses of 1.63 - 1.87 mg/cm² and isotopic enrichments of 99.97 %, 93.71 %, 98.78 %, and 95.2 %, respectively. The typical beam intensity was 5 enA.

The energy of tritons was measured with the magnetic spectrometer “Grand Raiden” [1] using complete dispersion matching techniques [2]. The energy resolution obtained was about 20 keV. The spectrometer was set at 0° and 2.5° with an opening angle of ±20 mrad horizontally and ±20 mrad vertically defined by a slit at the entrance of the spectrometer. Spectra for scattering angles between 0° and 3.5° were generated by ray-tracing techniques [3] and the spectra were decomposed into resonances and nonresonant components. The J^π of the transitions were determined by comparing the an-

gular distributions to the DWBA predictions. In this way we determined 101 new 1⁺, 23 new 3⁺ and 48 new L≥1 levels. The obtained GT strength distribution for ⁴⁸Sc was normalized in a similar way as published in Ref. [4] and shown in Fig. 1.

The corresponding theoretical analysis of the strengths is in progress.

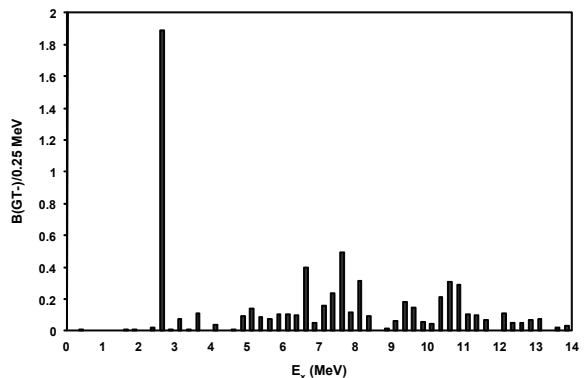


Figure 1. GT strength distribution of ⁴⁸Sc as a function of the excitation energy.

Acknowledgements

The work has been supported by the Hungarian OTKA Foundation No. K 72566.

- a)RCNP, Osaka University, Ibaraki, Osaka 567-0047, Japan
 - b) IFIC (CSIC-Univ. Valencia), Valencia, Spain
 - c) NSCL, Michigan State University, East Lansing, Michigan 48824, USA
- [1] M. Fujiwara et al., Nucl. Instrum. Methods Phys. Res. A 422, 484 (1999).
 - [2] T. Wakasa et al., Nucl. Instrum. Methods Phys. Res. A 482, 79 (2002).
 - [3] Y. Fujita et al., Nucl. Instrum. Methods Phys. Res. B 126, 274 (1997); H. Fujita et al., Nucl. Instrum. Methods Phys. Res. B 484, 17 (2002).
 - [4] E.-W. Grewe et al., Phys. Rev. C76 (2007) 054307.

2.7 High precision $^{89}\text{Y}(\alpha, \alpha)^{89}\text{Y}$ scattering at low energies

G.G. Kiss, P. Mohr^{a)}, Zs. Fülöp, D. Galaviz^{b)}, Gy. Gyürky, Z. Elekes, E. Somorjai A. Kretschmer^{c)}, K. Sonnabend^{c)}, A. Zilges^{d)}, M. Avrigeanu^{e)}

Alpha-nucleus potentials are basic ingredients for the calculation of reaction cross sections with α particles in the entrance or exit channel. These reaction cross sections are included in stellar reaction rate calculations in nuclear astrophysics. The extensive use of the statistical model requires experimental tests for the global alpha-nucleus optical potential parameterizations.

In previous years several (α, α) reactions on even-even nuclei have been studied at ATOMKI [1, and references therein]. In this work we measured the angular distribution of the $^{89}\text{Y}(\alpha, \alpha)^{89}\text{Y}$ reaction at $E_{c.m.} = 15.51$ MeV and 18.63 MeV with small uncertainties over the whole 20-170° angular range. The measured data are compared to calculations performed with global and regional alpha nucleus optical potentials. In some cases reasonable agreement was found [1]. Furthermore, a global alpha-nucleus optical potential must be able not only to provide a correct prediction for the elastic scattering cross section but also to describe the α -induced reaction cross sections, and to describe the variation of the angular distributions along isotopic and isotonic chains. The latest is especially important since modeling explosive nucleosynthesis scenarios requires the rate of a large number of reactions involving thousands of stable and mostly unstable nuclei where the potential cannot be derived from experimental scattering data.

In this work we used the ratio of the Rutherford normalized cross sections of $^{89}\text{Y}(\alpha, \alpha)^{89}\text{Y}$ from this work and $^{92}\text{Mo}(\alpha, \alpha)^{92}\text{Mo}$ previously studied by Fülöp et al., [2] at $E_{c.m.} = 15.69$ and 18.62 MeV to test the global and regional parameterizations used in astrophysical calculations. We found that all global parameterizations failed to reproduce the amplitude and/or phase of the oscillations of the ratio of the Rutherford normalized cross sections as can be seen in Fig. 1. In order to advance our current un-

derstanding of the α -nucleus optical potential, further experimental data is essential as well as improvements on the theory side.

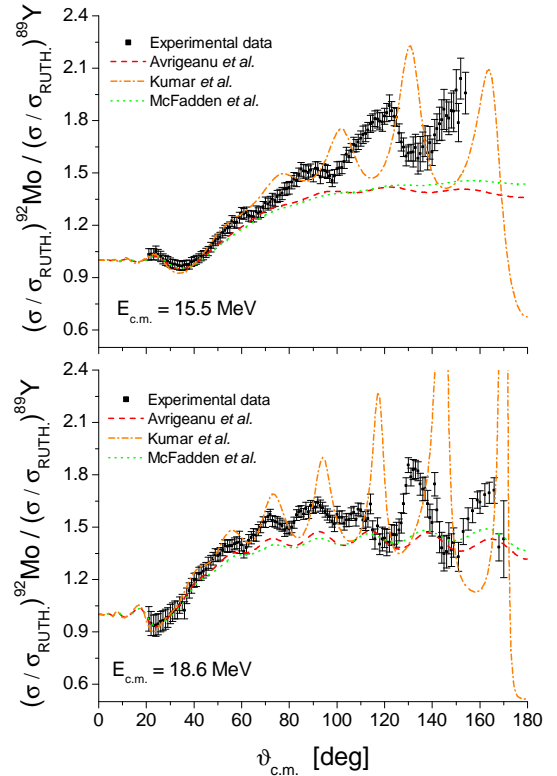


Figure 1. Ratio of the Rutherford normalized elastic scattering cross sections of $^{89}\text{Y}(\alpha, \alpha)^{89}\text{Y}$ and $^{92}\text{Mo}(\alpha, \alpha)^{92}\text{Mo}$ reactions at $E_{c.m.} = 15.69$ and 18.63 MeV versus the scattering angle. The lines correspond to the predictions using different global optical potential parameter sets.

- a) Diakonie-Klinikum, Schwäbisch Hall, Germany,
- b) Instituto de Estructura de la Materia, CSIC, Madrid, Spain,
- c) Institut für Kernphysik, TUD, Darmstadt, Germany,
- d) Institut für Kernphysik, Universität zu Köln, Köln, Germany,
- e) Horia Hulubei National Institute for Physics and Nuclear Engineering, Bucharest, Romania

[1] G.G. Kiss *et al.*, *Phy. Rev. C* **80**, 045807 (2009).

[2] Fülöp *et al.*, *Phy. Rev. C* **64**, 065805 (2001).

2.8 Structure of high-spin bands in ^{104}Pd

D. Sohler, J. Timár, I. Kuti, J. Molnár, A. Algora, Zs. Dombrádi, J. Gál, A. Krasznahorkay, L. Zolnai, P. Joshi^{a)}, K. Starosta^{b)}, D.B. Fossan^{c)}, R. Wadsworth^{a)}, P. Bednarczyk^{d)}, D. Curien^{e)}, G. Duchene^{e)}, A. Gizon^{f)}, J. Gizon^{f)}, D.G. Jenkins^{a)}, T. Koike^{g)}, E.S. Paul^{h)}, P.M. Raddon^{a)}, G. Rainovskiⁱ⁾, J.N. Scheurer^{j)}, A.J. Simons^{a)}, C. Vaman^{b)}, A.R. Wilkinson^{a)}

High-spin states of ^{104}Pd were studied through the $^{96}\text{Zr}(^{13}\text{C},5n)$ reaction at beam energies of 51 and 58 MeV, using the EUROBALL IV γ -ray spectrometer in conjunction with the DIAMANT charged particle array. On the basis of the analysis of $\gamma\gamma\gamma$ -coincidence data, the previously known rotation-like structures (*bands 1,2,3,4*) have been extended up to $E_x \sim 6, 13, 11$ and 9 MeV with $I^\pi = (12^+), (26^+), (23^-)$ and (20^-) , respectively. Besides the major sideband structures, two new negative-parity cascades (*bands 5,6*) were found and built up to $E_x \sim 8$ MeV with $I^\pi = (17^-)$ and (18^-) .

The ^{104}Pd nucleus with its 6 valence protons and 8 valence neutrons relative to ^{90}Zr lies in the upper part of the $g_{9/2}$ proton subshell and in the middle part of the $d_{5/2}, g_{7/2}$ neutron subshell where the low- Ω $h_{11/2}$ orbitals intrude already at small deformations. To get a deeper insight into the structure of the observed bands, total routhian surface (TRS) calculations based on the Woods-Saxon cranking formalism were performed. Comparing the experimental Routhians E' and aligned angular momenta I_x with the TRS results (Fig. 1), we assign two-quasiparticle $\nu(h_{11/2})^2$ configuration to the positive-parity *bands 1* and *2*. According to this expectation, the alignment of a $h_{11/2}$ neutron pair is clearly visible at $\hbar\omega \approx 0.4$ MeV frequency with nearly the full possible alignment gain of $\sim 10\hbar$.

As in the negative-parity *bands 3,4,5* and *6* the $\nu h_{11/2}$ alignment seems to be blocked, their configuration contains one neutron in the $h_{11/2}$ orbit. Furthermore, the second quasineutron is expected to have a $g_{7/2}, d_{5/2}$ origin due to their parity. This assumption is supported by the good agreement of the experimental data with the TRS results and accordingly we suggest $\nu h_{11/2}(d_{5/2}, g_{7/2})$ configurations for these bands.

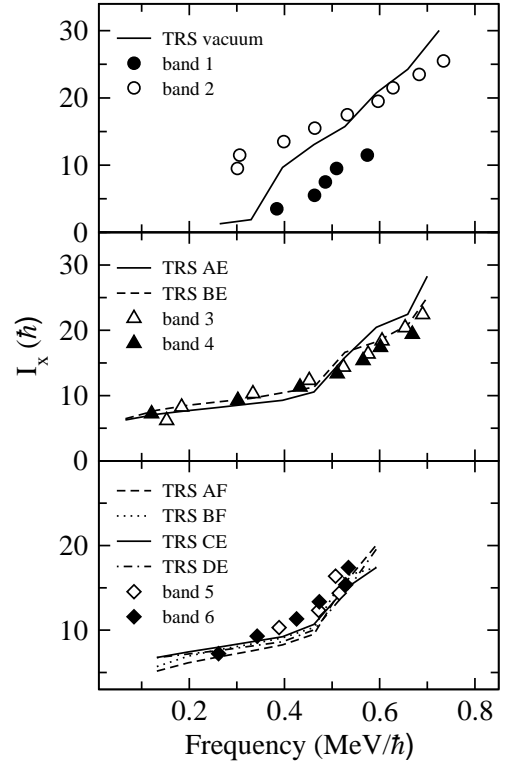


Figure 1. Comparison of the experimental and TRS aligned angular momenta I_x for high-spin bands in ^{104}Pd .

- a) Department of Physics, University of York, York, YO10 5DD, UK
- b) NSCL, Cyclotron Laboratory, Michigan State University, East Lansing, MI 48824-1321, USA
- c) Department of Physics and Astronomy, SUNY, Stony Brook, New York, 11794-3800, USA
- d) GSI, Darmstadt, Germany
- e) IReS, 23 rue du Loess, Strasbourg, 67037, France
- f) LPSC, IN2P3-CNRS/UJF, F-38026 Grenoble-Cedex, France
- g) Department of Physics, Tohoku University, Sendai, Japan
- h) Oliver Lodge Laboratory, Department of Physics, University of Liverpool, Liverpool L69 7ZE, UK
- i) Faculty of Physics, St. Kliment Ohridski University of Sofia, BG-1164 Sofia, Bulgaria
- j) Université Bordeaux 1, IN2P3- CENBG - Le Haut-Vigneau BP120 33175, Gradignan Cedex, France

2.9 Gamma-ray multipolarity assignments in ^{132}La

I. Kuti, J. Timár, D. Sohler, B.M. Nyakó, L. Zolnai, Zs. Dombrádi, E.S. Paul^{a)}, A.J. Boston^{a)}, H.C. Chantler^{a)}, C. Fox^{a)}, P.J. Nolan^{a)}, J.A. Sampson^{a)}, H.C. Scraggs^{a)}, A. Walker^{a)}, J. Gizon^{b)}, A. Gizon^{b)}, D. Bazzacco^{c)}, S. Lunardi^{c)}, C.M. Petrache^{c,d)}, A. Astier^{e)}, N. Buford^{e)}, P. Bednarczyk^{f)}, N. Kintz^{f)}, K. Starosta^{g)}, D.B. Fossan^{h)}, T. Koike^{h)}, C.J. Chiaraⁱ⁾, R. Wadsworth^{j)}, A.A. Hecht^{k)}

Understanding the nature of the chiral-candidate strongly linked $\Delta I=1$ rotational band structures, where results of lifetime experiments rule out chiral explanation is a challenge for the present high-spin nuclear structure studies. The observed three linked $\Delta I=1$ bands in ^{132}La is one of these cases. Recently SPAC calculations seemed to describe successfully the properties of these bands [1]. However, the experimental spins and parities of one of these bands, that were used in the comparison with the SPAC results, are only tentatively known. Therefore we have started studying the experimental properties of these bands based on Euroball and Gammasphere experiments.

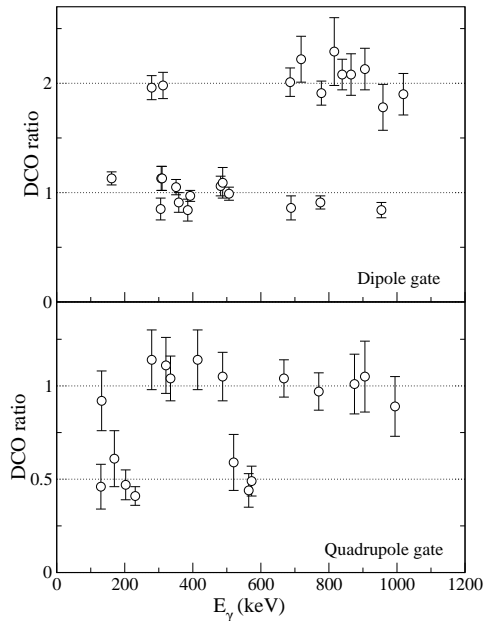


Figure 1. DCO ratios obtained for the ^{132}La γ -rays from the Gammasphere data.

In the present phase of the analysis angular correlation (DCO) study [2] was performed using the data from both experiments in or-

der to obtain γ -ray multipolarity assignments. In Fig. 1 we plotted the results obtained from the Gammasphere data. This analysis was carried out using a BLUE data base. The background subtraction was performed according to the prescription of Ref.[3]. For the analysis the three most forward and the three most backward detector rings were used against the three rings around 90 degrees. In this experimental arrangement DCO ratios of ~ 0.5 and 1.0 are expected for the stretched dipole and stretched quadrupole transitions, respectively, when the gate is set on a quadrupole transition. Also ~ 1.0 DCO ratio value is expected for the $\Delta I=0$ dipole transitions in this case. Using a dipole gate, the expected DCO ratios are ~ 1.0 and ~ 2.0 for the stretched dipole and for the stretched quadrupole as well as for the $\Delta I=0$ dipole transitions, respectively. Based on the observed DCO ratios, and the formerly known spins of lower states, spins were assigned to the band member states where they were not known previously.

- a) OLL, Univ. of Liverpool, Liverpool, UK
 - b) IN2P3-CNRS, Grenoble, France
 - c) Dip. di Fis. and INFN, Padova, Italy
 - d) University of Camerino, Camerino, Italy
 - e) IPN Lyon, IN2P3-CNRS, Villeurbanne, France
 - f) IReS, Strasbourg, France
 - g) Michigan State University, East Lansing, USA
 - h) State University of New York, Stony Brook, USA
 - i) Washington University, St. Louis, USA
 - j) University of York, Heslington, UK
 - k) Wright Nuclear Structure Laboratory, Yale University, New Haven, USA
- [1] A.A. Pasternak et al., Acta Physica Polonica B 40, 647 (2009)
 - [2] K.S. Krane et al., Nucl. Data Tables A 11, 351 (1973)
 - [3] K. Starosta et al., Nucl. Instrum. Methods Phys. Res. A 515, 771 (2003)

2.10 Medium- and high-spin band structure of ^{134}Pr

J. Timár, I. Kuti, D. Sohler, K. Starosta^{a)}, D.B. Fossan^{b)}, T. Koike^{b)}, C.J. Chiara^{c)}, A.J. Boston^{d)}, H.C. Chantler^{d)}, E.S. Paul^{d)}, R. Wadsworth^{e)}, A.A. Hecht^{f)}

Unambiguous identification of intrinsic chirality in rotating triaxial nuclei is one of the most intriguing questions of contemporary high-spin nuclear structure studies. The crossing, strongly linked $\Delta I=1$ rotational band structure, found in ^{134}Pr , was the first experimental candidate for chiral rotation. In order to collect more information on the structure of this key-nucleus among chiral candidates, we studied the rotational bands of ^{134}Pr by in-beam γ -spectroscopic methods.

Excited states of ^{134}Pr were populated using the $^{116}\text{Cd}(^{23}\text{Na},5n)$ reaction at a beam energy of 115 MeV. The experimental setup consisted of the GAMMASPHERE array of 99 HPGe detectors in 16 rings covering a large fraction of the full solid angle. The experiment consisted of two runs; Run 1 performed with a thinner 1.00 mg/cm^2 ^{116}Cd target backed with 15 mg/cm^2 ^{208}Pb was aimed in $\gamma\gamma$ -coincidence

measurements, while Run 2 performed with a thicker self-supporting 1.22 mg/cm^2 ^{116}Cd target was aimed in determination of γ -ray multiplicities in ^{134}Pr . For the off-line analysis, the experimental data obtained were sorted using the BLUE and RADWARE software packages.

The level scheme of ^{134}Pr was deduced using $E_{\gamma 1}-E_{\gamma 2}-E_{\gamma 3}$ triple events, which were sorted into Radware cubes. Typical coincidence spectra are presented in Figure 1. On the basis of the observed $\gamma\gamma\gamma$ -coincidence relations several new bands were found besides the previously published four ones.

- a) Michigan State University, East Lansing, USA
- b) State University of New York, Stony Brook, USA
- c) Washington University, St. Louis, USA
- d) Oliver Lodge Laboratory, University of Liverpool, Liverpool, United Kingdom
- e) University of York, Heslington, United Kingdom
- f) Wright Nuclear Structure Laboratory, Yale University, New Haven, USA

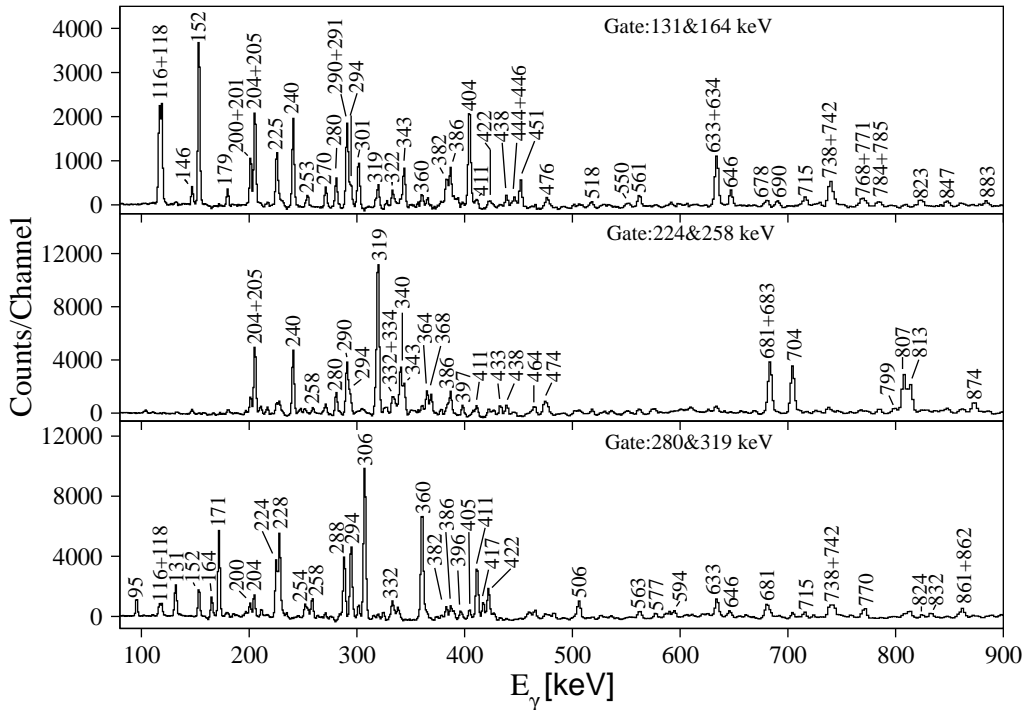


Figure 1. Sample $\gamma\gamma\gamma$ -coincidence spectra of ^{134}Pr obtained in the present work.

2.11 Precise half-life measurement of the 10 h isomer in ^{154}Tb

Gy. Gyürky, G. Rastrepina, Z. Elekes, J. Farkas, Zs. Fülöp, G.G. Kiss, E. Somorjai, T. Szücs

The precise knowledge of the half-life of the reaction product is of crucial importance for a nuclear reaction cross section measurement carried out with the activation technique. The cross section of the $^{151}\text{Eu}(\alpha, n)^{154}\text{Tb}$ reaction has been measured recently using the activation method, however, the half-life of the m1 isomer in ^{154}Tb has a relatively high uncertainty ($T_{1/2}^{m1} = 9.4 \pm 0.4$ h) and ambiguous values can be found in the literature. This uncertainty introduces an error in the measured cross section and therefore the precise determination of the half-life is highly needed.

For the half-life determination, several ^{154}Tb sources have been prepared by the $^{151}\text{Eu}(\alpha, n)^{154}\text{Tb}$ reaction. Highly enriched ^{151}Eu targets have been irradiated with the alpha-beam of the cyclotron of ATOMKI. The targets have been prepared by vacuum evaporation. By choosing different bombarding energies and irradiation times, source activities in the range of 1-100 kBq have been obtained.

The γ -radiation following the β -decay of ^{154}Tb has been measured with a shielded 40% relative efficiency HPGe detector. The length of the countings varied between 20 and 60 hours (more than 6 half-lives) and the spectra were stored in every hour. For the analysis the 540 keV line, the strongest γ -radiation which comes exclusively for the m1 isomer of ^{154}Tb has been selected.

In order to obtain a high precision half-life value, all possible systematic uncertainties have been carefully investigated. The five measured sources gave the same half-life value

within their statistical uncertainty. This shows the robustness of the counting system. However, to increase the reliability of the measurements, the half-life of a reference source is also determined. During α -bombardment the $^{63}\text{Cu}(\alpha, n)$ reaction takes place with high cross section in the target backing producing ^{66}Ga . The half-life of this isotope is similar to that of $^{154}\text{Tb}^{m1}$ (9.49 ± 0.07 h) and it is precisely known. The obtained half-life results for this reference isotope are in all cases in good agreement with the literature value, which shows the reliability of the measurement.

Further systematic uncertainties may arise from the complicated decay scheme of ^{154}Tb . The m2 isomer ($T_{1/2}^{m2} = 22.7 \pm 0.5$ h) is known to have a weak decay branch to the m1 state. This contribution has been taken into account by measuring the production ratio of the two isomers. Although the 540 keV radiation has been reported to come exclusively from the m1 isomer, a hypothetical contribution of the ^{154}Tb ground state decay to this γ -line has been considered. Using a χ^2 analysis, an upper limit could be assigned to this contribution.

A final result of $T_{1/2} = 9.994 \pm 0.039$ h has been obtained for the half-life of the m1 isomer in ^{154}Tb . Compared to the literature value, the half-life is increased significantly and its uncertainty is reduced by one order of magnitude. With this precise measurement one source of uncertainty of the $^{151}\text{Eu}(\alpha, n)^{154}\text{Tb}$ cross section measurement is avoided. Further details can be found in Ref. 1.

[1] Gy. Gyürky *et al.* Nucl. Phys. A **828**, 1 (2009)

2.12 Search for $E(5)$ type nuclei in terms of the sextic oscillator

G. Lévai, J.M. Arias^{a)}

The competition of the short-range pairing force and the long-range quadrupole–quadrupole interaction results in characteristic nuclear shapes, as the former one favors spherical shape, while the latter one induces deformation. The main types of nuclear shapes, the spherical, axially deformed and γ -unstable shapes correspond in the Interacting Boson Model to the U(5), SU(3) and O(6) symmetries, respectively. The quadrupole collective excitations of nuclei can also be described on the phenomenologic level by the Bohr Hamiltonian, which (after separating the angular variables) applies a two-dimensional potential $V(\beta, \gamma)$ defined in terms of the intrinsic β and γ shape variables. The minima of $V(\beta, \gamma)$ correspond to equilibrium shapes. By varying some parameter, e.g. the nucleon number the depth of the minima changes and one potential shape may give way to another one as the ground-state configuration. This phenomenon can be interpreted as a shape phase transition through a critical point.

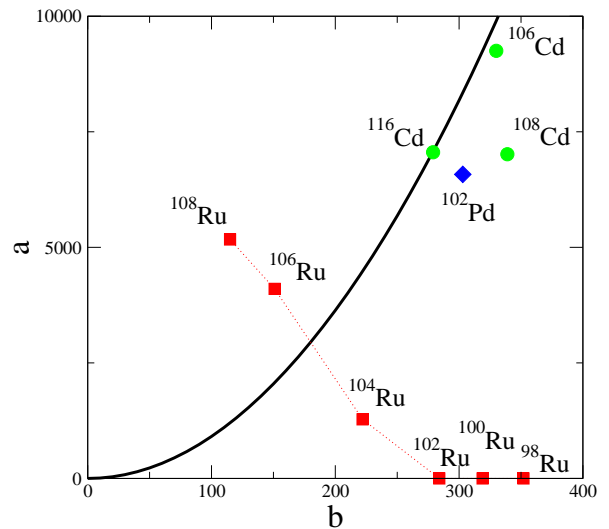
In the simplest case the potential depends only on the β variable, and the Bohr Hamiltonian reduces to a radial Schrödinger equation in five dimensions. Such γ -independent potentials can be used to describe the transitions from the spherical to the γ -unstable shape. This transition was first approximated by an infinite square well in the β variable, which can be solved exactly in terms of Bessel functions. This process was identified as a second-order phase transition and it was associated with the E(5) critical point symmetry. The key spectroscopic properties corresponding to the E(5) symmetry are obtained in a parameter-free form and can be compared with realistic data. Examples for this symmetry were identified near the $Z = 50$ shell closure: ^{134}Ba , ^{104}Ru , ^{102}Pd , $^{106,108}\text{Cd}$, ^{124}Te and ^{128}Xe .

Recently we introduced the sextic oscillator as another model for the spherical to γ -unstable shape phase transition [1]:

$$V(\beta) = (b^2 - 11a)\beta^2 + 2ab\beta^4 + a^2\beta^6. \quad (9)$$

This potential is quasi-exactly solvable meaning that only a subset of its lowest-energy solutions can be obtained exactly, however, these levels coincide with the ones that are essential in identifying the E(5) symmetry. The energy eigenvalues as well as the electric quadrupole and monopole transition rates can be calculated in closed form. The minimum of the potential (9) is spherical ($\beta_0 = 0$) if $b > 0$ and $b^2 > 11a$ hold, while for $b^2 < 11a$ it becomes deformed ($\beta_0 > 0$). The shape phase transition thus occurs along the $b^2 = 11a$ parabola in the parameter space, where furthermore, all the key spectroscopic values (ratios of energy eigenvalues and B(E2)'s, etc.) are constant. This means that the phase transition can be identified by parameter-free benchmark values in the case of the sextic oscillator too [2].

In order to identify further candidates for E(5) symmetry we fitted the energy spectrum of Ru, Pd and Cd nuclei and constructed the corresponding potential. It turned out that all the previously known examples ^{104}Ru , ^{102}Pd , $^{106,108}\text{Cd}$ fell close to the critical parabola, furthermore, the ^{116}Cd was also identified as a new candidate [2].



a) Universidad de Sevilla, Sevilla, Spain

[1] G. Lévai, J. M. Arias, Phys. Rev. C **69** (2004) 014304.

[2] G. Lévai, J. M. Arias, Phys Rev. C **81** (2010) 044304

2.13 Phases of clusterized nuclei

J. Cseh

The atomic nucleus is a rich microscopic laboratory of physical phenomena. Among others it shows evidence for different kind of phase transitions. Some of them are governed by the temperature, like the transition from the liquid to gas phase of the finite nucleonic matter, or from the hadronic to the deconfined phases at higher energy. In some sense these phenomena are similar to the macroscopic phase transitions, apart from the (important role of the) finite-size effects.

There are, however, other kind of phase transitions as well, which take place at (practically) zero temperature. They are called shape-phase transitions. They are not the same, of course, like those which are studied in classical thermodynamics, yet there is so close similarity both on the qualitative, and on the quantitative level, that the language of the phase transitions has been accepted for their discussion.

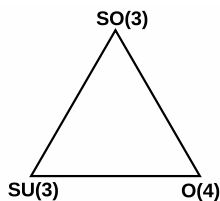


Figure 1. Phase-diagram of the binary cluster model.

A large amount of work has been dedicated to the study of shape-phase transitions in relation with the quadrupole deformation of nuclei. The atomic nuclei have, however, another important type of collectivity as well, based on the dipole degrees of freedom, which is related to the clusterization. The study of the phases and phase transitions of this collectivity has just started [1-3].

In particular, the question of shape-phase transitions due to the relative motion of the clusters have been discussed in [1-3]. This motion is describe by an algebraic model of $U(4)$ group-structure, called vibron model. Actually, the vibron model is applied in molecular physics, and in hadron spectroscopy, too; thus the treatment is similar to those. (The spe-

cific feature in nuclear cluster studies is the important role of the Pauli-principle.) This model has a one-dimensional phase diagram, and a phase transition is expected between the soft vibrator (shell-like clusterization), and the rigid rotor (molecule-like clusterization) phases.

Recently we have extended our investigations [4] by the incorporation of the coupling between the degrees of freedom associated to the relative motion and the internal cluster structure (of a binary cluster system). It turns out that in addition to the $U(3)$ and $O(4)$ dynamical symmetries, a third one, the $O(3)$ dynamical symmetry shows up, as well. Thus the phase diagram is of two-dimensional, and can be illustrated as a triangle, shown in Fig. 1.

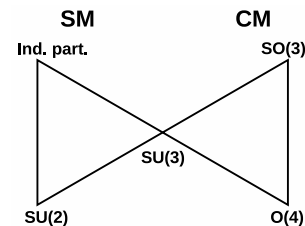


Figure 2. The connection of the phase-diagrams of the cluster and shell models.

A similar phase diagram has been proposed recently for the shell model [5], in which the endpoints represent the $SU(3)$, $SU(2)$, dynamical symmetries, and the independent particle approximation. Since the $SU(3)$ dynamical symmetry is common in the phase diagrams of the shell and cluster models, we propose, that their interrelation is like that on Fig. 2. This can be considered as a formulation of the connection of the two models in terms of their phase diagrams.

- [1] H. Yepez-Martinez, J. Cseh, P.O. Hess, *ATOMKI Ann. Rep.* 2006, 2.17.
- [2] H. Yepez-Martinez, J. Cseh, P.O. Hess, *Phys. Rev. C* **74** (2006) 024319.
- [3] J. Cseh et al, *Int. J. Mod. Phys. E* **17** (2008) 2296.
- [4] J. Cseh, in *Proc. Int. School on Nucl. Phys. Varna, 2009*, in press.
- [5] A. Frank, J. Jolie, P. van Isacker, *Symmetries in Atomic Nuclei*, Springer, NY, 2009.

3.1 Double differential ionization of H₂O by positron impact

Á. Kövér, C. Arcidiacono^{a)}, D.J. Murtagh^{a)}, A.I. Williams^{a)}, G. Laricchia^{a)}

The study of the intrinsic properties of H₂O and of its interactions with various projectiles remains a vigorous multidisciplinary pursuit, spurred by the universal importance of this molecule. In the case of irradiation by positrons (e^+), for example, the role that water radiolysis plays in cell destruction (e.g.[1]) is becoming increasingly pertinent due to the widespread usage of positron emission tomography in medical diagnostics. Here, knowledge of integral and differential cross-sections underpins the understanding of the microscopic distribution of energy deposits needed for accurate dosimetry (e.g.[2]).

H₂O is of special interest due to its strong dipole moment, which has been shown to cause significant forward scattering of electron projectiles [3]. Recently, the fragmentation of H₂O has been investigated around 0° as a function of the energy loss of the positron projectile, at 100 and 153 eV impact energies [4]. The main aims of this work have been to investigate whether forward scattering enhances the probability of ECC around 0° and to measure the intensity ratios of different fragments at various projectile energies.

Fig. 1 shows the results for H₂O⁺ fragments at 100 eV positron impact energy. No ECC peak has been found in the double differential electron spectrum, similarly to the earlier results obtained with Ar [5], indicating that the strong dipole moment of the water does not significantly enhance the ECC process for positron projectiles. However, a small shoulder around 28 eV energy loss has been recorded at both projectile energies. This structure may be consistent with the results of high resolution electron momentum spectroscopy ([6] and references therein), identifying 27.1 eV as the onset of a weak shake-up band connected with the 2a₁ orbital.

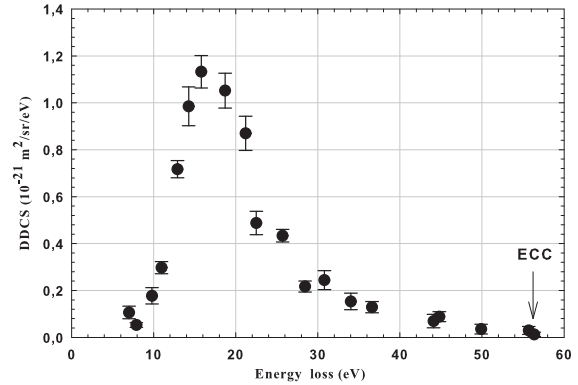


Figure 1. Energy loss spectrum of positron scattered projectile in coincidence with the H₂O⁺ fragments at 100 eV impact energy).

Acknowledgements

This work is sponsored by Engineering and Physical Science Research Council UK (Grant no. GR/S16041/01, EP/E053521/1), Hungarian Scientific Research Foundation (NKTH-OTKA, Grant No. 67719, OTKA K73703), the European Union (HPRN-CT-2002-00179 EPIC), and COST-STSM-P9-02555.

a) UCL Department of Physics and Astronomy, University College London, Gower Street, London, WC1E 6BT, UK

- [1] F. Alvarado, R. Hoekstra and T. Schlatholter, *J. Phys. B: At. Mol. Opt. Phys.* **38** (2005) 4085.
- [2] C. Champion and C. Le Loirec, *Phys. Med. Biol.* **51** (2006) 1707.
- [3] K L. Baluja, R. Zhang, J. Franz and J. Tennyson, *J. Phys. B: At.Mol. Opt. Phys.* **40** (2007) 3515.
- [4] C. Arcidiacono, J. Beale, Z D. PeĀić, Á. Kövér and G. Laricchia, *J.Phys.B: At.Mol.Opt.Phys.* **42**(2009) 065205
- [5] Á. Kövér, G. Laricchia and M. Charlton, *J.Phys.B: At.Mol.Opt.Phys.* **26** (1993) L575.
- [6] CG. Ning, B. Hajgato, YR. Huang, SF. Zhang, K. Liu, Z H. Luo , S. Knippenberg, JK. Deng and MS. Delueze , *Chem. Phys* **343** (2008)19.

3.2 A reaction microscope for studies positron - atom collisions

Á. Kövér, D.J. Murtagh^{a)}, A.I. Williams^{a)}, G. Laricchia^{a)}

Differential investigations, especially in positron physics, are very time consuming. The data collection takes weeks if not months. In order to reduce the data collection time or increase the accuracy of the measured data, new methods are necessary.

A recently developed system combines the advantages of the above mentioned methods i.e. simultaneous energy and angular detection, by measuring the energy and angular distribution of the recoil ion. A further benefit is the 4π collection of the recoil ions comparing with the traditional methods where only a small part of the collision events can be detected. This method, called Cold Target Recoil Ion Momentum Spectroscopy (COLTRIMS), has been successfully applied for investigating ion, electron and photon collisions (see [1] and reference therein). When the residual ions are recorded in coincidence with the outgoing fragments, a kinematically complete picture can be determined about the correlated motion of the fragments of atomic and molecular breakup processes.

Up till now the COLTRIMS have not been used in positron collision physics due to the serious requirement for the quality of the projectile and the target beam. For good time and position resolution timed projectile beam of about 1mm or less diameter is necessary. For the target beam the requirements are similar: the diameter must be small (around 1 mm) and very dense ($10^{11} - 10^{13} \text{atom/cm}^3$) due to the low projectile beam intensity. A further requirement is the small initial momentum distribution of the target atoms due to the small momentum transfer (0.3-4 a.u.) during collision. (The momentum distribution of He is 5.8 a.u. at room temperature.) The solution is using a supersonic gas target which has small diameter, high density and small momentum distribution. It is about 0.05 - 0.2 a.u. in the jet direction [1].

Application of the COLTRIMS method in

positron physics has several advantages in spite of the technical difficulties. The detection of the outgoing residual ion in 4π means the all the collision events can be detected which greatly reduced measuring time. From the measured time of flight of the ions the longitudinal energy of the ions can be determined which corresponds to the different collision processes (ionization, capture to bound/excited states, etc.) and the origin of the ionized electron. The ejection angle of the ion gives information on the dynamics of the collision process especially when it is measured in coincidence with other fragments.

An electrostatic lens system has been built at the UCL Department of Physics and Astronomy, University College London to transport and focus positrons into a narrow beam which will be crossed with a supersonic gas jet. A differentially pumped vacuum system is used, in which a supersonic expanding gas is skimmed successively to produce a collimated cold target. Finally, a spectrometer will be used to accelerate ions onto a position sensitive detector to image the final states of collisions [2][3].

Acknowledgements

This work is sponsored by Engineering and Physical Science Research Council UK (Grant no. GR/S16041/01, EP/E053521/1), Hungarian Scientific Research Foundation (NKTH-OTKA, Grant No. 67719, OTKA K73703), the European Union (HPRN-CT-2002-00179 EPIC), and COST-STSM-P9-02555.

a) UCL Department of Physics and Astronomy, University College London, Gower Street, London, WC1E 6BT, UK

- [1] R. Dorner, V. Mergel, O. Jagutzki, L. Spielberger, J. Ullrich, R. Moshammer and H. Schmidt-Bocking, Physics Reports **330** (2000) 95.
- [2] Á. Kövér, D.J. Murtagh, A.I. Williams and G. Laricchia J. Phys. Conf. Series (2010) in press
- [3] A. I. Williams, Á. Kövér, D. J. Murtagh and G. Laricchia J. Phys. Conf. Series (2010) in press

3.3 Electron Guiding through Insulating Nanocapillaries

K. Schiessl^{a)}, K. Tórkési, B. Solleder^{a)}, C. Lemell^{a)}, J. Burgdörfer^{a)}

The very recent observation of a guiding effect for electrons through Al_2O_3 [1] and PET capillaries [2] came as surprise. Electrons are unlikely to encounter a Coulomb mirror as strong as in the case of highly charged ions guiding. Secondary electron emission coefficients for electron impact with a few hundred eV energy may suggest even positive charge up resulting in attraction to rather than repulsion from the surface. Additionally, even in absence of any charge up, the attractive long-range polarization potential (image potential) steers electrons towards the surface. This suggests that a fundamentally different guiding scenario must prevail. Indeed, first experimental data [2] show a significant and, in many cases, dominant fraction of guided electrons having suffered considerable energy loss pointing to inelastic scattering events.

In this work, we present the first microscopic simulation of electron transmission through insulating nanocapillaries within the framework of the mean-field classical transport theory (CTT). Within the CTT, it is possible to include quantum scattering effects via the collision kernel for the evolution of the ensemble of classical particles. We have shown for the first time [3] that the electron guiding scenario through nanocapillaries entirely different from that for highly charged ions (see Fig. 1). Quantal specular reflection at an attractive average surface potential and multiple smallangle elastic and inelastic scattering are key to guiding. Charge up of the surface does play only a minor role in the guiding process as opposed to the case of highly charged ionic projectiles where strong electrostatic fields are required for guiding through insulating materials. In view of the complexity of the underlying processes, we find surprisingly good agreement with available data.

One consequence of this scenario is the prediction that electron guiding should also be operational for other materials, in particular, for metallic nanocapillaries. However, we expect reduced elastic transmission due to the smaller

specular-reflection probability for metallic surfaces. We hope this hypothesis will be experimentally tested in the near future.

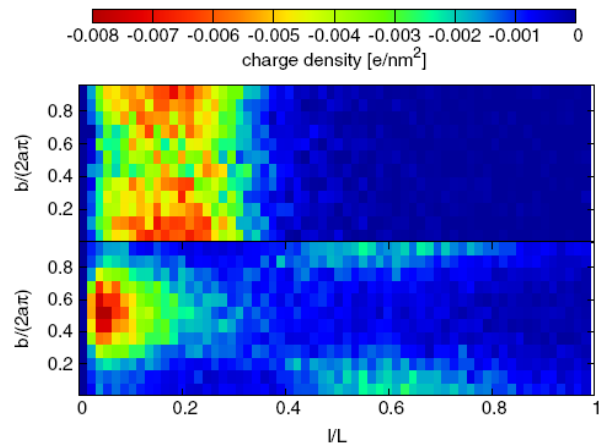


Figure 1. (color online). Equilibrium charge density on the internal walls of a PET capillary for $\theta_{in} = 3^\circ$. The primary impact region of projectile electrons is situated at a cylinder arc length of $b = 0.5/(2\pi a)$. The upper panel shows the result of the present simulation, the bottom panel shows $(-\rho)$ for ion guiding with charge $q=1$. The total charge accumulated on the capillary wall is in both cases $\sim 6000 |e|$.

Acknowledgements

This work was supported by the Austrian Fonds zur Förderung der wissenschaftlichen Forschung under Grants No. FWF-SFB016 ADLIS, No. 17449, No. 17359, and the TeT Grant No. AT-7/2007. One of us (K. T.) was also partially supported by the grant Bolyai from the Hungarian Academy of Sciences and the Hungarian National Office for Research and Technology. K. S. acknowledges support by the IMPRS-APS program of the MPQ (Germany).

- a) Institute for Theoretical Physics, Vienna University of Technology, Wiedner Hauptstrasse 8-10, A-1040 Vienna, Austria, EU
- [1] A. R. Milosavljević et al., Phys. Rev. A 75, 030901(R) (2007).
- [2] S. Das et al., Phys. Rev. A 76, 042716 (2007).
- [3] K. Schiessl, K. Tórkési, B. Solleder, C. Lemell, J. Burgdörfer, Phys. Rev. Lett. **102**, 163201 (2009).

3.4 Angular and energy differential electron emission cross sections in collisions between antiprotons and helium atoms

K. Tókési, J. Wang^{a)}, L. Gulyás, J. Burgdörfer^{b)}

Proton-atom collisions have one particularly interesting feature in the ionization process, namely the electron capture to continuum (ECC) peak that was discovered in 1970 in the doubly differential cross section (DDCS) of ejected electrons at 0° . The ECC process is well understood when the projectile is a heavy and positively charged particle. It can be explained as a result of the capture of the ionized target electron into the low-lying continuum states in the projectile's reference frame. In the electron spectrum the ECC peak appears at that energy, where the electron velocity matches the projectile velocity. The most important dynamical mechanism for ECC is the Coulomb focusing of the ejected target electron in the direction of the outgoing projectile due to the attractive interaction between them. Extending the scenario of the cusp formation for negatively charged projectiles, it works in the opposite way. Due to the strong Coulomb repulsion between the projectile (for example antiproton, electron or other negative ions) and the ionized target electron, an electron yield deficit will appear at the energy where the projectile velocity matches the ejected electron velocity. We therefore can expect the formation of the so called anti-cusp in the similar fashion as the cusp is formed in the case of positively charged projectile [1].

In this paper we present ionization cross sections of helium in collisions between antiprotons and helium atoms at 100 keV impact energy. We apply the continuum distorted wave eikonal initial state (CDW-EIS) and a three-body classical trajectory Monte Carlo (CTMC) methods. We have shown clear evidence for the formation of the anti-cusp in the differential cross sections in both CDW-EIS and CTMC results (see Fig. 1.). Some differences exist between the quantal and clas-

sical results. For example, the CTMC calculations show a larger width in energy of the anti-cusp where the Coulomb repulsion expels the electrons from the direction of the anti-proton. Further studies are necessary to resolve these discrepancies.

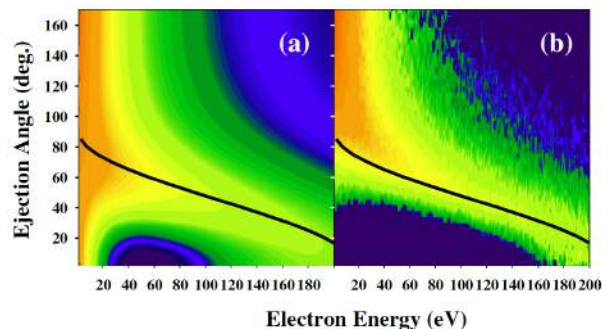


Figure 1. (Color online) Doubly differential electron emission cross sections emitted from He at 100 keV anti-proton impact. a) CDW-EIS b) CTMC. For visual guidance, the lines represent the classical binary encounter relationship according to $E = 4m/ME_p \cos^2 \theta$, where m/M is the mass ratio between the electron and the projectile, E_p the projectile energy, and θ the ejection angle.

Acknowledgements

This work was supported by the grant Bolyai from the Hungarian Academy of Sciences, the TeT Grant Nos. AT-7/2007, and JP-21/2006, the Hungarian National Office for Research and Technology, and the Hungarian Scientific Research Found OTKA K72172. JB acknowledges support from FWF (Austria).

- a) Department of Physics, University of Massachusetts Dartmouth, North Dartmouth, MA 02747, USA
- b) Institute for Theoretical Physics, Vienna University of Technology, Wiedner Hauptstrasse 8-10, A-1040 Vienna, Austria, EU

[1] K. Tókési, J. Wang, L. Gulyás, J. Burgdörfer, *Hyperfine Interact* **194** (2009) 45.

3.5 Atomic Ionization by Ultrashort Half-Cycle Pulses

D.G. Arbó^{a)}, M.S. Gravielle^{a,b)}, K. Tórkési, S. Borbély^{c)}, K. Dimitriou^{d)}, J.E. Miraglia^{a,b)}

In the last decade short unidirectional electric pulses, termed half-cycle pulses (HCP) have had several applications like focusing of Rydberg wave packets, production of one-dimensional Rydberg atoms, and the generation of quasiclassical Bohr-like atoms [1,2]. In this work we calculate total ionization probabilities and energy distributions of ejected electrons by ionization of a hydrogen atom initially in its ground state through different methods. We use (i) the classical trajectory Monte Carlo (CTMC) method [3], (ii) the single distorted Coulomb Volkov approximation (CVA) and (iii) the impulsive Coulomb Volkov approximation (ICV). In the latter both final and initial channels are distorted (Eq. (7) in [4]).

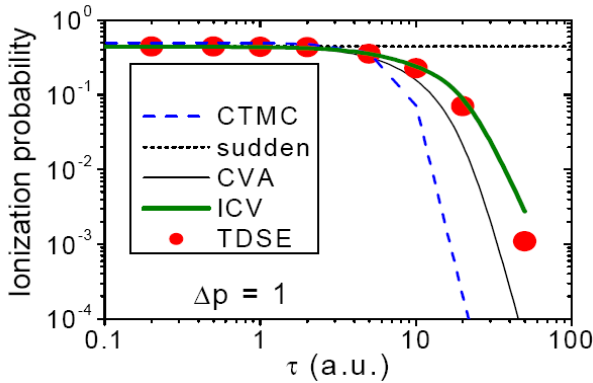


Figure 1. (color online). Total ionization probability as a function of the pulse duration of a HCP of $\Delta p = 1$.

In Fig. 1 we display the total ionization probability, as a function of the pulse duration τ . We observe that in the limit of short pulses all theories converge to the sudden limit ($\tau \rightarrow 0$). But for long pulses CTMC is unable to reproduce the exact time dependent Schrödinger equation results (TDSE) due to the well known classical suppression. The CVA also fails to reproduce the long pulse regime which is overcome with the more accurate ICV.

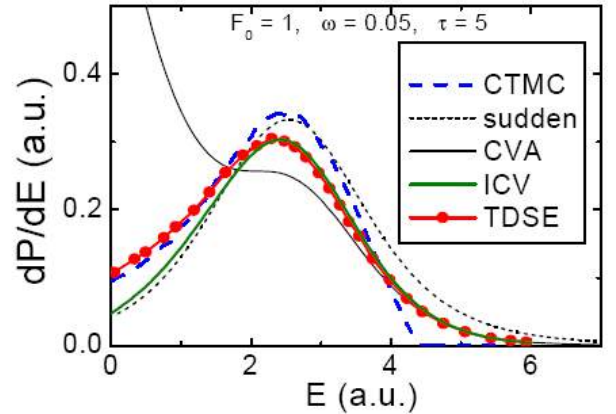


Figure 2. (color online). Energy distribution of an electron ionized by a HCP of duration $\tau = 5$ and peak field $F_0 = 1$.

In Fig. 2 we observe that for $\tau = 5$ the CVA energy distribution diverges at threshold which is solved by the ICV. CTMC reproduces the exact results for low energies with a cutoff due to the improper classical initial distribution [5].

Acknowledgements

Work supported by Conicet, Anpcyt PICT772, Argentina-Hungary collaboration PA05-EIII/007, grant Bolyai Hungarian Academy of Sciences.

- a) Institute for Astronomy and Space Physics, IAFE, CC67, SUC. 28 (1428) Buenos Aires, Argentina
- b) Department of Physics, FCEN, University of Buenos Aires, Argentina
- c) Faculty of Physics, Babes-Bolyai University, Kogalniceanu Street No. 1, 400084 Cluj-Napoca, Romania
- d) Hellenic Army Academy, Department of Natural Science and Applications, Vari, Greece

- [1] D.G. Arbó, et al., 2003, Phys. Rev. A 67 063401.
- [2] J.J. Mestayer, et al., 2008, Phys. Rev. Lett. 100 243004.
- [3] K. Tórkési and G. Hock, 1996, J. Phys. B 29 119.
- [4] P.A. Macri, et al., 2003, J. Opt. Soc. Am. B 20 1801.
- [5] D.G. Arbó, et al., 2009, Eur. Phys. J. D. 51 303.

3.6 Single and double ionization of He by slow antiproton impact

S. Nagele^{a)}, J. Feist^{a)}, S. Borbély^{b)}, K. Tókési, L. Nagy^{b)}, J. Burgdörfer^{a)}

The collision of antiprotons with helium atoms is a fundamental process in many-body atomic physics which long has attracted considerable interest. Due to the negative charge of the antiproton, no electron transfer can occur which facilitates the theoretical treatment of the problem.

So far, total cross sections for single and double ionization have been obtained, both experimentally and theoretically, for a wide range of impact energies from 3 keV up to a few MeV (see [1,2] and references therein). For high impact energies theory and experiment agree very well. However, below ~ 30 keV discrepancies between different theoretical approaches and experiments emerge.

We presented results from *ab initio* calculations in this energy range. Our approach is based on the numerical solution of the time dependent Schrödinger equation (TDSE) using the time dependent close-coupling (TDCC) method. The inter-electronic interaction is treated without approximation. The incoming antiproton is treated as a classical point-like charge and taken into account by its time-dependent Coulomb potential. The wave function is expanded in coupled spherical harmonics, and the radial part is discretized using a finite element discrete representation (FEDVR). For temporal propagation we employ the short iterative Lanczos method with adaptive time-step control. The fully correlated ground state wave function for helium is obtained via imaginary time propagation.

We presented total, integrated, single and double ionization cross sections and compare them with experimental data and other recent theoretical calculations [3]. In addition, we calculated (doubly) differential cross sections (with respect to the energies of the emitted

electrons). We also aim towards angle-energy differential cross sections which, so far, could not be calculated using *ab initio* methods. Differential cross sections are expected to be obtained in the future at the Facility for Antiproton and Ion Research (FAIR) [4] where kinematically complete measurements might be feasible.

Acknowledgements

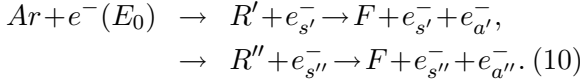
This work was supported by the Austrian Fonds zur Förderung der wissenschaftlichen Forschung under Grants No. FWF-SFB016 ADLIS, No. 17449, No. 17359, and the TeT Grant No. AT-7/2007. One of us (K. T.) was also partially supported by the grant Bolyai from the Hungarian Academy of Sciences and the Hungarian National Office for Research and Technology.

- a) Institute for Theoretical Physics, Vienna University of Technology, Wiedner Hauptstrasse 8-10, A-1040 Vienna, Austria, EU
- b) Faculty of Physics, Babes-Bolyai University, Kogalniceanu Street No. 1, 400084 Cluj-Napoca, Romania
- [1] H. Knudsen, H.-P.E. Kristiansen, H.D. Thomsen, U.I. Uggerhoj, T. Ichioka, S.P. Moller, C.A. Hunniford, R.W. McCullough, M. Charlton, N. Kuroda, Y. Nagata, H. A. Torii, Y. Yamazaki, H. Imao, H.H. Andersen and, K. Tókési, *Phys. Rev. Lett.***101** (2008) 043201.
- [2] H. Knudsen, H.-P.E. Kristiansen, H.D. Thomsen, U.I. Uggerhoj, T. Ichioka, S.P. Moller, C.A. Hunniford, R.W. McCullough, M. Charlton, N. Kuroda, Y. Nagata, H.A. Torii, Y. Yamazaki, H. Imao, H.H. Andersen and, K. Tókési, *Nucl. Instrum. Methods Phys. Res. Sect. B* **267** (2009) 244.
- [3] M. Foster, J. Colgan, M.S. Pindzola, *Phys. Rev. Lett.* **100** (2008) 033201.
- [4] C.P. Welsch, J. Ullrich, *Hyperfine Interact.* **172** (2007) 71.

3.7 State-to-state interference in electron induced resonant Auger decay

M. Žitnik^{a)}, B. Paripás^{b)}, B. Palásthy^{b)}, M. Kavčič^{a)}, K. Bučar^{a)}, K. Tórkési

Suppose that two resonances, R' and R'' are created by electron scattering on the atomic ground state and that they can decay by electron emission into the same final state F:



Electron pairs ($E_a; E_b$) are observed in coincidence by two electron analyzers and the necessary condition for the interference is that the energy of the scattered electron from one reaction path equals energy of Auger electron released along the other reaction path: in that case the electron pairs ($e_{s'}^-, e_{a'}^-$) and ($e_{s''}^-, e_{a''}^-$) are indistinguishable. For given states the interference occurs at unique electron impact energy $E_0 = E_{R'} + E_{R''} - E_F$. We have selected $\text{Ar} + [3p^2](^1D)3d\ ^2P; ^2D$ with excitation energy $E_F = 37.15 - 37.40$ eV since these final states are populated with reasonable intensity from both resonances: $[2p3=2]3d$ with excitation energy $E_{R'} = 246.927$ eV and $[2p_{3/2}]4d$ with excitation energy $E_{R''} = 247.669$ eV. Here, the state-to-state interference is expected to occur at $E_0 = 457.3$ eV and for electron pairs (209.6 eV, 210.4 eV) and (210.4 eV, 209.6 eV). The electron-electron coincidence experiment was performed at University of Miskolc by two electrostatic spectrometers, a single and a double pass cylindrical mirror analyser with HWHM energy resolution of 0.45% and 0.25%, respectively. They were mounted on the same axis, perpendicular to the electron projectile beam and in near vicinity of the gas entrance into the chamber. Large accepted solid angle ($0.015 \times 4\pi$ sr), essential to accumulate statistically significant data in reasonable time, was provided by 5° wide entrance cones. Our sim-

ulation of the (e; 2e) spectral plane is based on known resonance energies [1] and known decay branching ratios from photon impact experiments [2]. In addition, the missing branching ratios for the resonant Auger decay of $[2p_{3/2}]4p$ state (given essentially by amplitude B in Fig. 1) were provided by coincidence measurements at 350 eV electron impact energy, where also the Ar 2p energy loss spectrum was measured. We found that our model reproduces quite well the experimental data except for the PCI shift of "normal" Auger lines (due to the presence of additional slow ejected electron) and the missing intensity at 210 eV which is explained by destructive interference of amplitudes A' and A'' pertaining to two interfering electron pairs.

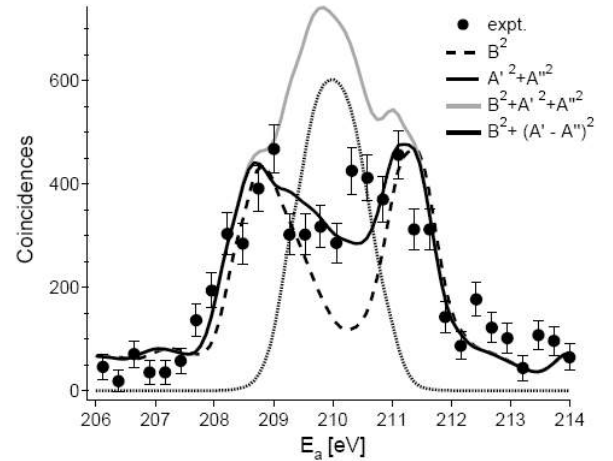


Figure 1. A cut through the two "interference" points in (e,2e) spectral plane, projected onto E_a axis.

- a) Jožef Stefan Institute, P.O. Box 3000, SI-1001 Ljubljana, Slovenia
- b) Department of Physics, University of Miskolc, 3515 Miskolc-Egyetemváros, Hungary

[1] G.C. King, et al., 1977, J. Phys. B 10 2479

[2] J.A. de Gouw, et al., 1995, J. Phys. B 28 2127

3.8 Multiple electron scattering sequences in $C^{q+} + Ar$ collisions at energies and charge states relevant for carbon ion therapy

K. Tőkési, B. Sulik

Secondary electrons, created in biological tissues by high energy ion impact, may significantly contribute to the fragmentation of small molecules up to single- and double-strand breaks in DNA. Differential spectra of electrons emitted in the collisions of decelerating ions are very important for estimating ion impact radiation damages.

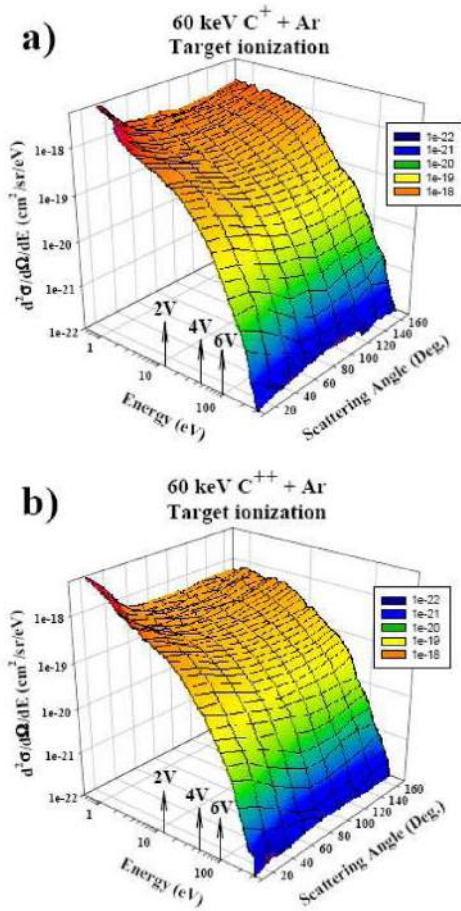


Figure 1. Double differential cross section for target electron emission as a function of electron energy and scattering angle.

In this work, we consider a specific ionization mechanism, the so called Fermi-shuttle acceleration, which can produce fast electrons even by slow ion impact. Focusing our interest to the distal region of the Bragg peak, we calculate electron spectra for singly and doubly charged carbon ions using the classical trajectory Monte Carlo method at 60 keV impact energy, where large fragmentation yields for water molecules have recently been observed experimentally.

Our preliminary results indicate unexpectedly long sequences of multiple scattering in the studied projectile energy range [1]. Since this is already the quasi-molecular collision regime, these classical predictions should be tested by both experiments and quantum calculations. The latter, however is not very easy. Quantum and classical calculations could be compared first for much simpler collision systems. According to our preliminary statistics, multiple (3-fold or higher order) scattering sequences dominantly contribute (with $\sim 70\%$) to the electron emission above 15 eV energy. As a next step, the predicted double differential cross sections should be tested by experiment.

Acknowledgements

This work was supported by the Hungarian National Science Foundation, OTKA (Grant Nos: K073703, K72172), the grant Bolyai from the Hungarian Academy of Sciences, the TeT Grant No. JP-21/2006, and the Hungarian National Office for Research and Technology.

[1] K. Tőkési, and B. Sulik, *Journal of Physics: Conference Series* **163** (2009) 012073

3.9 Ionization of the H_2^+ by intense ultrashort laser pulses

S. Borbély^{a)}, L. Nagy^{a)}, K. Tókési

Interference effects in the ionization of the hydrogen molecule due to the two-center character of the target have been observed experimentally and studied theoretically both for charged particle [1] and photon [2] impact. The interference patterns can be clearly observed in the ionization probability densities as deep minima for fixed molecular axis orientations (see Fig. 1.). In the present work triple differential ionization probabilities are calculated using exact numerical and approximate analytical solution of the time dependent Schrödinger equation (TDSE) for different laser pulse parameters. Classical calculations were also performed using the classical trajectory Monte Carlo (CTMC) method. In our quantum mechanical calculations the exact analytical [3] initial state wave function was used. In the Volkov model the Coulomb potential is neglected, in the momentum-space strongfield approximation (MSFA) [4] it is considered as a first order perturbation, while in the case of TDSE and CTMC models it is fully considered during the action of the laser field. By comparing the results of these models we were able to study in which situation the Coulomb potential has an important influence on the studied systems time propagation. Plane waves, single- and two-center Coulomb functions [5] were used to represent the final state of the ionized electrons, which gave us the possibility to analyze the influence of the final state wavefunction on the interference pattern. It was found that for each studied pulse the correct initial and final state wave functions were crucial for precise results, while for short and intense pulses the Coulomb potential does not influence significantly the time propagation of the active electron.

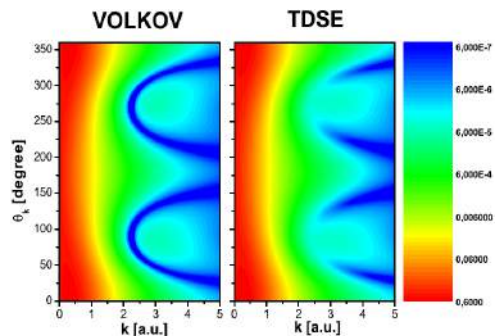


Figure 1. Ionization probability densities in the collisional plane (defined by the molecular axis and the polarization vector of the laser field) as a function of the electron momentum (k) and electron ejection angle (θ_k measured from the polarization vector) for a molecular axis perpendicular to the polarization vector.

Acknowledgements

This work was supported by the Romanian National Plan for Research (PNII) under contract No. ID 539, the European COST Action CM0702, the grant Bolyai from the Hungarian Academy of Sciences, and the Hungarian Research Found OTKA (K72172).

- a) Faculty of Physics, Babes-Bolyai University, Kogalniceanu Street No. 1, 400084 Cluj-Napoca, Romania
- [1] N. Stolterfoht, et al., Phys. Rev. Lett. **87** (2001) 023201.
 - [2] H.D. Cohen and U. Fano, Phys. Rev. **150** (1966) 30.
 - [3] D.R. Bates, et al., Philos. Trans. R. Soc. London **246** (1953) 215.
 - [4] S. Borbély, L. Nagy and K. Tókési, Phys. Rev. A **77** (2008) 033412.
 - [5] S. Borbély and L. Nagy, Rad. Phys. Chem. **76** (2007) 516.

3.10 Ionization of the H₂O molecule by intense ultrashort laser pulses

S. Borbély^{a)}, K. Tókési, L. Nagy^{a)}, D.G. Arbó^{b)}

In the present work calculations for the ionization of the water molecule by intense half-cycle electric pulses were presented. Single active electron classical (CTMC- classical trajectory Monte Carlo) and quantum-mechanical (numerical solution of the time dependent Schrödinger equation (TDSE)) models were employed in the framework of the hydrogenic approximation. In the hydrogenic approximation the 1b₁ electrons are initialized on a 2p_z hydrogenic orbital. The effective charge of the core (Z_{eff}) is calculated using the experimental value of the ionization energy $E_i = 0.463$ a.u. Calculations were performed using electric pulses with duration τ of 1, 3, and 5 a.u. at two different field intensities ($E_0 = 0.44$ a.u. and $E_0 = 1$ a.u.).

Ionization probability densities are calculated the TDSE and VOLKOV expansion coefficients along with the orthogonalized TDSE (TDSE-O model) and Volkov (VOLKOV-O model) expansion coefficients. The CTMC ionization probability densities are calculated from the simulated classical trajectories.

The probability densities predicted by quantum mechanical and classical models are qualitatively the same. In each approach the electrons are ejected with maximum probability along the polarization vector with momentum value around $\vec{A}(\tau)$, which is the momentum gained by the electrons from the external electric field. A double-peak structure in the ionization probability densities can be observed applying both the Volkov and TDSE models. This is the imprint of the double lobe structure of the initial state wave function. In the TDSE, TDSE-O and VOLKOV-O probability densities a parallel “ridge” structure was observed, which were identified as single-photon ionization peaks attributed to the shape of the half-cycle pulse.

The ionization spectra can be calculated from the ionization probability density by integrating over the electron ejection angles. We found a good agreement between the CTMC and TDSE results (see figure 1) only for pulses

with high net momentum transfer toward the active electron, where the dominant ionization mechanism is the over-the barrier ionization.

Both the TDSE and VOLKOV models provide qualitatively the same results. In both cases, the dP/dk curve has two maxima around the same electron momenta. Beside these similarities, significant discrepancies exist. In the case of the Volkov model both maxima have the same height, while in the case of TDSE model the first maximum is considerably smaller than the second one. This difference in the height of the maxima can be also observed for the CTMC model and can be explained as a result of the Coulomb interaction between the core and the electron, which is absent for the Volkov model.

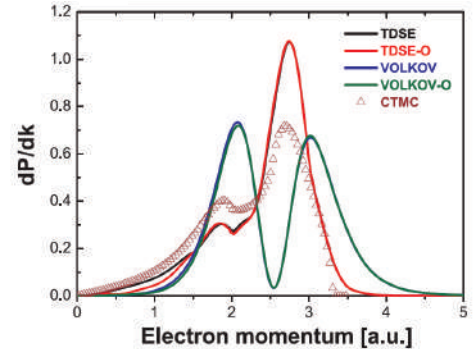


Figure 1. Ionization probability densities as a function of electron momentum at laser pulse parameter $E_0 = 1$ a.u., $\tau = 5$ a.u.

Acknowledgements

This work was supported by the Romanian National Plan for Research (PNII) under contract No. ID 539, the European COST Action CM0702, the grant Bolyai from the Hungarian Academy of Sciences, and the Hungarian Research Found OTKA (K72172).

- a) Faculty of Physics, Babes-Bolyai University, Kogalniceanu Street No. 1, 400084 Cluj-Napoca, Romania
- b) Institute for Astronomy and Space Physics, IAFE, CC67, SUC. 28 (1428) Buenos Aires, Argentina

3.11 ECR Plasma Photos

R. Rácz, S. Biri, J. Pálinkás

In order to observe and study systematically the plasma of electron cyclotron resonance (ECR) ion sources (ECRIS) we made a high number of high-resolution visible light plasma photos and movies in the ATOMKI ECRIS Laboratory. This required building the ECR ion source into an open plasma device, temporarily. An 8MP digital camera was used to record photos of plasmas made from He, methane, N, O, Ne, Ar, Kr, Xe gases and from their mixtures. The effects of the main external setting parameters (gas pressure, gas composition, magnetic field, microwave power, microwave frequency) were studied to the shape, color and structure of the plasma. The double frequency mode (9+14 GHz) was also realized and photos of this special “star-in-star” shape plasma were recorded. A study was performed to analyze and understand the color of the ECR plasmas. The analysis of the photo series gave us many qualitative and numerous valuable physical information on the nature of ECR plasmas [1, 2]. To our best knowledge our work is the first systematic study of ECR plasmas in the visible light region.

When looking in the plasma chamber of an ECRIS we can see an axial image of the plasma (figure 1) in conformity with experimental setup.

Structure of the ECR plasmas

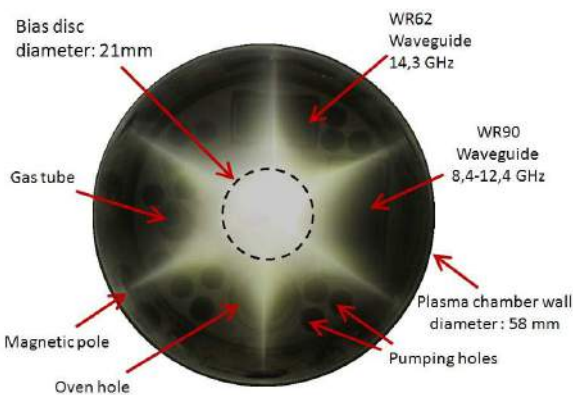


Figure 1. Typical axial image of the plasma with explanatory texts.

Most of the quantitative information was obtained through the summarised values of the Analogue Digital Unit (ADU) of pixels. By decreasing the strength of the magnetic trap we clearly observed that the brightness of the central part of the plasma gradually decreases, i.e. the plasma becomes more and more “empty”. Figure 2 shows a photo series of ECR plasma at decreasing axial magnetic field. The radial size of the plasma increased because of the ascendant resonant zone.

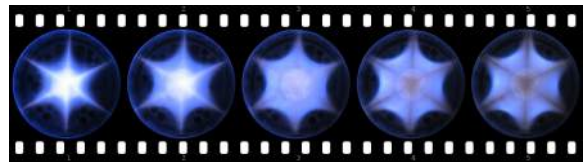


Figure 2. Argon plasma generated by 20W, 9 GHz microwave. The strength of the axial magnetic trap was 1.1T, 0.88T, 0.66T, 0.44T, 0.22T (from left to right, respectively)

By increasing the power of the injected microwave an optimum (or at least saturation) was found in the brightness of the plasma. We found correlation between the gas dosing rates and plasma intensities. When sweeping the frequency of the microwave in a wide region we observed that some frequencies are “better” than others for the point of view of plasma stability and brightness. There exist even frequencies where no plasma could be generated. Finally, a detailed study was carried out to analyze and understand the color of ECR plasmas [2]. More photos can be found in the homepage of the ECRIS Laboratory [3].

[1] R. Rácz, S. Biri, J. Pálinkás, *Rev. Sci Instrum.* **81** (2010), accepted for publication.

[2] R. Rácz, S. Biri, J. Pálinkás, *Plasma Sources Sci. and Techn.* (submitted)

[3] <http://www.atomki.hu/ECR>

3.12 Resonant Mn KLL Auger spectra excited from a nanolayer sample

L. Kövér, I. Cserny, W. Drube^{a)}, S. Egri^{b)}, Zs. Jánosfalvi, S. Thiess^{a)}

Analysis of high resolution resonant KLL Auger spectra photoexcited from 3d metals helps to understand better the excitations upon initial hole creation and the effects of the local density of the unoccupied electronic states on these processes. To reduce obscuring effects of multiple electron scattering on the lineshapes, ultrathin metallic layers were studied.

A *Mn* nano-film of < 2 nm thickness was evaporated in situ onto a glassy carbon wafer degassed previously. The cleanliness of the nano-film was proved by photoemission. High energy resolution measurements of the *Mn* KLL Auger spectra were performed with the Tunable High Energy XPS instrument (equipped with a Scienta SES-200 hemispherical analyzer) [1] at the BW2 beamline of HASYLAB using a *Si*(111) photon monochromator and an electron energy resolution of 0.2 eV. Using this equipment, measurements of Auger Resonant Raman effects in resonant KLL Auger spectra of 3d metals [2] and studies of threshold dynamics of the satellites in the spectra [3] have been performed recently. The angle of photon incidence related to the sample surface was just below the critical angle of total external reflexion (about 0.4°) while the angle of electron emission was 45.6°. Compared to bulk solids, the electron spectra obtained exhibit a strong reduction of the inelastic background and the spectral details are enhanced in the resonant spectra. In addition, spurious photoelectron peaks excited by the characteristic X-rays photoinduced internally in a bulk sample are avoided.

Figure 1 shows KLL Auger spectra excited from the *Mn* nanolayer using near K-threshold photon energies. A comparison with similar resonant KLL Auger spectra of a *Ni* nanolayer (obtained earlier [4]), shows that the strong satellite structure in the *Ni* KLL spectra above the K-absorption threshold [2] is missing in the *Mn* KLL spectra, as in the case of *Co* KLL spectra of a *Co* nanolayer [4].

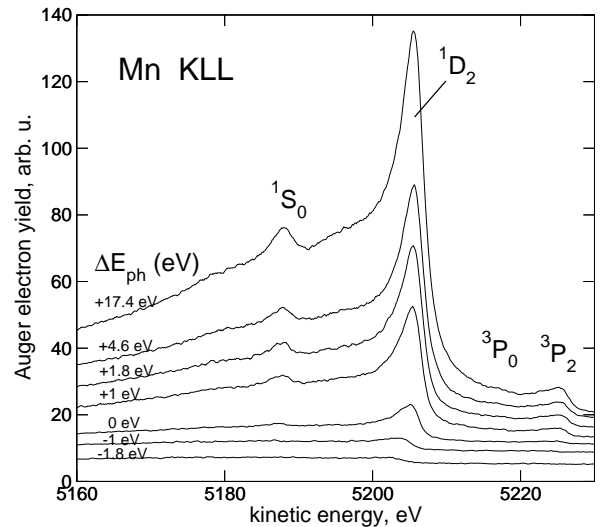


Figure 1. *Mn* KLL Auger spectra photoexcited from a 2 nm thick *Mn* layer deposited on a glassy carbon substrate. The photon energy is referenced relative to the *Mn*-K absorption edge.

Acknowledgements

The research leading to these results has received funding from the European Community's Seventh Framework Programme (FP7/2007-2013) under grant agreement n° 226716 as well as from the Hungarian project OTKA 67873.

- a) HASYLAB/DESY, Notkestraße 85, D-22603 Hamburg, Germany
- b) Department of Experimental Physics, University of Debrecen, 18/a Bem tér, H-4026 Debrecen, Hungary
- [1] W. Drube, T. M. Grehk, R. Treusch and G. Materlik, *J. Electron Spectrosc. Relat. Phenom.* **88-91**, 683 (1998).
- [2] L. Kövér, W. Drube, Z. Berényi, I. Cserny, V. R. R. Medicherla, T. Ishii, H. Ikeno, H. Adachi, *Surface Science* **601**, 1085 (2007).
- [3] L. Kövér, Z. Berényi, I. Cserny, L. Lugosi, W. Drube, T. Mukoyama, V. R. R. Medicherla, *Phys. Rev.* **B73**, 195101 (2006).
- [4] L. Kövér, I. Cserny, W. Drube, M. Novák, S. Egri, S. Thiess, HASYLAB Annual Report 2008.

4.1 Simulation of attosecond streaking of electrons emitted from a tungsten surface

C. Lemell^{a)}, B. Solleder^{a)}, K. Tókési, J. Burgdörfer^{a)}

We have presented simulations of the electron excitation (Fig. 1.), transport, and attosecond streaking for an xuv-pump-nir-probe setting near a tungsten surface [1]. This scenario models the recent experiment by Cavalieri et al. [2]. We find excellent agreement for the energy spectrum in the presence of the streaking field. In agreement with the experiment, we find the core electron emission to be delayed relative to the conduction-band electrons. Calculated run-time differences between groups of photoelectrons are at the lower bound of the error bar of the measurement. Latest experiments indicate a somewhat smaller run-time difference of 85 ± 35 as reducing the gap between measured data and our simulations. Processes responsible for the time delay identified by the present simulation include the larger emission depth of core electrons, the contribution of primary emitted conduction electrons slowed down to energies matching emitted core electrons, as well as secondary electrons. When we include a modification of the group-velocity distribution for energies in the region of core electrons as proposed by Silkin et al. [2], the delay time increases and is closer to the experimental data. We note, however, that invoking this correction would require an energy shift of the spectrum for which a convincing explanation is missing. Possible other mechanisms not yet accounted for include the influence of the nir pulse on the primary photoexcitation process and local crystal-field effects on the emission time spectrum. The impact of both effects could be increased by local-field enhancements at the surface (surface plasmons) as recently shown for the nanoplasmonic field microscope [3]. Such fields might influence excitation and transport of photoelectrons from the conduction-band and bound states differently.

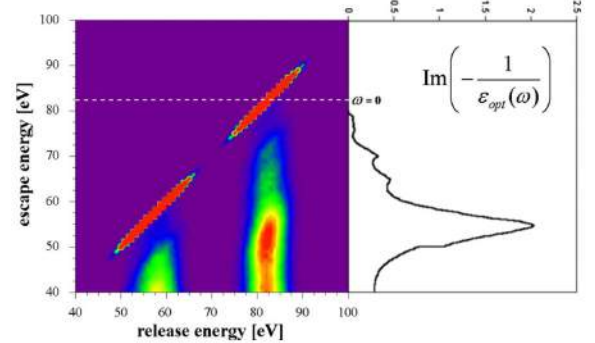


Figure 1. (Color online) Primary excitation energy vs escape energy for photoemission by an xuv pulse ($\hbar\omega=91$ eV) from a W surface. The loss function of tungsten (right-hand side) shows a pronounced excitation (loss channel) at about 25 eV.

Acknowledgements

This work was supported by the Austrian Fonds zur Förderung der wissenschaftlichen Forschung under Grants No. FWF-SFB016 ADLIS and No. 17449, the European ITS-LEIF network under Grant No. RII3 026015, and the TeT under Grant No. AT-7/2007. One of us (K.T.) was also partially supported by the grant Bolyai from the Hungarian Academy of Sciences and the Hungarian National Office for Research and Technology. We thank the group of R. Kienberger (MPQ Garching) for making their latest data available to us prior to publication.

- a) Institute for Theoretical Physics, Vienna University of Technology, Wiedner Hauptstrasse 8-10, A-1040 Vienna, Austria, EU
- [1] C. Lemell, B. Solleder, K. Tókési, J. Burgdörfer, *Phys. Rev. A* **79**, 062901 (2009).
- [2] A. L. Cavalieri, N. Müller, Th. Uphues, V. S. Yakovlev, A. Baltuska, B. Horvath, B. Schmidt, L. Blümel, R. Holzwarth, S. Hendel, M. Drescher, U. Kleineberg, P. M. Echenique, R. Kienberger, F. Krausz, and U. Heinzmann, *Nature (London)* **449**, 1029 (2007).
- [3] C. O. Reinhold and J. Burgdörfer, *Phys. Rev. A* **55**, 450 (1997).

4.2 Monte Carlo simulation of electron spectra scattered elastically from Au-C double-layer sample at relativistic energy

K. Tókési, D. Varga

We performed a Monte Carlo simulation [1] of electron spectra scattered elastically from two Au-C bilayer samples in reflection and transmission mode at the vicinity of the scattering angle of $\theta_0=44.3^\circ$ and at the primary electron energy of 40 keV. Our recent choice of the primary energy, incident and scattering angles was highly motivated by the experimental data published in [2]. The number of elastically scattered events in the used solid angle ($\Delta\Omega=0.03$ sr) was roughly $(0.5-3)\times 10^6$, thanks to the huge amount of primary histories (10^{11}). At the end of each calculation we have many partial distributions, but the most important among them are the following five: the peaks of the single scattering on gold and carbon atoms, the peaks of the multiple scattering on the gold atoms only, and on the carbon atoms only, and the energy distribution of the multiple scattered electrons when both target atoms contribute to the process.

The measurable electron spectra consist of two, more or less, separable peaks as it can be seen on Fig.1, where beside the total energy distributions (red solid lines) we show the peaks belong to the single scattering contribution also for the demonstration of the real yield ratios. Furthermore, results for intensity ratios, peak shifts and broadenings in four cases of measuring geometries and layer thicknesses were analyzed.

While for transmission geometries we found good agreement with the results of the single scattering model in the peak intensity ratios of gold and carbon, especially large differences were obtained in reflection geometries. The separation of the peaks, depending on the geometry and the thickness, generally smaller, and the peak width generally larger than it

can be expected from the nominal values of the primary energy, scattering angle, and mean kinetic energy. It was also shown that the peaks are asymmetric even for the case of the single scattering due to the used finite solid angle.

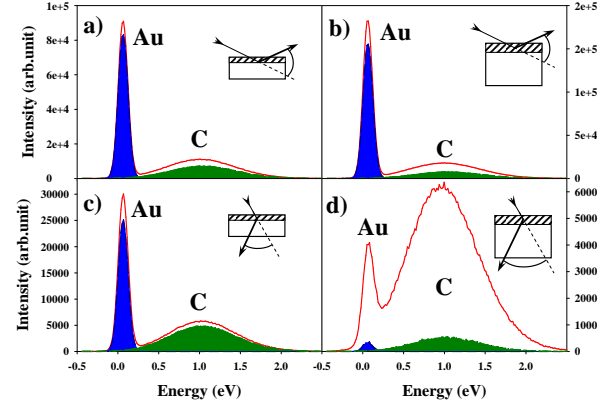


Figure 1. Energy distributions of electrons scattered elastically from Au-C double layer at 40 keV primary energy for two different thicknesses in transmission and reflection geometry. Panel a) - reflection mode, $d_1(\text{Au})=1\text{\AA}$, $d_2(\text{C})=90\text{\AA}$; panel b) - reflection mode, $d_1(\text{Au})=2\text{\AA}$, $d_2(\text{C})=1400\text{\AA}$; panel c) - transmission mode, $d_1(\text{Au})=1\text{\AA}$, $d_2(\text{C})=90\text{\AA}$; panel d) - transmission mode, $d_1(\text{Au})=2\text{\AA}$, $d_2(\text{C})=1400\text{\AA}$. Red solid line: total spectrum, blue area: the single scattering contribution from Au atoms, green area: the single scattering contribution from C atoms.

Acknowledgements

This work was supported by the grant ‘‘Bolyai’’ from the Hungarian Academy of Sciences, the Hungarian National Office for Research and Technology.

- [1] D. Varga, K. Tókési, Z. Berényi, J. Tóth and L. Kövér, *Surf. Interface Anal.* **38** (2006) 544.
- [2] M. Vos, M.R. Went, *Phys. Rev. B* **74** (2006) 205407.

4.3 Quantification of surface effects: Monte Carlo simulation of REELS spectra to obtain surface excitation parameter

K. Salma^{a)}, Z.J. Ding^{a)}, Z.M. Zhang^{b)}, P. Zhang^{a)}, K. Tókési, D. Varga, J. Tóth,

The surface excitation effect is investigated by using the quantum mechanical frame work of complex self-energy of electrons which interact with a bounded semi-infinite medium. In the self-energy formalism, differential inverse inelastic mean free path (DIIMFP) has contributions from bulk and surface plasmons. Monte Carlo simulation of the interaction of electrons with a solid medium and surface has been performed. The surface excitation parameter (SEP) is then obtained from the simulated reflection electron energy loss spectroscopy (REELS) spectra. The calculated SEP results by Monte Carlo simulation are compared with the previous calculations of total surface excitation probability, which was estimated by a numerical integration of surface term of DIIMFP. The contribution merely due to surface excitations towards REELS spectra is extracted by subtracting the two Monte Carlo simulated REELS spectra that based on the two models of electron inelastic scattering, i.e. a full surface model (SM) and a pure bulk model (BM). The surface excitations found to be significant at low energy losses and diminish at higher energy losses whereas the bulk plasmon contributions show opposite behavior and are negligible at lower energy losses. The average number of surface excitations is then evaluated by the computation of ratio of the integrated surface contribution to the elastic peak. The calculated results for Ag are found to be reasonably in agreement with our previous results for total probability of surface excitations and other reported experimental data for SEP. Surface correction factor (SCF) is calculated using SEP for several metals and is compared with the reported ratio of SCF with Ni sample

as reference (see Fig. 1).

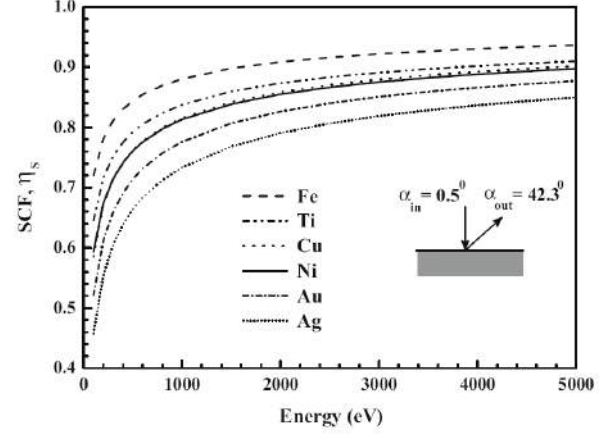


Figure 1. Surface correction factor (SCF) for double surface crossing at angles, $\alpha_{in} = 0^\circ$ and $\alpha_{out} = 42.3^\circ$ for Ag, Au, Cu, Ni, Ti and Fe

Acknowledgements

This work was supported by the National Natural Science Foundation of China (Grant No. 10874160), 111 Project, Chinese Education Ministry and Chinese Academy of Sciences, the grant Bolyai from the Hungarian Academy of Sciences, and TeT Grant No. CHN-28/2003. K. Salma also acknowledges PAEC, Islamabad for the facility to collect some of her work during doctorate studies at USTC, PR China, in the form of present article.

- a) Hefei National Laboratory for Physical Sciences at Microscale, Department of Physics, University of Science and Technology of China, Hefei, Anhui 230026, Republic of China
 - b) Department of Astronomy and Applied Physics, University of Science and Technology of China, Hefei, Anhui 230026, Republic of China
- [1] K. Salma, Z.J. Ding, Z.M. Zhang, P. Zhang, K. Tókési, D. Varga, J. Tóth, *Surface Science* 603 (2009) 1236.

4.4 Identification of hydrogen and deuterium at the surface of water ice by reflection electron energy loss spectroscopy

F. Yubero^{a)}, K. Tórkési

The study of elastically backscattered electrons from surfaces by reflection electron energy loss spectroscopy (REELS) has been recently recommended as an alternative technique to quantify the *H* content at the surface of a-C:H and polymer samples [1-3]. This analysis is based on the fact that the energy loss of the incident electrons due to the recoil effect depends on the atomic mass of the particular atom present at the surface. The observed difference in recoil energies between H and O atoms (about 2 eV for 1.5 keV primary electrons) can be easily measured with standard electron spectrometers used in surface analysis.

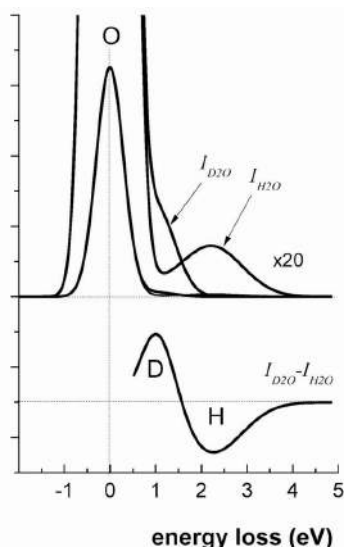


Figure 1. Above: MC simulations corresponding to 1500 eV backscattered electrons from H_2O and D_2O surfaces (primary energy 1500 eV, $\theta = 120^\circ$). Below: Corresponding difference spectrum $I_{D_2O} - I_{H_2O}$. The signals coming from H, D, and O atoms are indicated.

In this paper we go one step forward to explore if, with the same experimental approach, it is possible to differentiate between hydrogen and deuterium (D) in the surface region of a sample. This capability could be important for technological fields such as surface func-

tionalization, where it is desired to distinguish between H and D at surfaces after interaction with labeled compounds. We have chosen normal and deuterated water as test labeled compounds because this polar molecule is of key importance in numerous surface reactions.

It has been shown that H and D can be easily distinguished at the surface of water ice [4] using standard REELS measurements with 1000 - 1650 eV primary-electron energies, i.e., a surface analytical technique. Differences in recoil energies of the O - H and O - D atom pairs present in H_2O and D_2O have been found to agree with MC simulations (see Fig.1). There are many possible applications of H and D detection by REELS. Among many others, this study opens the possibility of nondestructive studies of deuterium-labeled atoms present or adsorbed on surfaces. For example, studies of H incorporation into a polymer or carbon-based surface after plasma activation with gas mixtures with several labeled molecules containing H atoms.

Acknowledgements

F.Y. thanks the Spanish Ministry of Science and Education (Project CONSOLIDER - INGENIO CDS2008-0023, FUNCOAT) for financial support. K.T. was supported by the grant Bolyai from the Hungarian Academy of Sciences.

a) Instituto de Ciencia de Materiales de Sevilla, CSIC - U. Sevilla, C/Américo Vespucio 49, E-41092 Sevilla, Spain

- [1] F. Yubero, V. J. Rico, J. P. Espinós, J. Cotrino, and A. R. González-Elipe, *Appl. Phys. Lett.* **87**, 084101 (2005).
- [2] D. Varga, K. Tórkési, Z. Berényi, J. Tóth, and L. Kövér, *Surf. Interface Anal.* **38**, 544 (2006).
- [3] V. J. Rico, F. Yubero, J. P. Espinós, J. Cotrino, A. R. González-Elipe, D. Garg, and S. Henry, *Diamond Relat. Mater.* **16**, 107 (2007).
- [4] F. Yubero, K. Tórkési, *Appl. Phys. Lett.* **95**, 084101 (2009).

4.5 Electroless nickel plating with different pre-treatments on silicon carbide particles

J. Pázmán^{a)}, V. Mádai^{b)}, J. Tóth, Z. Gácsi^{a)}

The quality of interface between the reinforcing phase and the metallic matrix plays a very important role during the production of Al/SiC composites by means of powder metallurgy. A transient layer, a plating shall be developed on the reinforcing particles in order to form a better mechanical contact between the ceramic particles and the metallic matrix. Owing to the inert surface of silicon carbide, the metallic layer can be formed by a chemical reduction only in case if a surface-activation is carried out. Different types of pre-treating materials were tried out in order to do this procedure. A partial activation can be obtained after the pre-treatment by using Naphosphite and lactic acid [1] and therefore the desired plating is not continuous. A compact layer of silica formed at the surface of the ceramic particles in the course of surface oxidation by which a compact plating can be developed in case of a stable chemical Ni-bath. The development of continuous plating is promoted by the formation of metallic palladium nuclei in the course of using the two-step activation by palladium-chloride. The developed pre-treating layers were studied by a home-built XPS equipment (some details of the equipment can be found in refs [2], [3], [4]) and XRD method and the final coating layers developed by the plating process was studied by SEM.

Acknowledgements

One of the authors J.T. is indebted for the support of the Hungarian Science Foundation OTKA: (No K67873).

- a) Institute of Materials Science, University of Miskolc, H-3515 Miskolc-Egyetemváros, Hungary
- b) Department of Minerology and Petrology, University of Miskolc, H-3515 Miskolc-Egyetemváros, Hungary

NOTE: the paper was presented at EURO PM 2009, 12-14th October, Copenhagen, in the Technical Sessions No 24: PM Functional Materials. *PM means: Powder Metallurgy.*

- [1] D. Takács, L. Sziráki, T. I. Török, J. Sólyom, Z. Gácsi, K. Gál-Solymos: *Surface and Coatings Technology*, **201** (8) (2007) 4526-4535
- [2] L. Kövér, D. Varga, I. Cserny, J. Tóth and K. Tőkési, *Surface and Interface Analysis* **19** (1992) pp. 9
- [3] J. Végh: ECASIA-95. 6th Eur. Conf. on Appl. of Surf. Interface Anal., Montreux, Switzerland, October 9-13, 1995. eds: H. J. Mathieu, B. Reihl, D. Briggs. Chichester, etc, John Wiley and Sons (1996) p. 679-682
- [4] J. Tóth, Gy. Molnár., D. Varga, I. Cserny, L. Kövér, J. Kiss, I. Gál, A. Nagy, A. Domonyi, Zs. Kertész, J. Mosolygó[†], G. Tarr, G. Pető, I. Szabó, Y. Ould-Metidji, B. Gruzza, L. Bideux, V. Matolin, A. Sulyok, M. Menyhárd: (TU-P-TDE 07. Book of abstr.: p. 293). 9th Eur. Conf. on Appl. of Surf. and Interface Anal. (ECASIA-2001), Avignon, France, 30 Sept. - 5 Oct., 2001

4.6 An experimental study on the effect of aqueous hypophosphite pre-treatment used on an Al-alloy substrate before electroless Ni plating

G. Szirmai^{a)}, J. Tóth, T.I. Török^{a)}, N. Hegmann^{b)}

A new surface pre-treatment method is under development for electroless nickel plating, which appears to be an effective and environmentally benign treatment for the following deposition of a sound and high quality surface nickel coating with good adhesion. The aluminium substrate is immersed in a mildly acidic solution (lactic acid) of sodium hypophosphite in order to modify the passive surface and make it suitable for the reductive chemical precipitation of the nickel-phosphorus nuclei from the electroless nickel plating bath [1]. During this novel pre-treatment procedure the surface adsorption of the hypophosphite anions might play an important role, therefore, several advanced surface testing and analytical techniques (SEM-EPMA-EDXRS, TEM, XPS) were applied in order to monitor and characterize the surface reactions and adsorption phenomena taking place during the pre-treatment. For the XPS study a home built XPS machine was applied [2], [3], [4]. The Al excited XPS (studying P 2s, P 2p, O 1s, C 1s, Al 2p, Ni 2p photoelectron lines) proved to be one of the most powerful techniques in the identification of the chemical species formed and present on the surfaces examined in this study.

Acknowledgements

One of the authors J.T. is indebted for the support of the Hungarian Science Foundation OTKA: (No K67873).

a) University of Miskolc Department of Metallurgical and Foundry Engineering, H-3515, Miskolc-Egyetemváros, Hungary

b) BAY-NANO Institute for Nanotechnology, H-3515 Miskolc-Egyetemváros Pf. 46, Hungary

Notes:

1. The paper was presented at the 7th Hungarian National Materials Science Conference (OATK-2009) 11-13 Oct 2009, Balatonkenese, Hungary.
2. The paper was the winner in the competition for the best poster presentation. See: <http://www.atomki.hu/newsann-hu.html#oatk>

[1] D. Takács, L. Sziráki, T. I. Török, J. Sólyom, Z. Gácsi, K. Gál-Solymos: *Surface and Coatings Technology*, **201**(8) (2007) 4526-4535

[2] J. Végh: ECASIA-95. 6th Eur. Conf. on Appl. of Surf. Interface Anal., Montreux, Switzerland, October 9-13, 1995. eds: H. J. Mathieu, B. Reihl, D. Briggs. Chichester, etc, John Wiley and Sons (1996) p. 679-682

[3] J. Tóth, Gy. Molnár., D. Varga, I. Cserny, L. Kövér, J. Kiss, I. Gál, A. Nagy, A. Domonyi, Zs. Kertész, J. Mosolygó[†], G. Tarr, G. Pető, I. Szabó, Y. Ould-Metidji, B. Gruzza, L. Bideux, V. Matolin, A. Sulyok, M. Menyhárd: (TU-P-TDE 07. Book of abstr.: p. 293). 9th Eur. Conf. on Appl. of Surf. and Interface Anal. (ECASIA-2001), Avignon, France, 30 Sept. - 5 Oct., 2001

[4] L. Kövér, D. Varga, I. Cserny, J. Tóth and K. Tőkési, *Surface and Interface Analysis* **19** (1992) pp. 9

4.7 On the composition depth profile of electrodeposited Fe-Co-Ni alloys

L. Péter^{a)}, A. Csik, K. Vad, E. Tóth-Kádár^{a)}, Gy. Molnár^{b)}

The production of magnetic materials with high saturation induction and low coercive field is a key issue for the development of magnetic data storage devices. Fe-Co-Ni alloys have also been intensively studied because these ternary alloys can show higher saturation induction and lower coercive field than the binary magnetic alloys. Electrodeposition of high-moment magnetic materials is a viable alternative of the physical production methods due to the flexibility of electrodeposition in the sense that patterned surfaces can be covered with an alloy of predefined composition at low cost.

Several recent studies have dealt with the optimization of the electrodeposition of Fe-Co-Ni alloys with respect to various target parameters. Low coercivity and high saturation induction were of prime importance, while other magnetic properties such as anisotropy, high-frequency permeability and magnetoimpedance properties were also examined.

Studies of electrodeposited Fe-Co-Ni alloys revealed that alloys in which the content of the major component exceeds about 70 wt. % adopt the equilibrium crystal structure of the majority components (bcc for Fe, hcp for Co and fcc for Ni). The structure of electrodeposited Fe-Co-Ni alloys was found to be a function of the deposit thickness, and this function was not restricted to the usual thickness dependence of the grain size but also included the variation of the phase ratio.

In this work the depth profile analysis of electrodeposited Fe-Co-Ni alloys was presented by Secondary Neutral Mass Spectrometry (SNMS) with the reverse depth profile technique. In this method, the deposit was covered with some separator and supporting layers (for Fe-Co-Ni samples, these were Zn and Ni, respectively). Then, the deposit was detached from the substrate and a very smooth initial surface was provided for the depth profile analysis, which made it possible to detect very fine composition changes close to the

substrate. The reverse depth profile analysis of electrodeposited Fe-Co-Ni samples indicated that various zones were formed close to the substrate due to the interplay of the anomalous nature of the codeposition of Fe, Co and Ni with the depletion of the electrolyte for the ions of the magnetic elements. A spontaneous near-substrate composition modulation was found for each sample studied. The initial deposit is very rich in Fe, which decays due to the depletion of the electrolyte in the vicinity of the cathode surface. The near-substrate modulation pattern can be elucidated by taking into account the mutual deposition preference of the iron-group metals and the mass transport of the ions in the solution. The composition fluctuations of Fe and Co at distances larger than 100 nm from the substrate are strictly correlated. Composition fluctuations beyond the near-substrate zone are attributed to the dependence of the hydrogen evolution rate on the Ni content of the surface and the convective effect of the hydrogen evolved.

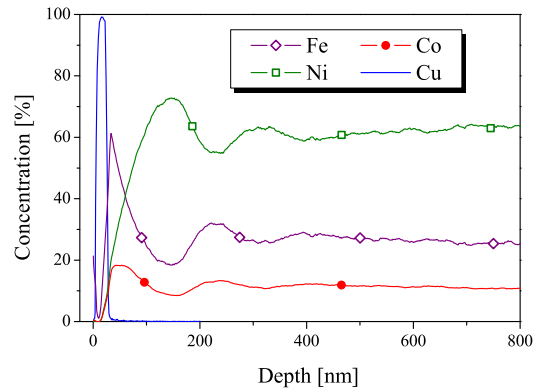


Figure 1. Reverse depth profile of electrodeposited Fe-Co-Ni layer.

- a) Research Institute for Solid State Physics and Optics, Hungarian Academy of Sciences 1525 Budapest, P.O. Box 49, Hungary,
- b) Research Institute for Technical Physics and Materials Science, Hungarian Academy of Sciences 1525 Budapest, P.O. Box 49, Hungary

4.8 Energy dependence of electron transmission through a single glass macrocapillary

B.S. Dassanayake^{a)}, R.J. Berezky, S. Das^{a)}, K. Tókési, J.A. Tanis^{a)}

Transmission and guiding of highly charged ions through various types of insulating nanocapillaries has been the focal point of many experimental and theoretical works. Guiding of slow highly charged ions through a single glass macrocapillary has been also studied, showing that guiding occurs even for macroscopic dimensions [1]. As a new aspect, the transmission of electrons through nanocapillaries was also investigated both experimentally and theoretically [2,3]. According to the recent theory and the previous measurements we expect a difference between the electron and ion guiding effect.

Therefore in our present work we investigated the transmission of 300 - 1000 eV electrons through a single, cylindrically-shaped glass capillary of macroscopic dimension with large aspect ratio of about 80. The capillary was produced in the Institute of Nuclear Research of the Hungarian Academy of Sciences, (ATOMKI). The measurements were performed in the accelerator laboratory at Western Michigan University in Kalamazoo.

We showed that electrons can be transmitted through a single glass capillary up to 6° tilt angle for all electron energies and the transmission decreases with tilt angle. Electrons transmitted through the capillary were found to lose energy, likely due to inelastic scattering with the inner surface while traversing the capillary tube.

To understand the transmission characteristics, the natural logarithm of the maximum peak height of the Gaussian fit to the angular distribution for each capillary tilt angle at each energy was plotted against the respective tilt angle as shown in Fig. 1. The transmitted intensities were found to reveal two distinct regions, as expected, which have very different transmission characteristics. For tilt angles $\Psi < 2.5^\circ$ the transmission falls off with a steeper slope than in the second region for $\Psi > 2.5^\circ$. Geometrical calculations, including the beam

divergence, indicate that the fall off for $\Psi < 2.5^\circ$ is due to the direct transmission of electrons through the capillary. Surprisingly, the guiding angle increased with increasing energy in the indirect region, contrary to previous results for slow positive ions and for fast electrons.

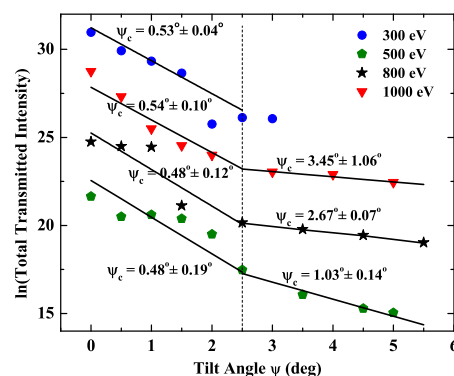


Figure 1. Natural logarithmic plots of the maximum peak heights of the Gaussian fits to the angular distributions. Intensities for 300, 800 and 1000 eV have been shifted by +7, +3, and +6, respectively, along the vertical axis for ease of visualization. Values for $\Psi < 2.5^\circ$ represent the direct transmission region of electrons, and values for $\Psi > 2.5^\circ$ the indirect transmission region. The Ψ_c values show the characteristic guiding angles of the capillary, defined as the tilt angle for which the transmitted intensity falls to 1/e of its value at $\Psi = 0^\circ$.

Acknowledgements

This research was supported by an award from Research Corporation.

- a) Department of Physics, Western Michigan University, Kalamazoo, USA
- [1] R.J. Berezky, G. Kowarik, F. Aumayr and K. Tókési, NIM B267 317 (2009).
- [2] S. Das, B.S. Dassanayake, M. Winkworth, J.L. Baran, N. Stolterfoht and J.A. Tanis, Phys. Rev. A76, 042716 (2007).
- [3] K. Schiessl, K. Tókési, B. Solleder, C. Lemell and J. Burgdörfer, Phys Rev. Lett. 102, 163201 (2009).

4.9 Heatable sample holder for capillary experiments

R.J. Berezky, G. Kowarik^{a)}, A. Macé^{a)}, F. Aumayr^{a)}, K. Tókési

The transmission of charged particles through various types of capillaries has been recently in the center of interest. The observed ion guiding phenomenon offered new possibilities for fundamental investigations, characterization of the inner walls of the insulating tube and also holds various possible applications.

Thereafter an intensive experimental investigation started to understand the basic properties of the guiding for ions using several insulating materials like PET, SiO₂, and Al₂O₃.

Another viewpoint of the experiments was how the guiding effect changes with the length or with the inner diameter of the capillary. Recently guiding of slow highly charged ions through a single glass macrocapillary has been studied, showing that guiding occurs even for macroscopic dimensions [1].

As a completely new aspect we would like to measure the temperature dependence of the ion-guiding. The investigation of the temperature dependence of the guiding gives new possibilities both for a fundamental understanding of the guiding phenomenon and applications. The guiding maybe adjustable by changing the temperature of the capillary, namely it may improve the efficiency of the guiding power. In our future experiments we try to find the answer how the ion guiding ability of an insulating capillary changes as a function of temperature.

For these experiments a completely new heatable sample holder was designed (see Fig. 1). Our preliminary results shows that the ion guiding ability of the capillary strongly decreases, when the temperature of the glass is raised from 20°C (room temperature) to 80°C.

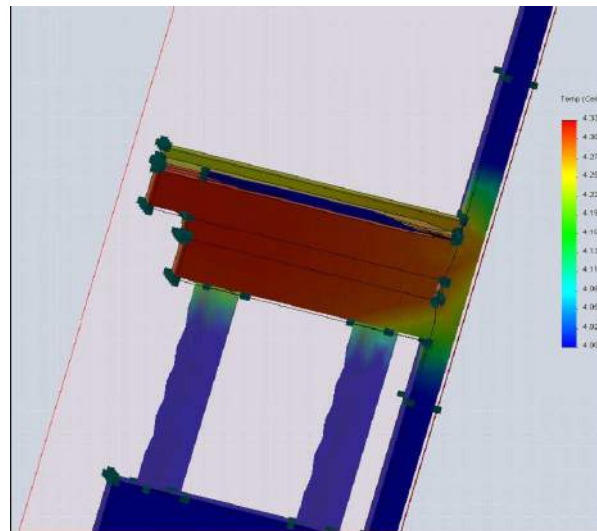


Figure 1. Simulation of the temperature of the heated sample holder.

Acknowledgements

The financial support received from the ITS-LEIF Project (RII3 026015) is gratefully acknowledged. This work was supported by the “Stiftung Aktion Österreich-Ungarn”, the grant “Bolyai” from the Hungarian Academy of Sciences, the TeT Grant no. AT-7/2007, the Hungarian National Office for Research and Technology, as well as Austrian FWP (P17499), and the Hungarian Scientific Research Found OTKA (K72172). We also thank to Mr. Ferenc Turi for the technical support.

a) Institut für Angewandte Physik, Technische Universität Wien.

[1] R.J. Berezky, G. Kowarik, F. Aumayr and K. Tókési, NIM B267 317 (2009).

4.10 Search for collective excitations in nanoparticles of biological origin

T. Papp, M. Hunyadi, Z. Gácsi, J. Tóth, D. Varga

Nanoparticles of biological origin are abundant in nature. One might even consider searching for them in extraterrestrial objects as a remnant of life, and a fingerprint of the existence of primitive life forms billions of years ago. It is also intriguing to consider the potentiality that some of the bacteria use very scarcely available elements for the internal (detoxication) and external (dissimilatory reduction) production of nanocrystals, for example like Te(0). Developing a breathing process based on a rare earth element, certainly is a stretch on the evolution idea. Turning the reasoning around, one can speculate that such primitive life forms have evolved in a very different environment, where the base elements of their make up were abundant, which is not the case on Earth. The late Prof. Terry Beveridge of University of Guelph, ON, Canada raised the idea on a speculative level, that such a characteristic biosignature imposed on a trace element like selenium may conceivably be useful in the search for evidence of extinct microbial communities in sedimentary deposits of extraterrestrial origin (i.e., Mars) [1].

These are challenging ideas, but there are potentially imminent benefits of using microorganisms to mass produce nanoparticles. Currently there is technical interest in tellurium with the aim of developing solar cells that have high efficiency to convert sunlight into electrical current. We are involved in photovoltaic technology research, and are developing CdTe detectors for X-ray detection [2]. We have recently observed giant resonances in scintillators [3], and with doping the CdTe could be turned into PET (Positron Emission Tomography) detector material [4]. Therefore

we have interest in the electro-optical properties of Te and Se. Our study of collective excitations and giant resonances in X-ray and nuclear radiation detectors has initiated new models and approaches in detector research. It is well established that giant resonances are also supported by nanostructures. Therefore, as a first step our direction is to search for such phenomena in biological matter. We have chosen the Se nanoparticles produced by lactic acid bacteria. The microbial diversity of Se-respiring prokaryotes is very broad and includes hyperthermophiles capable of respiring Se oxyanions at 90°C. There is a profound geometric and spectral variations between Te(0) and Se(0) nanoparticles formed by prokaryotes that respire oxyanions of these elements. Lower bandgap energy was noted for the Te(0) nanorods produced by them, suggesting the greater ease with which this material can serve to convert radiant electromagnetic energy into electrical current than the referenced commercially obtained samples.

Using XPS and REELS we have studied the electron transport properties of Se nanospheres, produced by various strains of lactic acid bacteria. The first obstacles that we have to overcome are sample preparation and characterization, as bacteria can produce profound variations on nanospheres and nanorods.

- [1] R.S. Oremland et al., *Appl. Environ. Microbiol.* 70 (2004) 52
- [2] T. Papp, et al., *ATOMKI Ann. Rep.* 2008, (2009) paper 8.10
- [3] T. Papp, et al., *ATOMKI Ann. Rep.* 2009, (2010) paper 7.8
- [4] A. Kastalsky et al., *Nucl. Instrum. and Methods A* 565 (2006) 650

5.1 Radiocarbon dating of the last volcanic eruption of the Ciomadul volcano, Southeast Carpathians

M. Molnár^{a,c}, I. Futó^a, L. Rinyu^a, Sz. Harangi^b, A.J.T. Jull^c

The last volcanic eruption in the Carpathian-Pannonian Region occurred within the Ciomadul volcano, Southeast Carpathians. It is a lava dome complex active for about 900 ka. Following the effusive activity, at least two major explosive volcanic eruptions occurred forming two craters (Mohos and St. Anna). These eruptions resulted in pumiceous pyroclastic fall and flow deposits. In order to understand the behavior of this volcano and evaluate the possible renewal of the volcanic eruption, it is crucial to constrain the length of the active and repose periods and know the date of the last eruption.

The former K/Ar and radiocarbon data are controversial and give only a rough estimate for the active phases. The age data for the last eruption is in the range from 10000 and 40000. In this study, we focus on the time of the last volcanic eruptions. We analyzed charcoal fragments found in pumiceous pyroclastic flow deposits from two localities.

C-14 dating from the first locality (Bx) was executed by GPC technique in the ATOMKI, and the following five dating (one repeated dating of the ATOMKI sample, with excellent match; one resampled charcoal from the first locality, and one sample from a second locality (Tf), and dating of NaOH-soluble fractions coming from sample prep for all the three charcoal samples) in NSF Lab in Tucson, AZ by AMS technique.

The new radiocarbon data provided valu-

able information on the behaviour of the Ciomadul volcano and help to constrain the time of the last eruption of the volcano. The main conclusions are the following:

1. The last volcanic eruption occurred at about 27000 BP.
2. The product of the youngest eruption is exposed at the southern margin of the volcano (Bx locality) and not at west (Tf locality) as was previously thought.
3. A striking new result is that there were at least two major explosive eruptions, not a single one, related to the formation of the St. Anna crater. The youngest one followed another subplinian eruption after about 10 ka quiescence period.
4. Further dating for the time of the older eruptions is crucial to understand the nature of the volcano and to evaluate the characteristic repose time of Ciomadul.

These data are consistent with the different composition of the volcanic products from the two localities.

Acknowledgements

This study is part of the research project supported by the OTKA grant K68587.

- a) Hertelendi Ede Laboratory of Environmental Studies, MTA ATOMKI, Debrecen, Hungary
- b) Department of Petrology and Geochemistry, Eötvös University, Budapest, Hungary
- c) NSF Arizona AMS Laboratory, University of Arizona, Tucson, AZ, USA

5.2 Atmospheric fossil fuel CO₂ record in Debrecen city during the winter of 2008

M. Molnár, L. Haszpra^{a)}, É. Svingor, I. Major^{b)}, I. Futó, L. Rinyu

Fossil fuel CO₂ content in the air of a major Hungarian city (Debrecen) was determined using together measurement of CO₂ mixing ratio and radiocarbon (¹⁴C) content of air.

In this project we developed a high precision atmospheric CO₂ monitoring station in Debrecen. An integrating sampling system (developed by ATOMKI) was applied for radiocarbon measurements. One sampler was installed in Debrecen station and two independent ¹⁴CO₂ sampling line were installed 300 km far from Debrecen at Hegyhátsál station as independent background references, where high precision atmospheric CO₂ mixing ratio measurement is also running since 1997.

During the winter of 2008/09 we measured the mixing ratio and radiocarbon content of atmospheric CO₂ at Debrecen and the reference station simultaneously. It was concluded that trends in CO₂ mixing ratio variations in time are very similar at the three different sampling points (3 m above ground in Debrecen, 10 m and 115 m above ground in Hegyhátsál). Air quality in Debrecen during September of 2008 seemed to be relatively clear from the point of

view of its CO₂ content at least. When winter came closer in October, with lower outside temperature and less sunshine hours the CO₂ content of air was increased in general at all the three sampling points, but this effect was more intensive closer to the ground level.

According our radiocarbon observations it was clearly indicated that there was not significant amount of fossil fuel CO₂ in the air of Debrecen during September in 2008. But during the winter of 2008/09 the $\Delta^{14}\text{C}$ value of atmospheric CO₂ of Debrecen decreased with more than 40 ‰ relative to September's results, and according our calculations it was caused by about 20 ppm fossil fuel CO₂ which appeared as a surplus amount in the air above the September level (Figure 1.).

Acknowledgements

This research project was supported by Hungarian NSF (Ref No. OTKA-F69029) and Isotoptech Zrt.

a) Hungarian Meteorological Service, Budapest, Hungary

b) University of Debrecen, Debrecen, Hungary

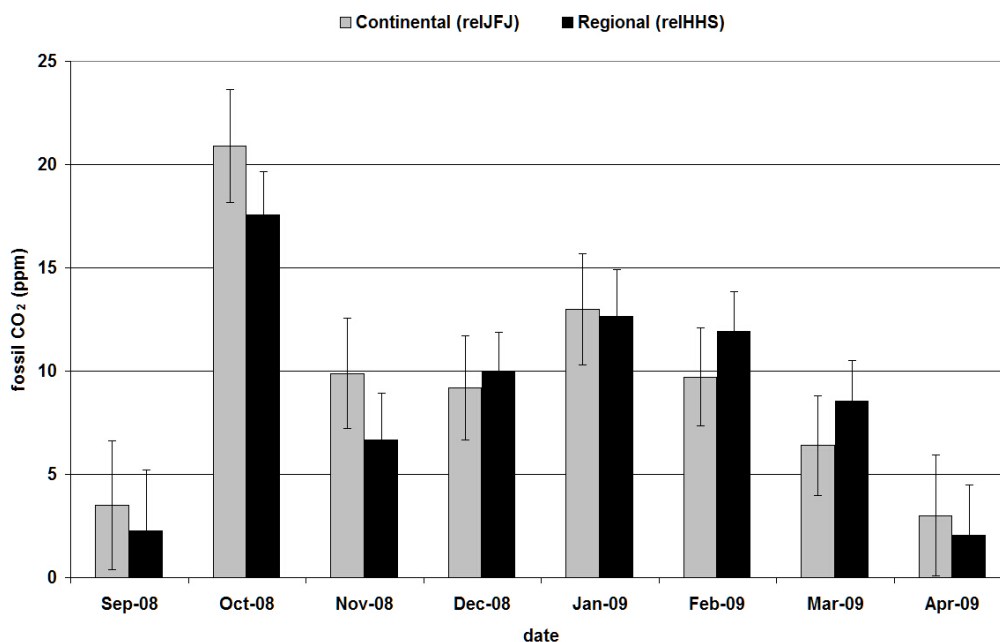


Figure 1. Regional and continental atmospheric fossil fuel CO₂ in the city of Debrecen during the winter of 2008.

5.3 Using an ultrapure ^4He spike in tritium measurements of water samples by the ^3He ingrowth method

L. Palcsu, Z. Major, Z. Köllő, L. Papp

Clarke et al. (1976) described a new method based on mass spectrometric measurement of ^3He to determine low level tritium concentrations of water samples [1]. The method consists of three major steps: 1) The water samples are put into glass bulbs. The dissolved gases including helium are removed from the water by vacuum pumping. 2) The sample are stored for several months or years so that ^3He atoms are produced from tritium decay. 3) The amount of the tritiogenic ^3He is measured mass spectrometrically.

Since then numerous laboratories adopted this method as noble gas mass spectrometers became commercially available. The measurements are usually calibrated by means of well known air aliquots, which in size can be compared to the helium amount from the tritium sample.

The $^3\text{He}/^4\text{He}$ ratio of samples can differ considerably from that of air used for standardization. For this reason it has to be kept in mind that a possible discrimination of ^3He by ^4He is not necessarily corrected by the air standards. Additionally, the mass spectrometric sensitivities of the different helium isotopes depend on the pressure at the ion source. In case of tritium measurements, the overall pressure of the helium in the mass spectrometer is much lower than that of the helium from the air calibration.

We use air aliquots that contain $7\cdot 10^{-9}$ to $2\cdot 10^{-7}$ ccSTP of ^4He and $5\cdot 10^{-15}$ to $1.5\cdot 10^{-13}$ ccSTP of ^3He . The relative standard deviations of the calibration measurements vary between 1-2 %, and the non-linearity effect is always taken into account. The overall helium amount in the mass spectrometer in case of a tritium sample is usually less than $3\cdot 10^{-10}$ ccSTP that derives, of course, from the ^4He . As the amount of the calibration sample converges to that of tritium samples, we lose the good statistical error of the ^3He measurement being counted by an electro-multiplier.

It seems that the large difference of the helium pressure in the ion source between a sample and the calibration makes a different ionization efficiency for the tritiogenic ^3He . In our case, even if the air calibration seems to be good, this pressure-dependent effect caused a changing systematic error of 10 to 40 % for the standard water samples of known tritium concentration.

Within a short period of a few weeks, the systematic difference between the expected and measured values of standard samples of known tritium concentration was quite stable allowing us to use a correction factor, that was usually used to correct the measured values of a sample. To solve this problem, we have decided to increase the helium pressure in the ion source for a tritium sample by adding an ultrapure ^4He spike to each tritium sample during the inlet. We built a reservoir of 6230 cm^3 that was filled with ^4He at about $1\cdot 10^{-5}$ mbar, and CO_2 at 1030 mbar. Pipetting aliquots from this spike reservoir we can prepare ^4He samples of $7.6\cdot 10^{-8}$ ccSTP that is always added to the tritium samples. Hence the helium pressures are always within the same order of magnitude. This ultrapure ^4He was prepared by Yoshiki et al. [2] using a superleak made of compacted aluminium oxide nano powder of 200 to 500 Å. Liquid helium of 1.5 K was let through this superleak. The superfluid component, that composed of solely ^4He bosons passed easily the superleak while the non-superfluid and gas components were retained.

Our measurements confirmed that this helium hardly contained any ^3He : the measured $^3\text{He}/^4\text{He}$ isotope ratio is lower than $5\cdot 10^{-10}$, that is extremely perfect for our purpose. Since we use this isotope dilution technique, namely the ^4He spiking, the standard measurement became very precise: the measured values are within 2.3 % around the expected values (see Fig).

The significance of this new method is be-

yond the tritium measurements. In all cases of helium measurements where precise helium isotope ratio measurements is needed, but the pressures are different, the ^4He isotope dilution

can be a way.

[1] W.B. Clarke, et al., (1976) *Int. J. Appl. Rad. Isot.* 27, 515-522.

[2] H. Yoshiki, et al., (2005) *Cryogenics*, 45, 399-403.

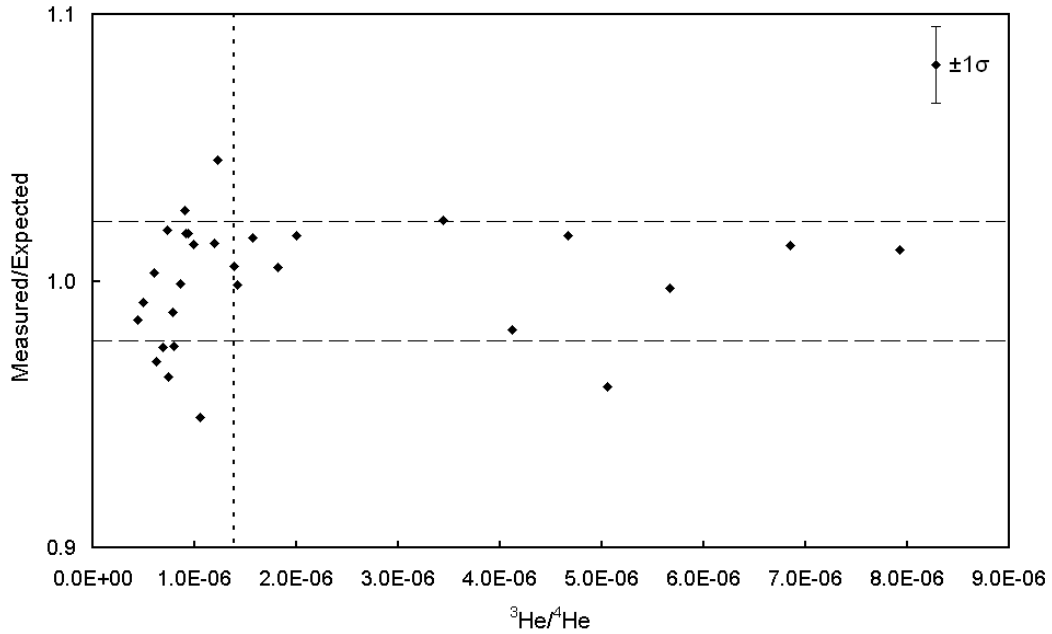


Figure 1. The ratios of measured and expected tritium concentrations as a function of the measured $^3\text{He}/^4\text{He}$ isotope ratio. The points are scattered around the value of 1.000 (more precisely, 1.000092) with a 1σ standard deviation of 0.023. The two horizontal dashed lines represent the $\pm 1\sigma$ values around the mean. The perpendicular line represents the atmospheric isotope ratio of $1.384 \cdot 10^{-6}$.

5.4 Separation of ^{79}Se from L/ILW radioactive waste material produced by the Hungarian NPP

Á. Bihari, M. Mogyorósi, Z. Szűcs, and B. Kovács^{a)}

Selenium-79 is a beta emitter produced by the fission of ^{235}U . It is one of the radionuclides of interest in the management of nuclear waste repositories because of its long half life (2.95×10^5 y) and its potential migration ability from the repository to the environment [1]. Typical global activity of low- and intermediate level (L/ILW) liquid wastes as well as spent ion exchange resins of Paks NPP meant to deposition is in the range of $10^5 - 10^7$ Bq L⁻¹ and $10^6 - 10^9$ Bq kg⁻¹, respectively. Measurement of ^{79}Se is particularly difficult due to its low activity (about 10^{-3} Bq L⁻¹ and 10^{-1} Bq kg⁻¹, resp.) in such waste matrixes. One of the main difficulty of the development of a separation procedure is that ^{79}Se is not available as a standard either in liquid or solid form. As a consequence, a “step by step” methodology was implemented to achieve the validation of the protocol where stable Se and ^{75}Se (gamma emitter) were used as carrier and tracer to estimate the chemical yields of the different steps.

The estimated chemical form of selenium in the samples is selenite (Se(IV)) due to strongly basic matrix. This way we expected that it must be concentrated on anion exchange as well as mixed bed resins while cation exchange resin does not adsorb it. This theory has been tested on the resins using the stable selenite as carrier. The concentrations of selenium

were measured by ICP-OES. The spent anion ion exchange resin samples already contained ^{75}Se therefore the measurement of the chemical yields was made by this way too. The resin samples were washed with 100 times resin bed volume of 10 w% NaNO₃ solution. The Se content of the resulting elutes proved our theory. However, they also contained various contaminants depending on the original sample. The ratios of the separation for the other radioisotopes (e.g. ^{54}Mn , ^{60}Co , ^{106}Ru , ^{125}Sb , ^{137}Cs , etc.) were also carried out by the measurement of their activity in each steps of the procedure.

The elutes were transferred in to 1:1 HCl matrix and selenite was reduced to elemental selenium by H₂S. The precipitated Se was filtered and was additionally cleaned by digeration in hot 1:1 HCl solution. After the required number of cleaning cycles, the selenium precipitate can be measured with liquid scintillation counting if ^{79}Se standard reference material is available. The initial isotopic composition of an anion exchange resin sample as well as the final separated sample is shown in Table 1.

a) Institute of Food Science, Quality Assurance and Microbiology Centre for Agricultural Sciences and Engineering, University of Debrecen

[1] F. Seby, M. Potin-Gautier, E. Giffaut, O.F.X. Donard, *Analisis* 26 (1998) 193.

Table 1. Isotopic composition of sample 132AER2009 at the beginning and at the end of the cleaning procedure.

Isotope	Initial values* (Bq)	Final values* (Bq)
^{124}Sb	266±8	<2.41
^{125}Sb	114±2	<0.34
^{137}Cs	13.4±0.5	<0.13
^{54}Mn	177±3	<0.22
^{60}Co	495±9	1.38±0.09
^{75}Se	54.7±1.5	22.6±0.5
^{108m}Ag	24.4±0.4	<0.09
^{110m}Ag	1041±5	<0.23

* Decay-corrected to 2009.03.20.

5.5 Improved determination of Tc-99 in L/ILW liquid wastes with special emphasis on quantitative Ag-108m separation

Á. Bihari, M. Mogyorósi, Z. Szűcs, I. Tóth^{a)}

The low- and intermediate-level liquid wastes produced by the Paks NPP contain routinely measureable gamma-emitting (e.g. ⁵⁴Mn, ⁶⁰Co, ^{110m}Ag, ¹²⁵Sb, ¹³⁴Cs and ¹³⁷Cs) as well as many so-called “difficult-to-measure” isotopes. Despite of their low specific activity compared to the total, the reliable determination of these isotopes is an important issue of nuclear waste management and environmental protection. The increasing amount of waste samples (with increasing number of isotopes in interest) to be qualified yearly by our laboratory put a pressure on revising the existing procedure of ⁹⁹Tc separation applied as well as to combine it with the separation of other isotopes wherever it is possible. One of the isotopes recently requested for determination is ^{108m}Ag.

The samples contain macro- and microscopic solid parts in small amounts. The solid to liquid ratio shows a very high variability among the samples. These particles are originated from the corrosion of the structural elements of the primary cycle and thus they contain isotopes like ⁵⁴Mn, ⁶⁰Co, ⁹⁵Zr, ^{110m}Ag, etc. in large specific activity. Some of these isotopes – such as that of manganese, silver and the members of the platinum group – are not soluble in the liquid phase of the samples allowing a quick and effective separation

of these from the matrix. This way, the specific activity of ^{108m}Ag (usually less than 10¹ Bq L⁻¹) can also be determined. In contrast, technetium attaches to these solid parts only in trace amounts as proved by spiking a sample with 50kBq ^{99m}Tc and after that filtering the solids from it (see columns 2-4 in Table 1).

Following the removal of the solids, BioRad®AG50W-X8 strongly acid cation exchange resin has been used to remove a large part of the radiocaesium content of the liquid phase (see columns 5-6 in Table 1). Since ^{99(m)}Tc is in the chemical form of pertechnate (TcO₄²⁻), it is not adsorbed on the resin. With the evaporation and subsequent dissolution of the effluent (in 1:1 HCl) one can remove the tritium (³H) and radiohalogenid (e.g. ³⁶Cl, ¹²⁹I) content of the sample. Technetium is reduced to Tc₂S₇ (solid) with H₂S in the presence of a substitute carrier (K₂ReO₄). After separation (filtering), technetium-heptasulfide is converted back to pertechnate form with H₂O₂. This step removes the majority of ⁶⁰Co, ¹²⁵Sb, ¹³⁴Cs, ¹³⁷Cs, etc. The remaining impurities are trapped on AG50W-X8 resin and ⁹⁹Tc is concentrated on Eichrom®Tc-TEVA selective resin.

a) ISOTOPTECH ZRt., Debrecen, P.O.Box. 360, H-4001, Hungary

Table 1. Isotopic composition of sample 212K2009 at various stages of the cleaning procedure.

Isotope	Initial values	Solid phase	Liquid phase	Adsorbed on resin	Effluent
¹²⁵ Sb*	58.7±3.8	< 3.67	59.8±1.8	< 27.4	60.1±0.4
¹³⁴ Cs*	5240±140	9.10±0.35	5170±30	2620±80	2510±20
¹³⁷ Cs*	32100±300	57.2±0.9	31400±500	15800±500	16200±300
⁵⁴ Mn*	397±19	362±5	< 2.81	< 4.30	< 0.79
⁵⁸ Co*	87.6±4.6	95.5±4.5	< 18.5	< 27.9	< 5.13
⁶⁰ Co*	5050±50	1210±20	3740±40	128±2	3600±30
^{108m} Ag*	< 7.55	1.85±0.18	< 1.49	< 2.89	< 0.40
^{110m} Ag*	585±20	570±3	< 4.75	< 6.83	< 1.37
^{99m} Tc**	~50	0.02±0.01	49.7±0.8	<0.01	50.9±0.9

* All values in Bq, decay-corrected to 2009.01.07.

** All values in kBq, decay-corrected to 2009.09.15. 18:20

5.6 Environmental survey of the low and intermediate level radioactive waste disposal facility Bábaapáti before the operation of the site

R. Janovics, Á. Bihari, Z. Major, M. Molnár, M. Mogyorósi, L. Palcsu, L. Papp, M. Veres^{a)}

The new Hungarian National Radioactive Waste Disposal Facility was established in the granite of the Mórág Block Mountains to store low and intermediate level radioactive waste originating from the Paks Nuclear Power Plant. The safe operation of the radioactive waste disposal facilities requires a long-term environmental monitoring to gain information about the radiation properties of the site together with the radiation exposure of the personnel and the environmental media. Before the start of the operation of the facility the environmental characteristics of the site and its vicinity, i.e. the so-called zero level was determined.

The determination of the zero level of the nuclear facilities is inevitable as the evaluation of the measurement data in the course of

the operation should be related mainly to this zero level. In the course of the measurements the monitoring of the environmental elements i.e. air, soil, water (springs, streams, precipitation), fall-out, wash-out, plant and animal samples was performed from several points of view. From the samples collected radiocarbon, tritium, strontium-90, gamma emitters, gross alpha, gross beta and field gamma measurements were carried out.

As the results reported show the state preceding the operation of the facility, they can approximately be considered as the Hungarian background data.

a) Isotoptech Co. Ltd., Debrecen, Hungary

5.7 Experimental investigation and numerical modelling of tritium wash-out by precipitation in the area of the nuclear power plant of Paks, Hungary

Z. Köllő, L. Palcsu, Z. Major, L. Papp, M. Molnár, T. Ranga^{a)}, P. Dombóvári^{a)}, L. Manga^{a)}

Tritium is an important radioactive isotope because its natural occurrence in the air and precipitation due to natural and artificial sources. In order to investigate the natural changes in tritium concentration, the artificial component has to be known.

Some field experiments were carried out before to investigate the washout of tritium by precipitation emitted from artificial sources, but none of them were carried out around a real power plant, measuring the deposition pattern. We collected rainwater around the nuclear power plant of Paks (Paks NPP), and analyzed them for tritium.

The rainwater samplers were constructed at ATOMKI. Their structure consists of a funnel, support parts and a long tube, acting as the storage vessel for the rainwater. One end of the tube is connected to the funnel, the other end is open. This way when "new" rainwater falls, it pushes out the "old" water, causing that always the last rainwater is in the tube (if enough rain is falling). In total 54 samplers were placed out around the Paks NPP in two half circles, with radiuses 400 and 800 m, pointing east.

We collected samples after a rain period on 7-8 June 2009. They were prepared and measured with liquid scintillation counting (LSC) for tritium. We measured some samples also with the ³He-ingrowth method, to ensure better accuracy.

The measurement results in Fig. 1 clearly show the trace of the tritium plume emitted from the plant. However, the highest values are not very high, compared to environmental levels, and considering the fact that all the samples were collected from the area of the plant.

A numerical model was coded to calculate the washout of tritium theoretically from the meteorological and emission data, and to estimate the effect of the plant in larger distances. In Fig. 1 it is apparent that the model, however does not describe the data precisely, but gives reasonable results, especially for the outer circle. The calculations also show that the tritium levels are comparable with the environmental ones over some kilometers of distance from the plant.

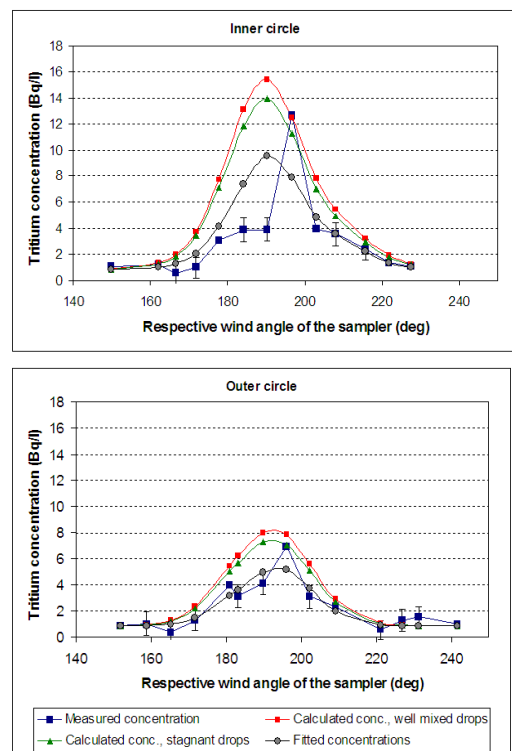


Figure 1. Measured and calculated tritium concentrations.

a) Paks Nuclear Power Plant, Paks, Hungary

5.8 Characterization of urban aerosol sources in Debrecen, Hungary

Zs. Kertész, T. Szoboszlai, A. Angyal, E. Dobos, I. Borbély-Kiss

Aerosol pollution represents significant health hazard in urban environments. Despite the fact that Debrecen has not a much stressed environment the city is highly exposed to aerosol pollution. In order to evaluate the impact of aerosol particles on health, the knowledge of the particle size distribution, chemical composition, sources, and their change in time and space is needed.

This work presents a source apportionment study of fine (particles with aerodynamic diameter less than $2.5 \mu\text{m}$) and coarse (particles with aerodynamic diameter between 2.5 and $10 \mu\text{m}$) particulate matter in Debrecen by following the evolution of the elemental components with hourly time resolution. The variation of the elemental concentrations, their periodicity, correlation with other elements and meteorological parameters were studied on samples collected in different seasons. Aerosol sources were determined using the positive matrix factorization (PMF) method.

Aerosol samples were collected in the garden of the ATOMKI with a 2-stage sequential streaker sampler manufactured by PIXE International, which collected the fine and coarse fraction separately with few hours' time resolution. Between October 2007 and January 2009 five 10-days long sampling campaigns were carried out.

The elemental composition was determined by Particle Induced X-ray emission (PIXE) for $Z \geq 13$, and the elemental carbon (BC) content was estimated with a smoke stain reflectometer.

Source apportionment was carried out with the PMF receptor model developed for aerosol source characterization, provided by US EPA. Mass of species apportioned to factor, percentage of species apportioned to factors and average factor contributions of the campaigns, of working days and weekends and within the days were calculated.

The PMF analysis resulted seven factors in the fine and seven factors in the coarse mode. The main sources of atmospheric aerosol in the city of Debrecen were traffic through direct emission and re-suspended soil dust, sulphates originating from combustion and regional background, domestic heating, agriculture, mixture of salts of different origins, and a yet unidentified source in the fine fraction enriched with Cl.

Other sources were also identified by detecting several emission episodes. These events often involved Cl and heavy metals, and the origin of most of them is still unclear.

In May 2008 a Saharan dust intrusion reached Europe. The Saharan influence was observed through the considerable increase in the concentration of Al, Si, Ca, Fe and Ti in the coarse size fraction on 20th of May, and through the characteristic elemental ratios of Ti/Fe and Ti/Ca on 21st - 24th May. These episodes, however they bear little significance from the point of view of aerosol impact in the city, serve as a basis to reach a better understanding of short and long range aerosol transport.

Results of this study were presented on the 7th International Conference on Air Quality Science and Application, the 19th International Conference on Ion Beam Analysis and the 9th Hungarian Aerosol Conference.

Acknowledgements

This work was supported by the Hungarian Research Fund OTKA and the EGT Norwegian Financial Mechanism Programme (contract no. NNF78829) and the EU co-funded Economic Competitiveness Operative Program (contract no. GVOP-3.2.1.-2004-04-0402/3.0).

- [1] Zs. Kertész, *et al.*, Acta Geologica Debrecina Landscape and Environment 2 (2009) 109.
- [2] Zs. Kertész, *et al.*, in press, Nucl. Instr. and Meth. B (2010) DOI:10.1016/j.nimb.2010.02.103

5.9 Study of Cl containing urban aerosol particles by ion beam analytical methods

A. Angyal, Zs. Kertész, Z. Szikszai, T. Szoboszlai

In the densely populated areas of Europe one of the most important environmental problems is aerosol pollution. Thus one of the main goals of atmospheric research is to determine aerosol sources. In order to identify the origin of the particles, the knowledge of the chemical composition and size distribution is demanded.

As a result of a source apportionment study, several sources of fine (particles with aerodynamic diameter $< 2.5 \mu\text{m}$) and coarse ($10 \mu\text{m} \geq$ aerodynamic diameter $\geq 2.5 \mu\text{m}$) urban particulate matter were identified in Debrecen, using the hourly evolution of the elemental components [1]. Sources characterized by high chlorine content were found in both size fractions, which gave significant contribution to the aerosol concentration in Debrecen. However, the origin of these particles could not be identified on the available information. In this work we give a more accurate characterization of the sources of coarse-mode Cl by using single particle analysis.

Aerosol samples with 2-3 hours time resolution were collected in the frame of sampling campaigns in the garden of ATOMKI between October 2007 and January 2009 [1].

The elemental composition (for $Z \geq 13$) was determined by Particle Induced X-ray Emission (PIXE). Single particle analysis of chosen samples was done on the ATOMKI Scanning Nuclear Microprobe Facility. Morphology, size and elemental composition for $Z \geq 6$ of around 1000 coarse mode particles were determined by Scanning Transmission Ion Microscopy, light-element PIXE and PIXE analytical methods. Hierarchical cluster analysis was performed on the data set to group the particles.

In order to determine the possible sources of Cl in the coarse mode, the correlation between Cl and other elements, which could be used as tracers of different sources, was examined. Cl showed very strong correlation with Na. However the Cl:Na ratio was found to be different for different episodes indicating dif-

ferent origin of these particles. Mg:Cl (sea-salt) and K:Cl (fertilizer) elemental ratios were also studied, and in few cases correlations were found between these elements too. In spring and summer 2008 the Na-Cl correlation was weaker, the Ca-Cl stronger than other times.

The hierarchical cluster analysis resulted in 11 groups. The analysis showed that the main origin of the Debrecen coarse mode aerosol was mineral dust. There were four groups which explained sources of Cl. One of these groups was rich in NaCl, KCl and P. The city is surrounded by agricultural areas and farmers use fertilizers containing these compounds. Thus this source was identified as agriculture through fertilizers. In the following group sea-salt was observed through significantly increased concentration of NaCl, MgCl, and Sr. The third group was responsible for 14 % of the particles, and was characteristic to winter. Thus this source was appointed to winter salting of streets. The fourth cluster with 13 % of the particles was rich in CaS (gypsum) and Ca-Cl correlation was high. This phenomenon could be explained by a construction near to the sampling place.

Single particle analysis by ion beam analytical methods proved to be a useful tool for source characterization of urban atmospheric aerosol through providing significant additional information about the origin and formation of Cl containing aerosol [2].

Acknowledgement

This work was supported by the Hungarian Research Fund OTKA and the EGT Norwegian Financial Mechanism Programme (contract no. NNF78829) and the EU co-funded Economic Competitiveness Operative Program (contract no. GVOP-3.2.1.-2004-04-0402/3.0).

- [1] Zs. Kertész, *et al.*, in press, Nucl. Instr. and Meth. B. (2010) DOI:10.1016/j.nimb.2010.02.103
- [2] A. Angyal, *et al.*, in press, Nucl. Instr. and Meth. B. (2010) DOI:10.1016/j.nimb.2010.02.090

6.1 ^{11}C -radioisotope study of methanol co-reaction with ethanol over Ni-MCM-41 silica-alumina and Ni-alumina

É. Sarkadi-Pribóczy, T. Tsoncheva^{a)}, N. Kumar^{b)}, Z. Kovács and D. Yu. Murzin^{b)}

The Ni modifies the properties of acidic alumina and light acidic MCM-41 silica-alumina supports [1]. The radioisotopic method is a suitable tool for distinction of the ^{11}C -radioisotopic methanol and its co-derivates from derivates of non-radioactive ethanol on these catalysts.

Experimental

The Ni/Al₂O₃ (5 wt % Ni) is commercially available while H-MCMN-41 (Si/Al=20) and Ni-ion-exchanged MCM-41 silica-alumina (5 wt % Ni) were prepared and characterized in previous works. Before catalysis the Ni/Al₂O₃ and Ni-MCM-41 were pre-reduced. The ^{11}C -methanol was formed by a radiochemical process from ^{11}C -carbon dioxide produced at cyclotron ($T_{1/2} = 20.4$ min). The mixture of equivalent volume of radioactive methanol and non-radioactive ethanol was introduced into glass tube micro-flow reactor at ambient temperature. After adsorption, the valves were closed and the catalyst was heated up to the required temperatures. The desorption rate of the remaining ^{11}C -derivatives on catalysts were continuously followed by radiodetectors and the derivatives of methanol with ethanol were analyzed by Radio/FID-gas chromatography (FID is coupled on-line with a radiodetector). The ethanol and its derivates were identified by FID while the ^{11}C -methanol and its co-derivates (with ethanol) were detected by both of FID and radiodetector.

Results

The ^{11}C -dimethyl ether was the common product of the single ^{11}C -methanol transformation on H-MCM-41, Ni-MCM-41 and Ni-Al₂O₃ at low temperature (200-280 °C) due to middle strong acid sites. At higher temperature (280-350 °C), the dimethyl ether and

hydrocarbons were the dominant products on H-MCM-41 while dimethyl ether selectivity decreased on Ni-alumina and Ni-MCM-41 in favor of methane. The selectivities of methanol to formaldehyde and methane were the highest on Ni-MCM-41.

During co-reaction of ^{11}C -methanol with non-radioactive ethanol, the ^{11}C -labeled co-ethers, namely ^{11}C -methyl ethyl ether, appears beside ^{11}C -dimethyl ether considerably on H-MCM-41 while slighter on Ni-alumina and Ni-MCM-41 in favor of methane. The ^{11}C -labeled carbon dioxide and formaldehyde were also radiodetected on Ni-alumina and Ni-MCM-41 silica-alumina between 240-350 °C but with variant ratios compared to single methanol transformation. The selectivities of non-radioactive ethanol to hydrocarbons as well as ^{11}C -methyl ethyl co-ether transformation to ^{11}C -hydrocarbons were different along H-MCM-41, Ni-MCM-41 and Ni-Al₂O₃. The ethanol formed to hydrocarbons on all of catalysts and acetaldehyde was also detected on Ni-Al₂O₃ and on Ni-MCM-41.

Conclusion

Methanol conversion over H-MCM-41, Ni-MCM-41 and Ni/Al₂O₃ could be significantly changed in the presence of ethanol as a co-reactant. At lower temperature, formation of methyl ethyl co-ether is observed, while with the temperature increase its conversion to methane and C₂-C₅ hydrocarbons becomes the main reaction pathway.

a) Institute of Organic Chemistry, Bulgarian Academy of Science, Sofia, Bulgaria

b) Laboratory of Industrial Chemistry, Åbo Akademi University, Åbo/Turku, Finland

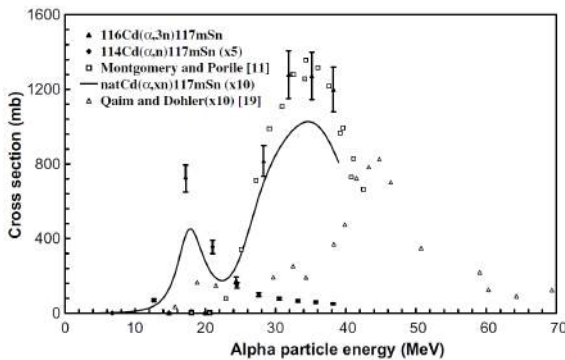
[1] É. Sarkadi-Pribóczy et al., *Cat. Lett.* **93**, 101(2004).

6.2 Production of ^{117m}Sn with high specific activity

Z. Szűcs, S. Takács, D. Jansen^{a)}, J.R. Zeevaart^{a)}, O.D. Maslov^{b)}, G.Ya. Starodub^{b)}, G.K. Vostokin^{b)}, M.V. Gustova^{b)}, V.N. Shvetsov^{c)}

Introduction

The production of ^{117m}Sn is commonly carried out by the $^{116}\text{Sn}(n,\gamma)^{117m}\text{Sn}$ or $^{117}\text{Sn}(n,n')^{117m}\text{Sn}$ nuclear reaction in nuclear reactor. However this method is unable produce ^{117m}Sn in high level of the specific activity, which is the basic requirement for application in nuclear medicine. An alternative way for the production would be the $^{116}\text{Cd}(\alpha,3n)^{117m}\text{Sn}$ nuclear reaction using a cyclotron. According to the literature [1] the cross section of this reaction is acceptably high, as can be seen in the following picture.



The thick target yield is $6\text{MBq}/\mu\text{Ah}$ and the activities of potential contaminating radioisotopes produced by side reaction are negligible, if the energy of the irradiating beam will be chosen precisely. The natural abundance of ^{116}Cd is 7,5%, it means that the price of the enriched material is reasonable [2]. A potential cyclotron facility with α -beam was found at JINR, Dubna, Russia where the radiochemical background also exist. This cyclotron facility is able to do routine irradiation with the necessary energy range (38-25 MeV) and beam intensity (at least $50\mu\text{A}$).

Experimental

The Cd-target was prepared as follows: the Cd-metal (22 mg) was dissolved in concentrated nitric acid and then evaporated to dryness producing $\text{Cd}(\text{NO}_3)_2$ salt. The $\text{Cd}(\text{NO}_3)_2$ salt was then re-dissolved in water, followed by the addition of a spatula tip of sugar and a few drops of methanol. The sugar allowed for adhesion of the salt to the target plate, and the methanol facilitated even wetting and hence homogeneous application of the Cd to the target surface. The target holder/plate comprised of a block of aluminium metal. The cadmium salt was then applied to the target holder painted across the surface.

Results and discussion

After irradiation the Cd-target material and the ^{117m}Sn product was stripped from the aluminium backing by washing with concentrated nitric acid. The solution was slightly evaporated, after that the salt was dissolved in HF acid. The ^{117m}Sn was then separated from the target material by anion exchange chromatography. The separation gave a chemical yield up to 90% and radiochemical purity 99.8%. The thick target yield of enriched $^{116}\text{Cd}(95\%)$ was found to be $173\text{ kBq}(\mu\text{A.h.mg})^{-1}$. It is therefore possible to produce sufficient quantities of “no carrier-added” ^{117m}Sn by the $^{116}\text{Cd}(\mu,3n)^{117m}\text{Sn}$ route, with as much as 0.5 Ci in a single batch (100 mg enriched ^{116}Cd , $10\mu\text{A}$ beam current, 100 hours irradiation).

a) NECSA, Division of R&D, South Africa

b) JINR, Flerov Laboratory, Dubna, Russia

c) JINR, Frank Laboratory, Dubna, Russia

[1] R.A. Rebeles, et.al, Nucl. Instr. and Meth. B 266 (2008) 4731

[2] isoflex@mail.transit.ru

6.3 Separation of ^{103}Pd from metal Rhodium by dry distillation

Z. Szűcs, S. Takács, J. Topkin^{a)}, J.R. Zeevaart^{b)}

Introduction

The use of Auger emitters as potential radiopharmaceuticals is increasingly investigated. One such radionuclide of interest is $^{103\text{m}}\text{Rh}$. This can be produced from ^{103}Ru or from ^{103}Pd in an in vivo generator. It has been proven on theoretical considerations that use of $^{103}\text{Pd}/^{103\text{m}}\text{Rh}$ in vivo generator will be successful in delivering $^{103\text{m}}\text{Rh}$ to a target site when complexed to a tumor selective carrier. ^{103}Pd is widely used in internal radiotherapy with one of the production routes via the irradiation of Rh by protons in a cyclotron. The charged particle production of ^{103}Pd is the only way for no-carrier -added production of this radionuclide, which is required for use in nuclear medicine. However, the widely used separation technique to get ^{103}Pd from the target material (as well as recovery of the Rh) by wet chemistry is a very complicated, labour intensive and expensive procedure, resulting in low yields of ^{103}Pd and high amounts of radioactive waste. An alternative more efficient separation and production technology can be developed based on differential evaporation. The principle is the following: The produced ^{103}Pd "contaminating" new element within the crystal structure of the Rh target can be forced to diffuse out from the deformed crystal lattice by heating up the target. In this process the ^{103}Pd accumulates on the surface of the target from where it can be evaporated. A prerequisite for this process is that the target metal (Rh) has a different partial pressure than the evaporated metal (Pd) [1].

The thick target yield is $6\text{MBq}/\mu\text{Ah}$ and the activities of potential contaminating radioisotopes produced by side reaction are negligible, if the energy of the irradiating beam will be chosen precisely. The natural abundance of

^{116}Cd is 7,5%, it means that the price of the enriched material is reasonable [2]. A potential cyclotron facility with α -beam was found at JINR, Dubna, Russia where the radiochemical background also exist. This cyclotron facility is able to do routine irradiation with the necessary energy range (38-25 MeV) and beam intensity (at least $50\ \mu\text{A}$).

Experimental and results

Irradiation of a stack of thin Rh foils was performed to determine the optimal irradiation parameters to avoid side nuclear reactions taking place simultaneously producing contaminating $^{101,101\text{m},102,102\text{m}}\text{Rh}$. radionuclides. After evaluating the gamma-spectra optimal parameters were determined during the second irradiation, producing pure ^{103}Pd . Two activated Rh foils were transferred to Necsa for further investigation of the separation process of ^{103}Pd . A series of experiments were carried out using high temperature and high vacuum condition. Separation of ^{103}Pd was demonstrated after keeping the irradiated Rh foil for 45 hours at $1190\ ^\circ\text{C}$ and 2×10^{-6} torr pressure.

Acknowledgements

The work was partly supported by the Hungarian TéT Bilateral Cooperation (OMFB-00138/2009) and by the South African NRF (UID 68768)

- a) Nuclear Energy Corporation of South Africa (Necsa), R&D, Radiochemistry, Pretoria, South Africa
- b) CARST, North West University - Mafikeng Campus, South Africa

[1] Z. Szűcs, J. Van Rooyen, J.R. Zeevaart. Recoil effects on β -decaying in vivo generators, interpreted for $^{103}\text{Pd}/^{103}\text{Rh}$. *Applied Radiation and Isotopes*, 2009, **67**, 1401-1404

[2] I.E. Alekseejev, *Radiochemistry* **45**, 2003, pp.429-456

6.4 Study of the sap-flow and related quantities of oak trees in field experiments

P. Kanalas^{a)}, I. Ander, A. Fenyvesi, V. Oláh^{a)}, E. Szöllősi^{a)}, I. Mészáros^{*,a)}

Climatology model calculations for the next decades in the Carpathian Basin predict more frequent occurrence of meteorological extremes and, especially, longer droughts with elevated average temperatures during the growing season. A drift of the transition zone between the wooden steppe and the forest regions is predicted [1], too, resulting in significant reduction and alteration of the climazonal forest communities in the mountainous regions. The aim of our project is obtaining information on the climatic sensitivity of the tree species in the sessile oak - Austrian oak forest stand of the Síkfőkút Project Long Term Ecological Research (LTER) area (Bükk Mountains, NE Hungary).

“Campaign-like” complex field measurements have been performed in contrasting vegetation seasons of 2007 and 2008. As a function of time, stomatal conductance and intensity of sap-flow and stem diameter of *Quercus petraea* and *Quercus cerris* trees were measured simultaneously with photosynthetic photon flux density (PPFD), atmospheric pressure, temperature and relative humidity and vapour pressure deficit (VPD) of air, precipitation and soil moisture.

It was found that the two oak species of forest stand exhibit similar daily course of stomatal conductance in rainy periods. However, during drought stomatal conductance of *Quercus cerris* was higher, and after a transitional decrease around midday it exhibited a second maximum in late afternoon. In dry days after a maximum of stomatal conductance at early morning the stomatal closure of *Quer-*

cus petraea was permanent which might result in “carbon starvation” of trees if drought is too long.

During rainy periods, sap-flow of both species changed in correlation with VPD. In dry period this correlation weakened especially in case of *Quercus petraea* but a stronger correlation of sap-flow maximum appeared with the decreasing soil moisture content.

Quercus cerris showed smaller stem radial variation, than *Quercus petraea*, which refers larger water store of stems than in the former species. As a result of drought in 2009 the stem radial growth finished one month earlier than in 2008.

Our results [2] suggest that if the frequency of drought years increases severe physiological disturbances and mortality of *Quercus petraea* can be expected in forest stands of climatically border habitats and *Quercus cerris* can become gradually the dominant tree species.

Acknowledgements

This work was supported by the Hungarian Research Found OTKA (T37961 and K68397).

* Corresp. author: immeszaros@puma.unideb.hu

a) Dept. of Botany, Faculty of Science and Technology, Center of Arts, Humanities and Sciences, Univ. of Debrecen, Egyetem tér 1., H-4032, Hungary.

[1] Mátyás, Cs., Czimer, K., In: Mátyás, Cs., Víg, P. (Eds.), Erdő és klíma IV., Sopron, NyME, 2004, pp. 35-44, ISBN:963 9364 36 3 (in Hungarian).

[2] I. Mészáros *et al.*, In: Víg, P. (Ed.), Erdő és klíma VI., 2009. október 9-10., Nagyatád, NyME, 2010 (in press), (in Hungarian)

6.5 Technology for microbial synthesis of nanoparticles

M. Hunyadi, Z. Gácsi, Z. Szűcs, J. Prokisch^{a)}, A. Csik,

Nanotechnology has a high potential to engineer and alter basic properties of materials, and to exploit unusual phenomena observed on the nanometer scale. Consequently, the development of nanomaterials is already involved in a vast range of application fields, however, most of their characteristics are still underexamined, and relevance of studies on their environmental fate, toxic effects and other health risks have just been recognized. Besides, environmental effects and high costs of present production technologies definitely outline a need of both competitive and eco-friendly alternatives.

It is well known that microbial production of nanoparticles may offer new perspectives in the field of bionanotechnology since it provides clean, inexpensive and “green chemistry” techniques, which are especially desired in the future when technology transfer to large-scale production is concerned. In the last years the development of biosynthetic methods was an exponentially growing field, which focused on nanoparticles of noble metals, elemental and composite semiconductors with diameters in the range of 5-100 nm [1,2].

We initiated the set-up of a new laboratory for studying biosynthesis processes of nanoparticles. The primary goal of this project is to realize the ability of controlling the size of nanoparticles by the conditions of the synthesis, which is motivated by the fact that the optoelectronic and chemical properties are sensitively dependent on this single parameter in addition to their elemental composition. In general, the characterization of nanoparticles, as well as measurements of structural properties require the presence of dedicated analytical infrastructure. The local availability of techniques like TEM, SEM, EDX, XPS, EELS, SIMS/SNMS, AFS, ICP-MS and spectrophotometry provides an advantageous background to consolidate bionanotechnological programs in our institute.

As a result of our first test experiments selenium nanoparticles were successfully synthesized by non-pathogenic *Lactobacillus* strains.

Batch cultures were incubated at 37 °C in MRS nutrient medium supplemented with 0.5 mM Se(IV) solution. Selenite oxyanions functioned as terminal electron acceptors in anaerobic respiration, which lead to the formation of elemental Se(0) nanospheres with a diameter of 150-250 nm as measured in SEM images (Fig. 1). The elemental analysis of the observed nanospheres was also performed, which is shown in Fig. 2.

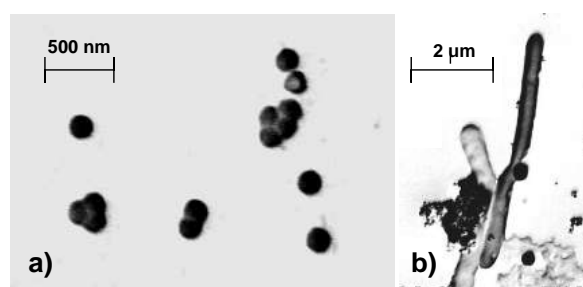


Figure 1. a) SEM image of selenium nanoparticles extracted with sterile filtration from mixed batch cultures of *Lactobacillus* spp.; b) SEM image of selenium nanoparticle bound to cell membrane.

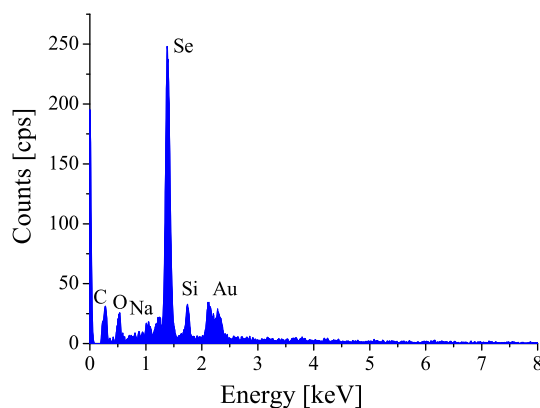


Figure 2. X-ray spectrum taken on the nanospheres observed in the SEM images in Fig. 1.

a) Univ. of Debrecen, Institute of Bio- and Environmental Energetics

[1] H. Bai, Zh. Zhang, Y. Guo, W. Jia, *Nanoscale Res. Lett.* (2009) 4:717-723

[2] N. Tejo Prakash et al., *Biotechnol Lett* (2009) 31:1857-1862

7.1 The ATOMKI Accelerator Center

S. Biri, Z. Kormány, I. Berzi, M. Hunyadi

In 2009 a new division was established in our institute: the ATOMKI Accelerator Center (AAC). Before this time the facilities and staff of AAC belonged to other departments of the institute. The re-organization however, was necessary. It was understood that the translocation of all the accelerators into a centralized unit is advantageous in numerous fields. Here we just mention some of them. The submission of any instrumentation type proposal (EU or domestic) will be easier and has a higher chance to be supported. The organization and distribution of the beamtimes will be more equal and optimal. The usage of the maintenance and spare tools can become better and cheaper. The operating staff (cca. 20 person) can serve at more than one accelerator and the teams can help each other.

The accelerator center actually became a fourth new basic unit of the institute besides

the three traditional scientific divisions (see the Atomki homepage for the organization chart). The following six main facilities belong to the accelerator center:

- Cyclotron
- VdG-5 accelerator
- VdG-1 accelerator
- ECR ion source
- Isotope separator
- Tandetron (under installation)

In figure 1 the placements of these machines are shown in an artistic 3D map of the Atomki. The table 1 summarizes the main parameters of the accelerators. More detailed technical specification of the machines can be found in the new homepage of the center [1].

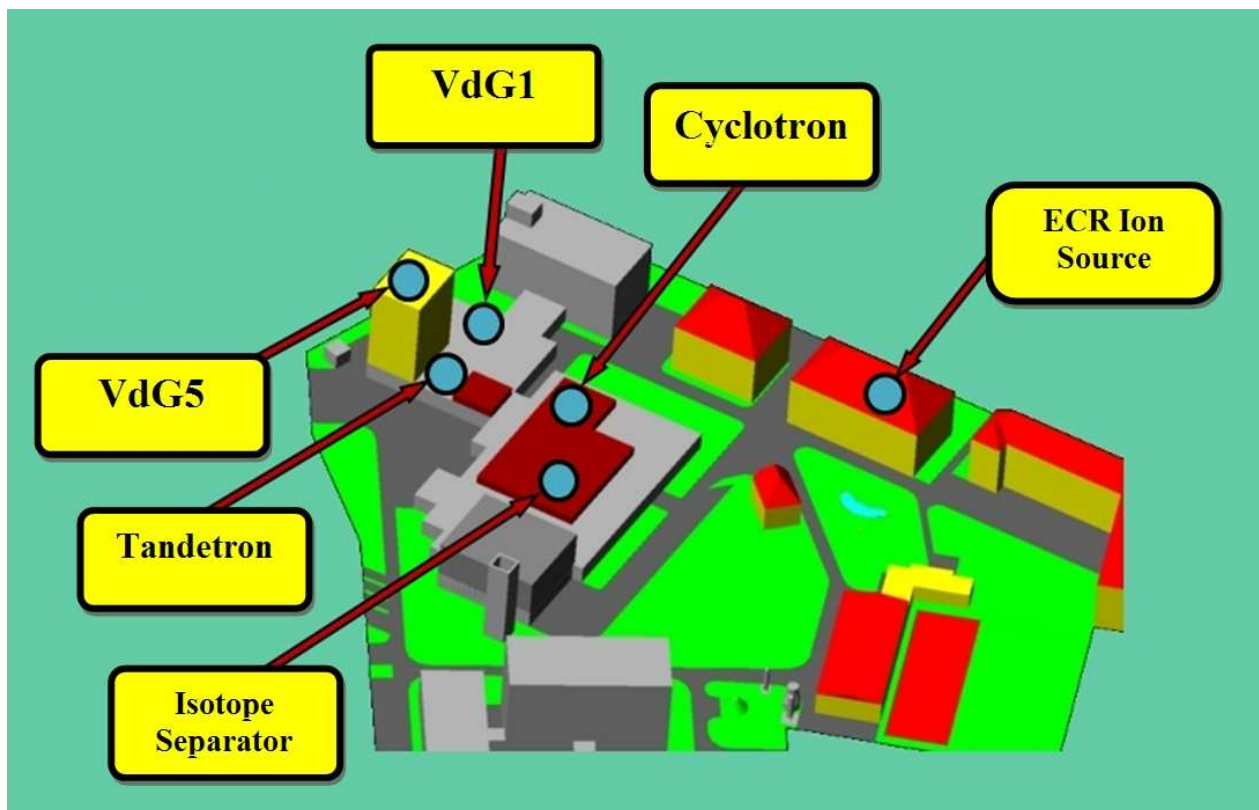


Figure 1. The accelerators of ATOMKI on the layout of the institute.

	Cyclotron	VdG-1	VdG-5	ECR ion source	Isotope separator	Tandetron
Particle	H, D, He	H, He, C	H, D, He, C, N, O, Ne	H...Xe	He, Ne, Ar, N, S, Se	H, D, He, C
Energy range	1-26 MeV	50-1500 keV	0.8-5 MeV	(0.1-30)*Q keV	0.05-50 keV	1-4 MeV

Table 1. The particle and energy range of the ATOMKI accelerators. Most particles in the table are singly or doubly (in the case of He) charged positive ions, except the ECR ion source where multiply charged ions can also be produced (Q: number of removed electrons). The energies are the total achievable kinetic energies.

In 2009 all the accelerators operated as scheduled, safely and without major breakdowns. After the experiences in the first months it can be concluded that the new center works well both for technical and human point of views. In the next sub-chapters the 2009 operation and development details of the individual accelerators are summarized.

Cyclotron operation

The operation of the cyclotron in 2009 was concentrated to the usual 9 months; January, July and August were reserved for maintenance and holidays. The overall working time of the accelerator was 2009 hours; the time used for systematic maintenance was 328 hours. The breakdown periods amounted to only 2 hours last year. So the cyclotron was available for users during 1679 hours and the users required 1242 hours. The effectively used beam-on-target time is summarized in Table 2.

The accelerated particles and the most frequent or typical energies were: proton (44%, 14.5 MeV), deuteron (29%, 10 MeV), alpha (16%, 12.5-15 MeV), He-3 (11%, 24 MeV).

The renewal project of the nuclear magnetic resonance (NMR) based field stabilization system for the energy analyzing magnet has been completed. The original analogue signal processing units were replaced by a newly developed digital system. It first digitizes the low-frequency amplitude modulated signal of the marginal oscillator and then searches for the NMR-resonance. If the resonance is found then the phase of the resonance signal is measured compared to the field modulating sine wave. Based on this measured phase value the

control voltage of the analyzing magnet power supply is adjusted automatically. The system hardware was built applying a C8051F041 mixed signal microcontroller, containing all the peripherals required for the measurement and control of the different components. Signal processing and power supply control is implemented by the microcontroller program and the operator can control the system through a GUI program running on a Windows PC. The new system has been in real operation since March 2009. It provides easy handling, user friendly and reliable operation with measured magnetic field stability values on the $2\text{-}3 \cdot 10^{-5}$, level.

Projects	Hours	%
Nuclear spectroscopy	282	30.7
Nuclear astrophysics	523	42.1
Nuclear data	7	0.6
Medical isotope production	97	7.8
Thin layer activation (TLA)	217	17.5
Target technology	16	1.3
Total	1242	100

Table 2. Statistics of the irradiation time (beam-on-target) for different research groups.

The project of developing new power supplies for the low-current magnet coils of the cyclotron and the beam transport system has been continued. The prototype circuit of the new power supplies was designed, built and tested thoroughly. It contains modern high-voltage tolerant IGBT components in the final stage. They are cooled by forced air, so we can get rid of the water cooling circuits used for the old units. This results in major simplifications in the construction, operation and maintenance of the involved power supplies. After successful trial operation with the prototype four new units were built. Four original units in the first

rack of the beamlines power supply system (belonging to the first two quadrupole doublets) were replaced with the new ones. During the last two months of the operation in 2009 these new units were used and they performed excellently under real working conditions.

VdG-5 and VdG-1 machines

The 5 MV Van de Graaff accelerator (VdG-5) was at service nearly throughout the year. The net beamtime was 1601 hours, mainly proton particles were accelerated (99%). There was little need (1%) for $^4\text{He}^+$ particles. The beam time was distributed among the different research subjects as shown in Table 3.

Field	Sign	Hours	%
Nuclear physics	NP	493	31
Nuclear astrophysics	NAP	113	7
Analitical studies	IBA	632	39
Micromachining	MM	313	20
Machine tests	MT	50	3
Total		1601	100

Table 3. Time distribution among different research activities at VdG-5

The typical energy range of the ion-beam per research subjects were:

Nuclear physics	0.8 MeV–1.3 MeV
Nuclear astrophysics	0.8 MeV–3.6 MeV
Analitical studies	2 MeV
Micromachining	0.8 MeV–2 MeV

We had a three week break-down in October. During that time we repaired the broken parts and performed all the maintenance work that is needed periodically. We replaced some parts of the ion-source, repaired the pre-focus power supply, and carried the maintenance work of the belt driving system out (including replacing some of the special bearings and greasing). This maintenance did not cause any problem to the users. In 2009 the VdG-1 machine was not used however it was avail-

able for users. During the year the preparation of a complicated measurement was carried out in the target room. The measurement itself is scheduled in 2010.

Tandetron installation

The tandetron is a used accelerator given as a gift to our institute years ago. For some technical difficulties it is still under assembling so there has not been operation experience about this accelerator in 2009 yet.

ECR ion source

In November 2008 the ECRIS was stopped to perform a major renewing and refurbishing of the laboratory. This work was finished in February 2009. The goal of the renewing was to establish an up-to-date laboratory at European standard to get an attractive place for foreign and domestic researchers, students and visitors. Some photos showing the new look of the laboratory are in our homepage [1]. Later on, throughout the year we had to stop the continuous operation for some other renewal activities in the ECR building. This restricted a little the overall beamtime and scientific activity of the lab, but all these changes were necessary and finally resulted in a modern and attractive environment for the team and, mainly, for the beam users. Table 4 summarizes the beamtime we supplied in 2009. The “Hours” in the table actually mean the time when a plasma was made in the plasma chamber. In most cases a positive ion beam was extracted from the plasma so the ECRIS operated as a classical low-energy particle accelerator. Sometimes however, we produce just plasma without beam extraction and the investigation target is the plasma itself. The summaries of some research topics in Table 4 are written in individual papers in this annual report (ion guiding, plasma photos). The scientific program “Delta” of the Hungarian “m1” television channel made a short film in the ECRIS laboratory [2].

Research topic	User	Ion species	Extraction voltage (kV)	Hours	%
Ion guiding through capillaries	ATOMKI-DAP	Ne ⁶⁺ , Ar ⁷⁺	0.4-0.5	250	61
Ti-coating with C60	DE-FD, DE-IEP, ATOMKI ECR	C ₆₀ ⁺ , C ₆₀ ⁰	0.2-0.5	40	10
Plasma photo experiments	ATOMKI-ECR	He, CH ₄ , N, O, Ne, Ar, Kr, Xe	–	100	24
Beam development & maintenance	ATOMKI-ECR	Ar ^{1+...16+} Ne ^{4+...9+} , C ₆₀ ⁺	0.1-30	20	5
Total				410	100

Table 4. Plasmas and ion beams delivered by the ECRIS in 2009. The total energy of the beams is the product of the charge and the extraction voltage. DE: University of Debrecen, IEP: Institute of Experimental Physics, FD: Faculty of Dentistry, DAP: Division of Atomic Physics, ECR: ECR Group.

Isotope separator

The isotope separator and low-energy ion beam facility are operational for research involving ion beam applications. The facility offers research potential in fields of both surface physics requiring special deposition techniques, and sub-surface implantation, especially for isotope tracing studies.

The ion source and beam guide system are capable of producing momentum-analyzed, positive singly charged ions in a broad energy range of 50 V-50 kV at a typical beam current of 1-200 μ A. The traditional hot-cathode Freeman-type ion source was redesigned, and a novel vapor injector system was constructed to provide ion beams of solid elements with improved ionization efficiency and stability. The presently utilized range of ions, however, is restricted to non metallic elements with moderate melting point and noble gases. The development of a high-temperature version of the ion source for metallic charge materials is in progress.

The beam guide system is based on a Pierce-type extraction electrode as a one stage accelerator lens, a series of Einzel-lenses and a dual-focusing 55° sector magnet with a nominal momentum-dispersion of 15 mm/%. The central radius of the electromagnet is 1500 mm. The geometry of the exit plane has a tilt angle of 30°, which was designed to achieve a simultaneous vertical and horizontal focusing possibility at a given distance. This feature has not been exploited so far, instead, additional focusing elements were used to place the deposition stages and targeting systems in a limited volume due to vacuum quality considerations taking into account our presently available vacuum technical background.

A scattering/experimenting chamber as a versatile end station of the beam line was designed to host various deposition stages with accel-decel columns. The first assembly of this chamber has been started and partly commissioned in 2009, as well as a prototype version of a thin-film deposition stage was constructed and was mostly employed in soft-landing mode.

[1] <http://www.atomki.hu/Accelerators>

[2] http://videotar.mtv.hu/Videok/2009/03/28/16/Delta_2009_marcus_28_.aspx.

7.2 Fabrication of optical devices in poly(dimethylsiloxane) by proton microbeam

R. Huszánk, S.Z. Szilasi, I. Rajta, A. Csik

Optical diffraction grating and micro Fresnel zone plate type structures were fabricated in relatively thin poly(dimethylsiloxane) (PDMS) layers using proton beam writing technique and the performance of these optical devices was tested.

Micro-optics is a key technology in many fields of common applications like, for example, data communication, lighting technology, industrial automation, display technology, sensing applications and data storage. It enables new functionalities and applications previously inaccessible and improves performance of the already available products with reduced cost, volume and weight. There are a few different fabrication techniques to produce refractive or diffractive micro-optical devices such as X-ray lithography, UV-lithography, e-beam lithography, laser writing, plasma etching, proton beam writing. In general, three different kinds of materials are used for micro-optics, such as glass, polymers and crystal.

PDMS is a commonly used silicon-based organic polymer, optically clear, generally considered to be inert, non-toxic and biocompatible and it has been used as a resist material for direct write techniques only in very few cases.

In this work, PDMS was used as a resist material; the structures were irradiated directly into the polymer. We were looking for a biocompatible, micropatternable polymer in which the chemical structure changes significantly due to proton beam exposure making the polymer capable of proton beam writing.

We demonstrated that the change in the structure of the polymer is so significant that there is no need to perform any development processes. The proton irradiation causes refractive index change in the polymer, so diffraction gratings and other optical devices like Fresnel zone plates can be fabricated in this way. The observed high order diffraction patterns prove the high quality of the created optical devices [1]. This technique may be a useful tool for designing micro-optics for various applications like microfluidics, lab-on-a-chip systems.

Acknowledgements

This work was supported by the EU co-funded Economic Competitiveness Operative Programme (GVOP-3.2.1.-2004-04-0402/3.0)

- [1] R. Huszánk, S.Z. Szilasi, I. Rajta, A. Csik, *Optics Communications* **283** (2010) 176.

7.3 WCGM - a gamma-spectrum analysis program rewritten in Windows

G. Székely

Introduction

The original code [1] was written in Fortran in 1985 and it worked mostly in batch mode. Later the code was redesigned in Pascal and several graphics tools were added. This version (called PGM) is still used, but the limits of MSDOS (memory, graphics, filename length, etc.) make it more and more obsolete. Because of these reasons the redesign of the code is started in order to be able to use it on the most frequently used operating systems, which are nowadays Windows XP and Windows 7.

This paper describes the present state of this work and shows some new ways of the usage of the code. In the same time it invites the reader to visit the home page of the code [2] in order to contribute to the further development.

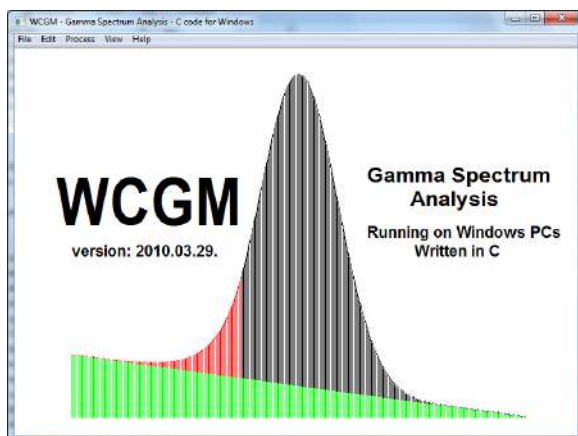


Figure 1. Program logo on the first screen.

Data input

Probably one of the main reasons why the original DOS code is still used is that a lot of input formats are accepted. The following short names identify the currently available input spectrum formats: “ASCII”, “Binary”, “I-format”, “Jyväskylä”, “K-format”, “MCA”, “MCAtxt”, “MSI”, “NBI”, “Ortec”, “Oxford/Nucleus”, “PCA9”, “Tukan”. The most simple ones (ASCII, Binary) contain only the counts of the gamma spectrum, but the more

sophisticated ones (I-format, Tukan) also include data for the energy, resolution and efficiency calibrations. The user can choose different levels of interaction during the input process. One can put everything to a control data file and tell the code to use it, or one can manually find the input spectrum and the calibration data during running the code.

Spectrum processing

After reading the input data the whole spectrum is shown in the main window. To find the peak positions one can use “Process|Automatic peak search” menu item to scan the displayed interval of the spectrum and assign the peaks with black vertical lines, which were selected by the built-in algorithm. Then the user can fine tune this peak set by manually insert or remove peaks, with the help of the right hand side mouse button. By activating “Process|Fit selected spectrum region” menu item, the code starts to fit the peak shape shown on the logo screen (fig.1) at the selected peak positions together with a background function. The parameter settings determining the theoretical functions to be fitted can be edited by the “Edit” menu items. The results of the fit can be saved in a text file and the graphical screen of the code can be also captured and saved.

Graphical manipulations

To determine the spectrum region to be displayed one can move the cursor to the required start position, push the left mouse button and pull the cursor to the required end point. To shift the current region left or right, contract or expand it, or go back to the whole spectrum region - all these functions are solved by a 4-arrow cross with an inner circle - like the one on the map navigation sites. In addition the “View” menu items give a selection for the spectrum displaying modes.

Software environment

The code was developed in C++ and compiled with gcc [3] under DevC++ [4] system. These are free softwares which make it possible to produce executable code in 32-bit Windows systems like XP, Vista or Windows7. The main component that makes the system routines callable for the application code is the Windows API (msvcrt.dll) which is part of the Windows system since the Windows 2000 version.

Content of the code's webpage

The mathematical models of the fitting functions for the calibrations, background and peak shapes can be found in the copy of the original article [1]. A FAQ will be also available as the experiences grow. The most important

is that the executable code and the online help file are there and ready to download. An example spectrum file and the corresponding control data file are also included. The readme.txt file contains the description of the installation of the code and running it with the given example. It also contains the e-mail address of the author, where all the suggestions and opinions are welcome. On the basis of these suggestions the code will be developed further and the new versions will be also available to download.

[1] G. Székely, Computer Physics Comm. **34**, (1985) 313-324.

[2] <http://www.atomki.hu/szekely/wcgm>

[3] <http://gcc.gnu.org>

[4] <http://www.bloodshed.net/devcpp.html>

7.4 Report on the development of an XRF set-up with X-ray tube excitation

I. Uzonyi, Z. Pintye

Ion beam analytical (IBA) laboratories have the potential to analyse materials with various IBA methods in order to determine their bulk composition or lateral and/or depth distribution of elements. However, the establishment of some complementary analytical techniques, especially X-ray Fluorescence (XRF), seems to be essential and has become a common practice in many laboratories.

The aim of this paper is to report about the realization of an XRF setup which is based on nuclear instruments generally available in all IBA laboratories, such as: X-ray detector, signal processor, ADC or MCA, data acquisition software, XYZ-stage, etc. For excitation, a medium power X-ray tube was purchased. Our aim has been to design a flexible system applicable for the analysis of wide spectrum of samples.

The main features of the XRF set-up are as follows:

- Excitation: Oxford Instruments XTF6000BR X-ray tube; target: Rh; Be window: 125 μm ; focal spot size: 80 μm ; cone angle: 20 degrees;

high voltage power supply: 60 kV; 1 mA (60 W).

- Experimental arrangements:
 - Direct excitation
 - Optionally secondary targets
- Detector port to horizontal arrangement Si(Li) X-ray detectors equipped with Oxford Microbeams Ltd.-type interface.
- Construction:
 - Primary radiation collimated to ~ 5 mm
 - Provision for low background measurements
 - Vacuumable system
 - 15-position (manual) sample changer
 - XYZ-stage for tiny samples
- Analytical:
 - Major and trace elements from Na
 - Detection Limit down to ~ 1 $\mu\text{g/g}$
 - Quantification e.g. by AXIL

The setup has been successfully used for the analysis of archaeological bronze metals, soil and sediment samples. Analytical results will be presented elsewhere.

7.5 Micro-XANES and micro-PIXE measurements of iron-rich impact materials from the Barringer Crater

Z. Szikszai, I. Uzonyi, Á.Z. Kiss, G.Á. Sziki*, D. Vantelon^a, P. Rózsa^b

Barringer Crater, also known as Meteor Crater, in Northern Central Arizona was the first recognized impact crater on Earth. It was created about 50,000 years ago by an iron asteroid. A small portion of the incoming asteroid survived in the form of solid fragments, but most of the asteroid material were dispersed.

During our previous investigations, impact material from the Barringer Crater was examined with various nuclear analytical techniques [1]. These powerful tools are dedicated to the study of the elemental composition of the samples and the distribution of elements but do not give access to the chemical state of these elements. However, by combining micro-X-ray Absorption Near Edge Structure (XANES) and micro-Synchrotron X-Ray Fluorescence (SXRF) both the distribution of the elements and their chemical state can be determined [2]. The main aim of the present study was to investigate the valence states of iron [Fe(III), Fe(II), Fe metal] [3] to obtain additional information about the impact processes forming the Barringer Crater.

The samples (tiny magnetic objects) were embedded in artificial resin and polished to get a flat surface. They were covered with a thin carbon layer for pre-selection using electron microprobe. The micro-XANES and micro-XRF measurements were carried out on the LUCIA beamline at SLS with a beam focused to a $4 \times 10 \mu\text{m}^2$ spot. XANES spectra were obtained by recording the Fe K_{α} fluorescence intensity as a function of the incident beam energy over a range of 7.0-7.2 keV. Five samples served as standards with known proportion of chemical states of iron. After determining the position of the pre-edge peaks in the spectra of these minerals, a calibration curve was plotted for estimating the Fe(III)/ \sum Fe ratio in unknown samples.

Chemical speciation screening was also fol-

lowing the method described in [4]. X-ray fluorescence maps were recorded at four different excitation energies, reflecting the differences of the spectra. Iron(0) absorption is significantly higher at the lowest excitation energy (7117 eV) than Fe(II) and Fe(III) absorption. On the other hand, Fe(III) iron exhibits low absorbance at the two medium energies (i.e. 7124 and 7125.8 eV) compared to Fe(0) and Fe(II). At the highest energy (7193 eV) differences in the chemical and physical states do not play a significant role. Systematic calculations of the appropriate yield ratios pixel by pixel showed predominantly iron(II) state, in accordance with the PIXE results. These results were corroborated by XANES measurements in selected spots, as the pre-edge peak position data also suggested a predominantly Fe(II) state in all samples.

This study was presented at the ICNMTA2008 and the corresponding paper was published in NIMB [5].

Acknowledgements

This work was supported by the EU-co-funded Economic Competitiveness Operative Programme GVOP-3.2.1.-2004-04-0402/3.0, the Hungarian-Slovenian intergovernmental S&T cooperation programme (SLO-16/2005) and the Hungarian Research Foundation (OTKA T046579).

* Present address: University of Debrecen

a) Synchrotron SOLEIL, France

b) University of Debrecen

[1] I. Uzonyi, et al., Spectrochim. Acta B **59** (2004) 1717.

[2] M. Mosbah, et al., NIM B **158** (1999) 214.

[3] M. Wilke, et al., Amer. Min. **86** (2001) 714.

[4] D. Grolimund, et al., Spectrochim. Acta B **59** (2004) 1627.

[5] Z. Szikszai, et al., NIM B **267** (2009) 2229.

7.6 Detection efficiency of a low-energy TOF neutron spectrometer

A. Krasznahorkay, A. Algora^{a)}, M. Csatlós, A. Vitéz J. Gulyás, L. Stuhl,

Relativistic heavy-ion beams and especially rare-isotope beams open up a new avenue for studying giant resonances in inverse kinematical reactions. In addition, a large part of physical background can be suppressed by using kinematically complete experiments. The most serious problem of such experiments is the very low energy of the low mass ejectiles, which requires very thin targets for the charged particles.

We are planning to study spin-isospin giant resonances in (p,n)-type reactions at GSI and later on in FAIR in the EXL and R3B collaborations. Using relatively thick targets without disturbing the energy spectrum of the recoiled neutrons has an importance in experiments with rare-isotope beams to achieve reasonable statistics. On the other hand, a resolution of 10 % in the determination of the neutron kinetic energy requires a resolution of 1° in the scattering angle. Therefore a newly designed and developed time of flight scintillator array has been built at ATOMKI Debrecen.

The array consists of 15 scintillator bars with dimensions of $45 \times 10 \times 1000 \text{ mm}^3$, and with fast photomultiplier tubes (XP2262) on both ends. The whole system is mounted on a hollow aluminum frame to reduce the amount of material which can scatter the neutrons.

Detailed Monte-Carlo simulations of the TOF array were performed using the GEANT4 code. The calculations gave about 50 % efficiency for 1 to 4 MeV neutrons if we assumed a detection threshold of 50 keV electron equivalents for the detectors. The scattering probability from one detector to another one was less than 2 %.

The detection efficiency of the system was measured recently using a ^{252}Cf fission source, which neutron spectrum is precisely known. The start signal was generated by the fission fragments detected by a thin (0.2 mm) plastic scintillator. We have got good agreement with the results of Monte-Carlo simulations and also

fair agreement with the efficiency of similar detectors constructed recently in Dresden [1] and in NSCL MSU [2].

The energy resolution of the system was measured with mono-energetic neutrons produced by different (p,n) reactions at the Debrecen cyclotron laboratory. Better than 10 % relative energy resolution was obtained for 1 - 5 MeV energy neutrons.

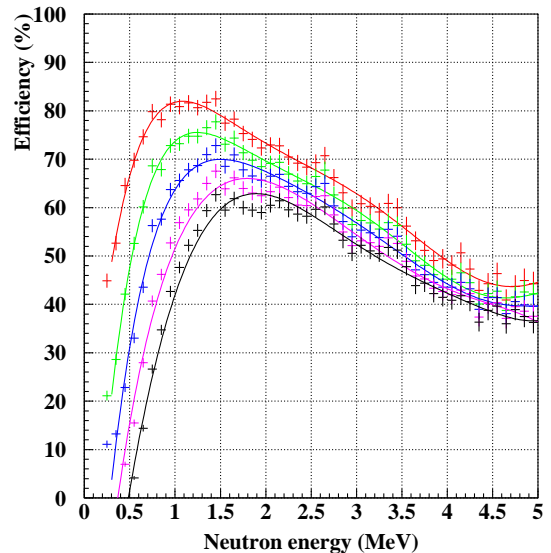


Figure 1. Measured detection efficiency as a function of the neutron energy for different detection thresholds expressed in electron equivalent energy of: 20 keV (red), 40 keV (green), 60 keV (blue), 80 keV (magenta) and 100 keV (black).

Acknowledgements

The work has been supported by the Hungarian OTKA Foundation No. K 72566.

a) IFIC (CSIC-Univ. Valencia), Valencia, Spain

- [1] R. Beyer et al., Nucl. Instr. and Meth. **A575** (2007) 449.
- [2] G. Perdikakis et al., IEEE Trans. on Nucl. Sci. **56** (2009) 1174.

7.7 Deposition station for selenium isotopes

M. Hunyadi, Z. Gácsi, J. Prokisch^{a)}

Isotopic tracing of nanoparticles mostly involved in environmental and metabolic processes, industrial, and agricultural technologies, attracts an increasing attention nowadays. As an experimental goal, for proposed tracing studies selenium was chosen, which is an essential trace element for the nutrition of almost all living organisms, since it plays a crucial role in the antioxidant activity of seleno-enzymes [1]. Selenium in forms of nanoparticles being synthesized by wet chemical or microbial dissimilatory processes, turned out to possess new functionality as exemplified in affecting semiconductor properties, toxicity, and growth factors, which are important for both nutritional supplements and potential cancer therapy agents [2]. Stable isotope tracing of selenium nanoparticles under *in vivo* conditions would then yield relevant information on biodistributions, efficiency and safety issues of applications.

A prototype version of a deposition station for enrichment of stable selenium isotopes was constructed and installed downstream to the sector magnet of the DiSP isotope separator [3]. The deposition of the isotopic beam particles was carried out with the use of self-sputtering technique. The beam with a kinetic energy of 25-30 keV was first guided through electrostatic elements, where it was focused and decelerated to 300-500 eV (Fig. 1). The geometry of the electrostatic lenses was designed with the simulation code SIMION 8. The outgoing beam impinged upon the surface of a tungsten disc, on which recombination and self-sputtering of selenium ions occurred. Sputtering yields and efficiencies were measured as a function of beam intensities. It was concluded that emission of the selenium atoms can be predominantly attributed to heat spike mechanism due to large differences in evaporation characteristics of selenium and tungsten.

The selenium atoms were then deposited as a thin film on a polypropylene (PP) surface with a conical geometry. PP was chosen to resist strong oxidizing agents used for dissolving and processing the selenium. On the

other hand, the deposition as a thin film with large surface-to-volume ratio was also essential to produce oxyanions with a well-controlled oxidation state, strongly affecting the efficiency of nanoparticle biosynthesis.

The isotopic compositions of samples were checked with SNMS (Secondary Neutral Mass Spectrometer) technique at Atomki, while quantitative analyses were carried out with AFS (Atomic Fluorescent Spectrometer) technique at the University of Debrecen. The net efficiency of transforming isotopic Se(0) to Se(IV) was found 0.90 ± 0.25 with respect to estimated values, which were calculated by measuring integrated beam charge, assumed evaporation profiles, and expected losses of the dissolution procedure.

As an outlook, this prototype of deposition station is planned to be developed and integrated in a new scattering chamber, which will host various beam forming, analytical, and target manipulator elements to achieve a higher level of control over parameters of implantation and deposition using isotopic ion beams.

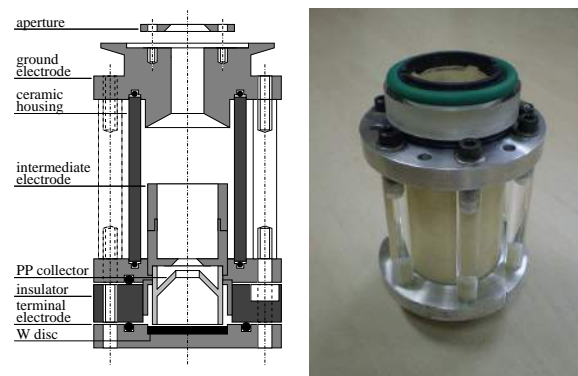


Figure 1. Cross sectional view and photograph of the deposition station.

a) Univ. of Debrecen, Institute of Bio- and Environmental Energetics

[1] B.P. Rosen and Z. Liu, *Environment International* 35 (2009) 512-515

[2] H. Zeng and G.F. Combs Jr, *Journal of Nutritional Biochemistry* 19 (2008) 1-7

[3] M. Hunyadi and Z. Gácsi, *Atomki Annual Report* (2007) 10

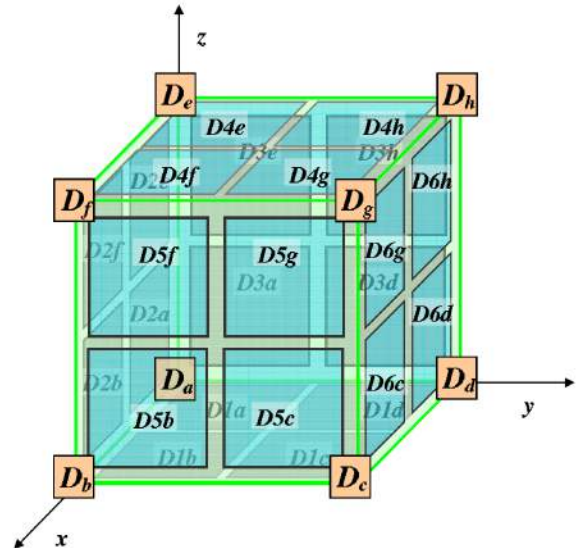
7.8 Theoretical study of three-dimensionally position-sensitive scintillation detector based on continuous crystal

J. Gál, G. Kalinka, B.M. Nyakó

In the field of nuclear imaging (PET, Compton camera, etc.) the application of detectors that are position sensitive in all the three dimensions could increase spatial resolution of images by avoiding the parallax error. In two recent papers [1,2] the viability of a three-dimensionally position-sensitive scintillation detector using continuous scintillator crystal is theoretically studied. For the moment the treatment is limited to cube shaped crystals. The feasibility of building such a detector is based on the recognition that both the spatial position and the radiant flux of a point-like isotropic radiation source can be determined by performing flux density measurements at four appropriately selected points of the space. On this basis one can construct a position-sensitive scintillation detector where the scintillation crystal is surrounded with four or more photodetectors, supposing that the point of interaction (POI) of the gamma ray within the scintillator could be considered as a point-like isotropic light source. The POI coordinates can then be determined relying on the finding that the ratio of two arbitrary linear combinations of the photodetector responses is equal to the same ratio constructed from the solid angles subtended by the photodetectors as seen from the POI. The results of theoretical calculations describing the relations between the photodetector responses and the spatial coordinates of the POI are presented for three different photodetector-scintillator combinations.

The position resolution of such position sensitive scintillation detectors was also investigated theoretically. The standard deviations of the space coordinates were calculated in different cases. For the characterization of the position sensitive detectors different quantities, namely the coordinate quality factors and the volume quality factor were introduced for both the statistical fluctuation and the noise. The calculations show that with four photodetectors the position resolution strongly depends

on the coordinates of the point of interaction. As the POI approaches the crystal surfaces which are not covered with photodetectors the position resolution is gradually degraded. Similar effect is experienced in the case of five photodetector arrangement but to significantly lower extent. However, applying six photodetectors or eight vertex photodetectors around the scintillator the dependence of the position resolution as a function of POI is weak and it shows, as it is expected, a symmetrical behaviour. The figure below shows the arrangement of the eight vertex photodetector, performing the best among the cases analysed, where each of the vertex photodetectors consists of three parallelly connected photodetectors. Assuming 10^4 photons detected with noiseless photodetectors, this arrangement exhibits better than 1 % position resolution in the whole volume of the crystal. In the case of a scintillator with side lengths of 1 cm this means an absolute resolution of smaller than 100 μm .



- [1] J. Gál, G. Kalinka, B.M. Nyakó, Nucl. Instrum. and Methods A 607 (2009) 607
- [2] J. Gál, G. Kalinka, B.M. Nyakó, submitted to Nucl. Instrum. and Methods A

7.9 Giant resonances in BaF₂ scintillators

T. Papp, J. Gál, G. Kalinka, J. Molnár, J. Tóth, D. Varga*

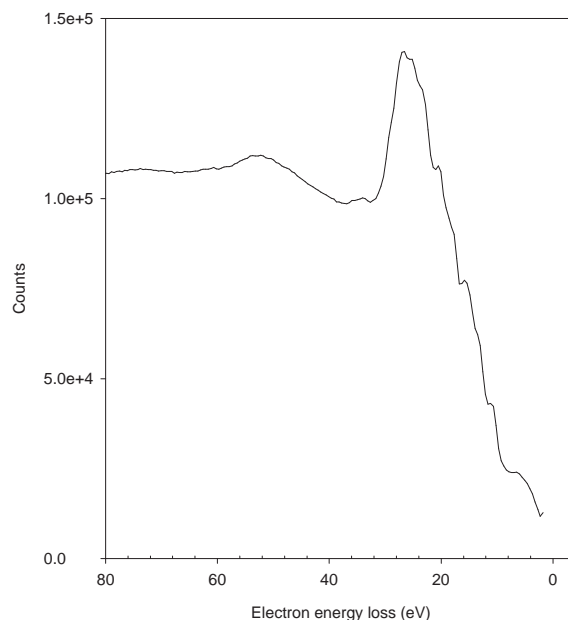
BaF₂ as a scintillation material is interesting because it belongs to the group of scintillators having core-valence (C-V) luminescence. In addition this core valence luminescence is Auger free luminescence [1]. Therefore the excited core state decays with a single photon transition. The Auger decay channel is energetically forbidden. As a consequence, the scintillator has well defined photon energy and is fast, having the decay time constant of 0.6 ns. There are additional photons filling the bubbled up vacancy, and in the literature they are attributed to the self trapped excitons. The decay mechanism has been extensively studied and a rich variety of decay mechanisms have been suggested in the last decade [2]. Many of these suggested mechanisms are questionable, as they do not have the correct energy values [3].

In these studies generally photons are used to excite the crystals and the fluorescent and luminescent lights are observed. However, in gamma ray detection the gamma rays produce energetic electrons, via photo- and Compton effects, and these energetic electrons are producing the interactions that will yield light emission.

To study the mechanism, we have chosen energetic electrons from an electron gun and have collected the reflected electron energy loss spectra (REELS) with the ESA31 spectrometer of ATOMKI. We have observed that there is a dominating energy loss process, which is the excitation of the Ba 5p electrons to the giant resonance of Ba. A typical spectrum measured at 4 keV electron energy is presented in the figure.

Between 20 and 30 eV is the energy loss peak due to exciting the 5p electrons to the giant resonance. The broad peak between 40 eV and 60 eV corresponds to two consecutive ex-

citations. This is the first proposal to incorporate giant resonances in the interaction mechanism in BaF₂ scintillators. From this mechanism the expected photon numbers per MeV of energy deposition can be derived, and such derivation predicted remarkably well the photon numbers for some other scintillators. However, for BaF₂, the experimentally observed photon number need to be corrected for photon loss before such a comparison could be made. The giant resonance model needs to be added to the concept of self trapped exciton model.



* T.P. acknowledges support from the Marie Curie International Reintegration Grant within the 7th European Community Framework Programme.

- [1] M. Kamada, S. Fujiwara, O. Arimoto, Y. Fujii, S. Tanaka, *J. Electron Spectrosc. Rel.Phenom.* 88-91 (1998) 297
- [2] P.A. Rodnyi, *Radiation Measurements* 38 (2004) 343
- [3] P.A. Rodnyi: *Physical processes in inorganic scintillators*, CRC Press, Boca Raton, 1997

7.10 The energy linearity and resolution of Si based X-ray detectors based on the properties of plasmons

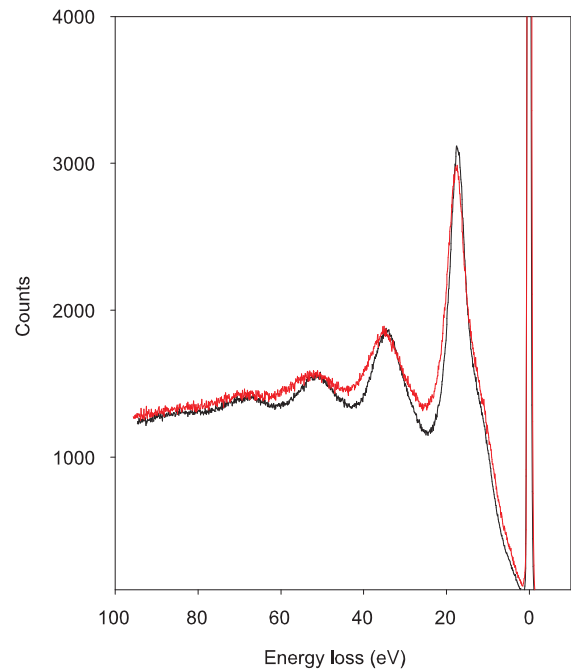
T. Papp, G. Kalinka, J. Tóth, D. Varga*

The modeling of energy-dispersive X-ray spectra has no firm basis yet, which imposes several limits for the derivation of data, and opens a significant room for individual interpretation. Two required basic necessities are the functional form of the energy dependence of the spectrum and the peak line shape. Since statistical processes are involved in the creation of a signal, the event distribution can be characterized by the moments of the statistical distribution, and the first few moments have special names. The first moment is the mean. In our case it will correspond to the X-ray energy. The second (central) moment is the variance. In the case of an X-ray spectrum it is frequently assumed that the peak has a Gaussian line shape; the FWHM of a Gaussian peak is related to the variance as $\text{FWHM}=2.35(\text{variance})^{1/2}$. It is customary to assume that electron hole pairs are created with a given ionisation energy, and use Poisson distribution to derive the so-called Fano factor.

In our study of the energy transfer processes we have concluded that the process is different than the above assumption. If x-rays are detected, then the x-rays will create energetic electrons in the detector and these electrons will move in the crystal, losing energy first and foremost via creating plasmons in their path. How the plasmon decays is still in debate in the literature. Our conclusion is that a plasmon decays primarily by creating a well-defined vacancy in the valence band, an electron and, as silicon is an indirect band gap semiconductor, a phonon. Therefore, the energy transfer path has three steps, each with their own statistical distribution: (i) a dominating plasmon creation channel, (ii) creation of a well-defined vacancy via the plasmon decay and (iii) decaying of the vacancy via electromagnetic radiation and Auger processes. Based on this model, the moments of the statistical distribution were derived.

We have measured the plasmon energy and

line shape with reflected electron energy loss spectroscopy and have observed that the plasmon energy and breadth are changing at lower energies. The figure shows such REELS spectra of Si measured with incident electron energies of 2.2 (black) and 1.2 keV (red/wider plasmon losses). At higher energies the plasmon shape and energy are essentially the same as that presented by 2.2 keV energy events.



It can be concluded from this observation that starting at around 3 keV and extending downwards, the energy dependence of the x-ray peaks is not a linear function, and even has a non-monotonic behavior for Si based detectors. The deviation from the linearity becomes emphasized below 1 keV. Similar conclusions were obtained for the second moment. This observation helps to create a proper response function model in the low energy region.

* T.P. acknowledges support from the Marie Curie International Reintegration Grant within the 7th European Community Framework Programme.

8.1 Events

Nuclear Data Newsletter Issue No. 47, May 2009, Meeting Reports

- pp. 7-8. IAEA Consultants Meeting on Total Absorption Gamma-ray Spectroscopy (TAGS) -
Current Status of Measurement Programmes for Decay Heat Calculations and Other Applications,
Alejandro Algora,
27-28 January 2009
- pp. 8-9. Reference Data Libraries for Nuclear Applications - ENSDF,
János Timár, Zoltan Elekes,
10-11 November 2008
- p. 11. Technical Meeting of the International Network of Nuclear Reaction Data Centres, IPPE, Obninsk,
and Moscow State University, Moscow, Russian Federation,
Ferenc Tárkányi,
22-25 September 2008

30th Physicist Days

2-7 March 2009

Scientific meeting to celebrate the 80th birthday of Tibor Fényes

(in Hungarian, speakers D. Berényi, A. Algora, Zs. Podolyák, D. Sohler)
19 May 2009

Specs, the manufacturer of the SNMS jointly operated by ATOMKI and the University of Debrecen uses our Facility as a reference on their website: http://www.specs.de/cms/front_content.php?idcat=131
20 May 2009

Scientific meeting to celebrate the 70th birthday of Árpád Z. Kiss

(in Hungarian, speakers E. Koltay, Zs. Fülöp, I. Rajta, G.Á. Szíki)
21 May 2009

Szalay-centenary

24 September 2009

Researchers' Night

25 September 2009

Ádám Kovách has been elected to be a member of The Executive Board of Science on Stage Europe
10 December 2009

8.2 Hebdomadal Seminars

5 February

How to swim in sand?

T. SHIMADA (Department of Applied Physics, University of Tokyo)

19 February

High resolution measurements using Grand Raiden spectrometer at RCNP

H. FUJITA (Research Center for Nuclear Physics (RCNP), Osaka University, Japan)

12 March

Adiabatic and diabatic dynamics of fusion in heavy ion collisions

W. SCHEID (Justus-Liebig Universitat, Giessen)

19 March

EURISOL: scientific motivations and European Roadmap

Y. BLUMENFELD (CERN), M. LINDROOS (CERN)

26 March

State of affairs

Zs. FÜLÖP, M. PÁLINKÁS, B. SULIK, R. LOVAS, Z. TRÓCSÁNYI

2 April

ILC: the next big accelerator?

D. HORVÁTH (Research Institute for Particle and Nuclear Physics (RMKI), Budapest)

9 April

Experimental investigation of exotic nuclei

L. CSIGE

23 April

Ion beam analysis of materials in one and two dimensions

R.W. SMITH (ATOMKI, Cyclotron Section, WEMESURF project)

30 April

Development of secondary education of science - plans, results, tasks

P. ÁDÁM (Research Institute for Solid State Physics and Optics (SZFKI), Budapest)

7 May

This is not a report, it is entertainment! Or, how does the media present science to the general public?

G. HRASKÓ (Scientific journalist)

14 May

Nanoscopium: Scanning hard X-ray beamline at Soleil synchrotron

A. SOMOGYI (Soleil synchrotron)

28 May

Treasures of an ice covered world: story of my Antarctic expedition

Z. PÉCSKAY

3 June

Physicist fathers and sons

Gy. RADNAI (Eötvös Loránd University, Budapest)

11 June

Physicist point of view of the Cellular automata theory

I. HORVÁTH (mathematician)

18 June

The origin of mass

T. FÉNYES

25 June

Neutron scattering measurement techniques at high flux neutron sources (ESS)

P. HARMAT (ANTE Innovative Technologies Ltd., Székesfehérvár)

16 July

General overview of NECSA and New method to make isotopic ^{35}S

M. PHETOE and J. TOPKIN (Nuclear Energy Corporation of South Africa, Pelindaba, Pretoria)

- 2 September
Investigation of the modern carbon dynamics at Baradla-cave by isotopic and gas measurement methods
Regional atmospheric fossil fuel CO₂ study in a Central European city
M. MOLNÁR
- 10 September
Dynamics of ion guiding through nanocapillaries in insulating polymers
N. STOLTERFOHT (Helmholz Zentrum, Berlin)
- 17 September
Proton radius story
I. ANGELI (Department of Experimental Physics, University of Debrecen)
- 1 October
Young scientists reports
Á. BIHARI, Zs. JÁNOSFALVI
Introduction of new colleagues in Atomki
A. ANGYAL, L. CSEDREKI, E. FURU, G. GÁL, F. NAGY
- 8 October
Discussions about relativistic temperature
T. BIRÓ (Research Institute for Particle and Nuclear Physics (RMKI), Budapest)
- 15 October
Hirsch-mechanism, z-index and others
L. ZOLNAI
- 22 October
Introduction of new colleagues in Atomki
Z. HALÁSZ, A. PAPP, T. SZÜCS, T. TORNYI
- 12 November
Present and future of medical radionuclide production at cyclotrons
S.M. QAIM (Forschungszentrum Juelich GmbH, Germany)
- 26 November
Quantum dissipative systems via bosonisation of fermion gas-impurity models
P. JARVIS (School of Mathematics and Physics, University of Tasmania)
- 1 December
Asymptotic iteration method and its applications in quantum mechanics
O. ÖZER (University of Gaziantep, Turkey)
- 3 December
The astrophysical p-process - simulations and the necessity of an experimental database
I. DILLMANN (Technische Universität München)
- 8 December
Photon-induced reactions and K-isomers in nucleosynthesis: ¹⁸⁰Ta, ¹⁷⁶Lu, ¹⁸⁶Re
P. MOHR (Schwäbisch Hall)
- 10 December
Cluster features of deformed nuclear shapes
G. ADAMIAN (Bogoliubov Laboratory of Theoretical Physics, JINR, Dubna)

8.3 Awards

Dénes Berényi
Jurányi Award

István Csige
Radiation Protection Nivo Award, Somos Foundation

Zsolt Fülöp, György Gyürky, Dezső Horváth, Attila Krasznahorkay
Nivo Award for Publication (Ed.: A. Vértes: "Szemelvények a nukleáris tudomány történetéből" in Hungarian)

Dezső Horváth
HAS Academy Award

József Imrek, Gábor Kiss
ATOMKI Young Scientist Award

Árpád Kiss
Officer's Cross Order of Merit of the Republic of Hungary

László Kövér
Roland Eötvös Physical Society: Zoltán Gyulai Award

Mihály Molnár
Fermi Young Researcher Award
HAS Young Scientist Award

Mihály Novák
MTA Fiatal Kutatói Oklevél

László Palcsu
György Hevesy Award

Éva Svingor
ATOMKI Szalay Award

József Tóth
Best Poster Award at OATK (National Materials Science Conference)

8.4 List of Publications

The total number of publications in 2009 was 294, of which 172 SCI papers, 90 other papers and proceedings, 3 theses, 6 diploma works, 19 books or book chapters and 4 edited works.

The list of the Institute's publications can be found on-line at:
<http://www.atomki.hu/p2/years/yea02009.htm>

Author index

- Achouri N.L., 29
Adachi T., 30
Aiba T., 25, 26
Algora A., 30, 32, 84
Ander I., 73
Angélique J.C., 29
Angyal A., 68, 69
Aoi N., 25, 26
Arbó D.G., 42, 47
Arcidiacono C., 38
Arias J.M., 36
Astier A., 33
Aumayr F., 58
Avriganu M., 31
Azaiez F., 29
- Baba H., 25, 26
Baiborodin D., 29
Bastin B., 29
Bazzacco D., 33
Bednarczyk P., 32, 33
Bemmerer D., 25, 26
Benjamin E.A., 27
Berezky R.J., 57, 58
Berényi D., 1
Berzi I., 75
Bihari Á., 64–66
Biri S., 1, 48, 75
Borbély S., 42, 43, 46, 47
Borbély-Kiss I., 68
Borcea R., 29
Boston A.J., 33, 34
Bourgeois C., 29
Brown B.A., 25
Bučar K., 44
Buforn N., 33
Burgdörfer J., 40, 41, 43, 50
Burger A., 29
Buta A., 29
- Chamon L.C., 27
Chantler H.C., 33, 34
Chapman R., 29
Chiara C.J., 33, 34
- Csatlós M., 30, 84
Cseh J., 27, 37
Cserny I., 49
Csik A., 56, 74, 79
Curien D., 32
- D'onofrio A., 24
Dalouzy J.C., 29
Darai J., 27
Das S., 57
Dassanayake B.S., 57
De Cesare M., 24
De Cesare N., 24
Deaven J., 30
Di Leva A., 24
Dimitriou K., 42
Ding Z.J., 52
Dlouhy Z., 29
Dobos E., 68
Dombóvári P., 67
Dombrádi Zs., 25, 26, 29, 32, 33
Drouard A., 29
Drube W., 49
Duchene G., 32
- Egri S., 49
Elekes Z., 25, 26, 29, 31, 35
Estevez E., 30
- Farkas J., 35
Feist J., 43
Fenyvesi A., 73
Filho R.L., 27
Fossan D.B., 32–34
Fox C., 33
Franchoo S., 29
Fujita H., 30
Fujita Y., 30
Fülöp Zs., 24, 25, 26, 31, 35
Furumoto T., 25, 26
Futó I., 60, 61

Gácsi Z., 54, 59, 74, 85
Gál J., 32, 86, 87
Galaviz. D., 31
Gianlanella L., 24
Gizon A., 32, 33
Gizon J., 32, 33
Gravielle M.S., 42
Grévy S., 29
Guess C., 30
Gulyás J., 30, 84
Gulyás L., 1, 41
Gustova M. V., 71
Gyürky Gy., 24, 31, 35

Harangi Sz., 60
Haszpra L., 61
Hatanaka K., 30
Hecht A.A., 33, 34
Hegmann N., 55
Hirota K., 30
Hooi Jim O., 30
Hunyadi M., 59, 74, 75, 85
Huszánk R., 79

Iacob S., 29
Imbriani G., 24
Ishikawa D., 30
Iwasa N., 25, 26

Jánosfalvi Zs., 49
Janovics R., 66
Jansen D., 71
Jenkins D.G., 32
Joshi P., 32
Juhász Z., 1
Jull A.J.T., 60

Kalinka G., 86–88
Kanalas P., 73
Kavčič M., 44
Kertész Zs., 68, 69
Kintz N., 33
Kiss Á., 25, 26
Kiss Á.Z., 83
Kiss G.G., 31, 35

Kobayashi T., 25, 26
Koike T., 32–34
Köllő Z., 62, 67
Kondo Y., 25, 26
Kormány Z., 75
Kovács B., 64
Kovács Z., 70
Kövér Á., 1, 38, 39
Kövér L., 49
Kowarik G., 58
Krasznahorkay A., 30, 32, 84
Kretschmer A., 31
Kumar N., 70
Kunz R., 24
Kuti I., 32–34

Laricchia G., 38, 39
Laurent B., 29
Lazar M., 29
Lemell C., 40, 50
Lévai G., 22, 23, 36
Liang X., 29
Lienard E., 29
Lukyanov S.M., 29
Lunardi S., 33

Macé A., 58
Mádai V., 54
Major I., 61
Major Z., 62, 66, 67
Manga L., 67
Mangano G., 24
Maslov O. D., 71
Matsubara H., 30
Meharchand R., 30
Mészáros I., 73
Miraglia J.E., 42
Mogyorósi M., 64–66
Mohr. P., 31
Molina F., 30
Molnár Gy., 56
Molnár J., 32, 87
Molnár M., 60, 61, 66, 67
Motobayashi T., 25, 26
Mrazek J., 29
Murtagh D.J., 38, 39
Murzin D.Yu., 70

Nagele S., 43
 Nagy L., 43, 46, 47
 Nakabayashi T., 25, 26
 Nalpas L., 29
 Nannichi T., 25, 26
 Negoita F., 29
 Nolan P.J., 33
 Nowacki F., 29
 Nyakó B.M., 33, 86

Okamura H., 30
 Oláh V., 73
 Orbán A., 1
 Ordine A., 24
 Orr N.A., 29
 Otani Y., 27
 Özer O., 22, 23

Palásthy B., 44
 Pálincás J., 1, 48
 Palcsu L., 62, 66, 67
 Papp L., 62, 66, 67
 Papp T., 1, 59, 87, 88
 Paripás B., 44
 Paul E.S., 32–34
 Pázmán J., 54
 Penionskhevitch Y., 29
 Perdikakis G., 30
 Péter L., 56
 Petrache C.M., 33
 Pintye Z., 82
 Podolyak Zs., 29
 Pougheon F., 29
 Prokisch J., 74, 85

Rác R., 1, 48
 Raddon P.M., 32
 Rainovski G., 32
 Rajta I., 79
 Ranga T., 67
 Rastrepina G., 35
 Ricsóka T., 1
 Ricz S., 1
 Rinyu L., 60, 61
 Roca V., 24
 Rogalla D., 24

Rolfs C., 24
 Romano M., 24
 Roussel-Chomaz P., 29
 Rózsa P., 83
 Rubio B., 30

Sakuragi Y., 25, 26
 Sakurai H., 25, 26
 Salma K., 52
 Sampson J.A., 33
 Sarkadi L., 1
 Sarkadi-Pribóczki É., 70
 Scheurer J.N., 32
 Schiessl K., 40
 Scholl C., 30
 Schürmann D., 24
 Sciani W., 27
 Scraggs H.C., 33
 Shvetsov V. N., 71
 Simons A.J., 32
 Sohler D., 25, 26, 29, 32–34
 Solleder B., 40, 50
 Somorjai E., 24, 31, 35
 Sonnabend K., 31
 Sorlin O., 29
 St-Laurent M.G., 29
 Stanoiu M., 29
 Starodub G. Ya., 71
 Starosta K., 32–34
 Stefan I., 29
 Strieder F., 24
 Stuhl L., 30, 84
 Sulik B., 1, 45
 Sűsoy G., 30
 Suzuki T., 30
 Svingor É., 61
 Székely G., 80
 Szíki G.Á., 83
 Szöllősi E., 73
 Szücs T., 35
 Szűcs Z., 64, 65, 71, 72, 74
 Szikszai Z., 69, 83
 Szilasi S.Z., 79
 Szily A., 27
 Szirmai G., 55
 Szoboszlai Z., 68, 69

Takács S., 71, 72
 Takashina M., 25, 26
 Takeuchi S., 25, 26
 Tamii A., 30
 Tanaka K., 25, 26
 Tanis J.A., 57
 Terrasi F., 24
 Thies J., 30
 Thiess S., 49
 Timár J., 32–34
 Tókési K., 1, 40–47, 50–53, 57, 58
 Togano Y., 25, 26
 Topkin J., 72
 Török I., 1
 Török T.I., 55
 Tóth I., 65
 Tóth J., 52, 54, 55, 59, 87, 88
 Tóth-Kádár E., 56
 Tsoncheva T., 70

Uzonyi I., 82, 83

Vad K., 56
 Vajta Zs., 26
 Vaman C., 32
 Vantelon D., 83

Varga D., 1, 51, 52, 59, 87, 88
 Veres M., 66
 Vitéz A., 84
 Vostokin G. K., 71

Wadsworth R., 32–34
 Walker A., 33
 Wang J., 41
 Wilkinson A.R., 32
 Williams A.I., 38, 39

Yamada K., 25, 26
 Yamaguchi M., 25, 26
 Yoneda K., 25, 26
 Yubero Y., 53

Zeevaart J.A., 71, 72
 Zegers R., 30
 Zenihiro J., 30
 Zhang P., 52
 Zhang Z.M., 52
 Zilges A., 31
 Žitnik M., 44
 Zolnai L., 32, 33